Dissertation zur Erlangung des Doktorgrades

der Fakultät für Chemie und Pharmazie

der Ludwig-Maximilians-Universität München

Preclinical characterization of the myxobacterial compound

pretubulysin as novel vascular disrupting agent

Verena Karoline Kretzschmann

aus Stuttgart

2013

Erklärung

Diese Dissertation wurde im Sinne von § 7 der Promotionsordnung vom 28. November 2011 von Frau Prof. Dr. Angelika M. Vollmar betreut.

Eidesstattliche Versicherung

Diese Dissertation wurde eigenständig und ohne unerlaubte Hilfe erarbeitet.

München, den 07. November 2013

Verena Karoline Kretzschmann

Dissertation eingereicht am: 07.11.2013

1. Gutachter: Prof. Dr. Angelika M. Vollmar

2. Gutachter: Prof. Dr. Robert Fürst

Mündliche Prüfung am: 12.12.2013

to my family

CONTENTS

1 INTRODUCTION

1.1 Background and aim of the study

Since the 1960s, microtubule targeting agents (MTA) have become the most successful and effective chemotherapeutic agents used in the clinic today. They are effective well below their maximum tolerated dose (MTD) and are used as single agents or in combination for the treatment of a variety of hematological malignancies and solid tumors.[1] Their success is based on the fact that they target microtubules, which are essential components of the cytoskeleton and play important roles in regulating mitosis, cell shape, trafficking, signaling and motility.[2] Depending on their way of action, MTAs can be divided into two classes: microtubule stabilizers and destabilizers.[3] In the last years it became increasingly evident that the antitumor effects of MTAs not only rely on their ability to interfere with the mitotic spindle apparatus and to provoke tumor cell death, but also show promising anti-metastatic, anti-angiogenic and vascular disrupting effects.[4]

The latter is mediated by a relatively new group, called vascular disrupting agents (VDAs). These agents target, in contrast to the classic angiogenic inhibitors (AI), the already established tumor vasculature of larger solid tumors and selectively induce tumor vessel collapse, stop of blood flow and central necrosis.[5] In recent years, natural compounds of the destabilizing MTA class were the most successful VDAs. Among them, combretastatin A-4-phosphate (CA-4-P), the most famous and intensively investigated VDA, which was originally isolated from the African tree *Combretum caffrum*,[6] is currently in clinical trial phase III.[7] Despite their promising anti-tumor properties, the efficiency of VDAs is limited due to certain side-effects and drug resistance.[8, 9] To circumvent these obstacles it is important to expand the pool of VDAs by identifying new compounds. Hereby natural sources like plants, bacteria or fungi, which produce a high diversity of compounds suitable as lead structures, represent a very promising option, however, poor accessibility is still a major challenge.

In 2009, pretubulysin (PT), a natural compound of myxobacterial origin (*Angiococcus disciformis*), was first synthesized in gram scale by Ullrich *et al.*[10, 11] It represents a biosynthetic precursor of the microtubule depolymerizing tubulysins,[12] which recently showed high activity against different tumor cell lines.[13, 14] PT is like tubulysin, a linear tetrapeptide, but its structure is less complex, making them synthetically more easily accessible. Since PT is able to depolymerize microtubules nearly in the same potency as tubulysin and shows profound anti-tumor as well as anti-angiogenic properties,[15, 16] we hypothesized that PT could act as a new VDA.

The **aims of the study** were:

 I. to clarify if PT is able to induce typical features of vascular disruption *in vitro* and *in vivo* and

 II. to elucidate the underlying signaling pathway induced by PT in endothelial cells.

1.2 Natural compounds

1.2.1 Importance of natural compounds

Natural products produced by plants and microbes have played an essential role in drug discovery.[17] Due to their high chemical diversity and their biological history, they offer an enormous source of potential new therapeutic agents, either as lead structure or directly. Today many natural products are tested in clinical trials against several malignancies.[18] In recent years, myxobacteria have gained importance since they are great producers of a variety of secondary metabolites with different biological activities and modes of action.[19] The most promising anti-cancer agents isolated from myxobacteria are the microtubule-binders epothilones and tubulysins.[13, 18]

1.2.2 Myxobacteria as producers of natural compounds

Myxobacteria belong to the group of gram-negative δ-proteobacteria, which occupy a wide range of habitats including soil, decomposing plant materials and the bark of trees.[20] They are characterized by special behaviors that differentiate them from other bacteria: i) They move by gliding or creeping over the surface and produce several extracellular enzymes for food digestion. ii) They typically build swarms of many cells, kept together by intercellular signal molecules and in case of scarce resources (*e.g.* starvation conditions) they aggregate into fruiting bodies[21] (Figure 1 A-C). iii) Their genomes are very large, thus producing an enormous variety of secondary metabolites (*e.g. Sorangium cellulosum* with 20 and *Myxococcus xanthus* with 18 gene clusters).[22, 23] Reichenbach and Höfle[24] were the first describing this variety and opened up the field for new natural compounds with new chemical structures and modes of action.[19]
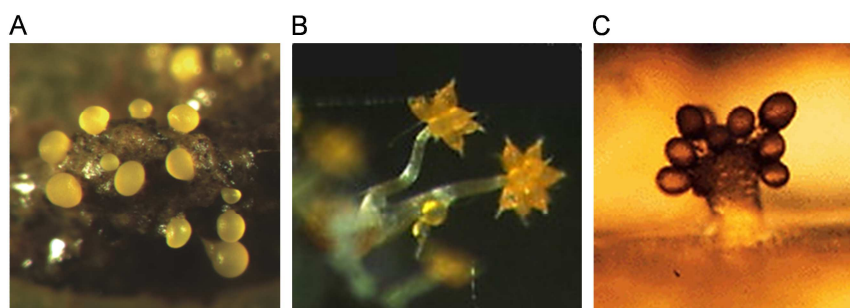
Figure 1   **Typical fruiting bodies of myxobacteria. A:** *Myxococcus xanthus* (www.wikipedia.de) **B:** *Chondromyces apiculatus* (www.sciencedirect.com) **C:** *Stigmatella aurantiaca* (www.sciencedirect.com).

1.2.3 The myxobacterial compound pretubulysin

In the present work, the myxobacterial compound pretubulysin (PT) was intensively investigated concerning its vascular disrupting activity. PT was first isolated from *Angiococcus disciformis* An d48 in very small amounts.[12] It is a biosynthetic precursor of the microtubule depolymerizing tubulysins,[12] which have recently been described to be highly active against different tumor cell lines.[13, 14] Structurally, PT is a linear tetrapeptide consisting of N-methylpipecolic acid (Mep), isoleucine (Ile), tubuvaline (Tuv) and either tubuphenylalanine (Tup) or tubutyrosine (Tut) (Figure 2). In contrast to tubulysins, PT lacks the acetoxy group and the *N,O*-acetal functionality,[12] which makes PT synthetically more easily accessible compared to tubulysin.[25-28] In 2009, PT was first synthesized in the gram scale by Ullrich *et al.*[10, 11] and although the structure of PT is less complex, it shows nearly the same microtubule depolymerizing potency as tubulysin and is also able to inhibit tumor cell growth.[15]

Tubulysin	R^1	R^2
A	$CH_2CH(CH_3)_2$	OH
B	$CH_2CH_2CH_3$	OH
C	CH_2CH_3	OH
D	$CH_2CH(CH_3)_2$	H
E	$CH_2CH_2CH_3$	H
F	CH_2CH_3	H
G	$CH=C(CH_3)_2$	OH
H	CH_3	H
I	CH_3	OH
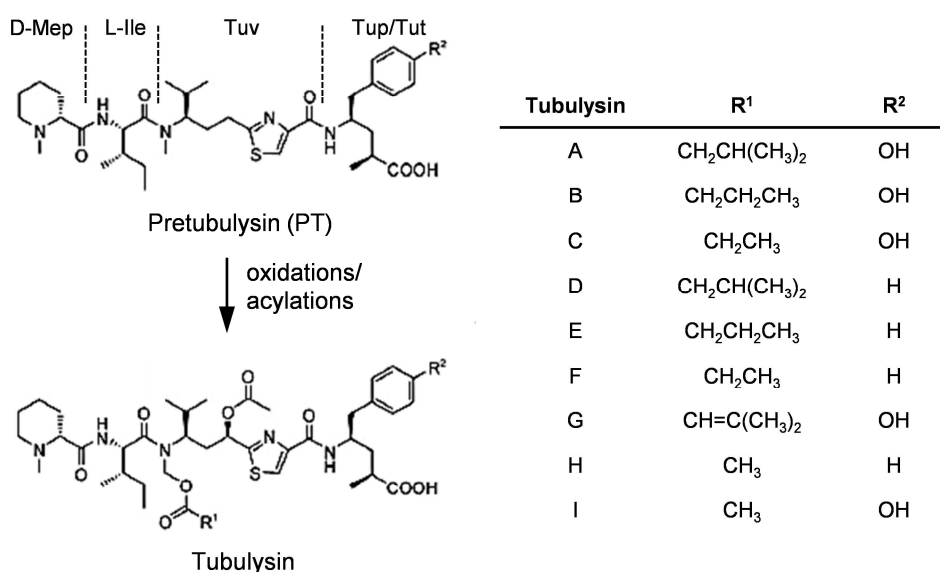
Figure 2   Pretubulysin and the proposed biosynthetic pathway to the nine known tubulysins. Adapted according to Ullrich *et al.*[11]

1.3 The microtubule system

The eukaryotic cytoskeleton is composed of three distinct elements: actin microfilaments, intermediate filaments and microtubules. The latter represent a dynamic system, which is critically important for the spatial and temporal organization of eukaryotic cells. Microtubules are involved in many cellular functions such as intracellular transport, organelle positioning, cell migration and polarization, signaling and cell division.

1.3.1 Structure of microtubules

Microtubules are hollow tube-like structures of about 24 nm in diameter comprised of heterodimers of α- and β-tubulin (each 55 kDa). Both tubulin subunits alternately (head to tail) build longitudinal and lateral contacts to form the main element of microtubules, the protofilament (Figure 3). *In vivo* 13 parallel offset protofilaments build the helical microtubule, whereby the remarkable organization of tubulin heterodimers results in a polarized microtubule, consisting of a (+)-end (β-tubulin) and a (-)-end (α-tubulin). The polymerization of α- and β-monomers depends on guanosine triphosphate (GTP), which binds to its GTP-binding site at the N-terminal domain of α- and β-subunits. The α-tubulin subunit only binds GTP at the dimer interface and it is never hydrolyzed or exchanged, whereas β-tubulin binds both, GDP and GTP.[29] Microtubules are anchored via their (-)-ends at the MTOC, which is located at the perinuclear region and is also known as centrosome. It consists of two centrioles and proteins which are important for microtubule anchoring and organization. One of them, the γ-tubulin, associates with other proteins to form the γ-TuRC (Tubulin Ring Complex), thus promoting αβ-heterodimer binding and microtubule nucleation (Figure 3).[30]
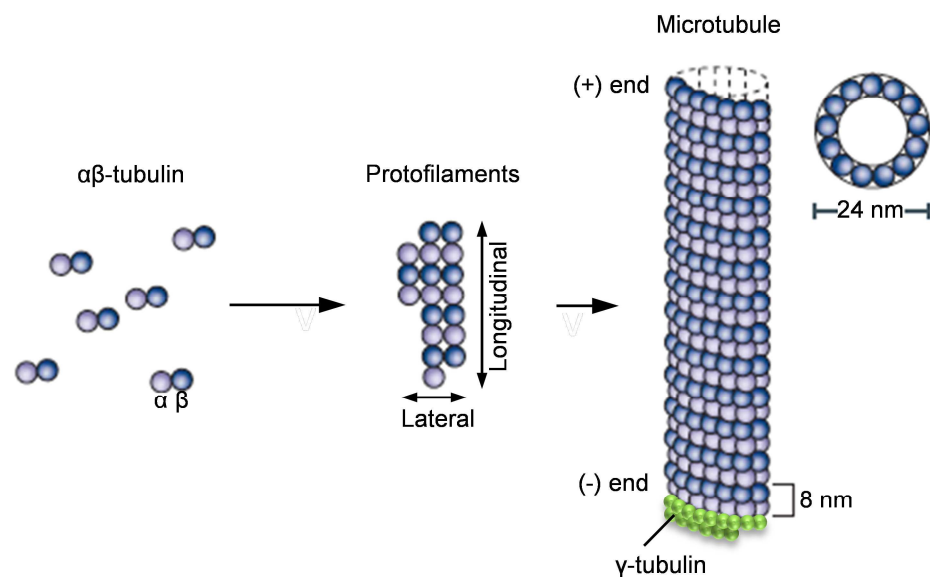
Figure 3   **Structure of microtubules.** Modified according to Jordan and Wilson.[3]

1.3.2 Dynamic microtubules – mode of action

Polymerization of microtubules occurs in two steps: a slow nucleation and a rapid elongation, thereby adding reversible and non-covalent GTP-bound tubulin dimers to the microtubule lattice.[3] GTP-bound β-tubulin is hydrolyzed to GDP and P_i upon assembly, thus forming a GTP or GDP-P_i cap. In the presence of the cap, microtubules are stabilized and can grow. GTP hydrolysis and P_i dissociation result in conformational changes of tubulin leading to a reduced binding affinity of neighboring subunits in the polymer. As a consequence, the unstable microtubule core is exposed and depolymerizes rapidly (Figure 4).[31]
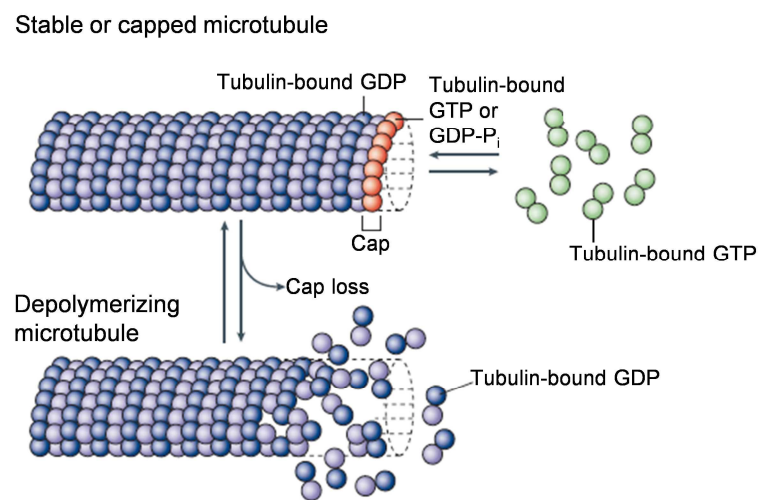
Figure 4   Polymerization and depolymerization of microtubules. Adapted according to Jordan and Wilson.[3]

Microtubules always switch between polymerization and depolymerization, a process called dynamic instability.[32, 33] Thereby, the individual microtubules ends undergo phases of growth and shortening. The (+)-ends shortens and grows more rapidly than the (-)-ends, which are capped by the γ-TuRC and embedded in the MTOC. A further dynamic behavior called 'treamilling' represents the net growth at one microtubule end and simultaneously shortening at the other end.[34] Thereby, tubulin subunits from the (+)-end flow to the (-)-end. This process has been shown to occur mainly during metaphase and anaphase.[35] Dynamic instability and treatmilling are not strictly separated; they even occur in some microtubules at the same time and depend on post-translational modifications and regulatory proteins.[36, 37]

1.3.3 Regulation of microtubule dynamics

Microtubules dynamics, properties and spatial distribution are strictly regulated and depend on different tubulin isoforms, post-translational modifications and microtubule associated proteins (MAPs). Today six α-tubulin and seven β-tubulin isoforms, varying in different tissues and cells, are known.[31] They undergo tyrosination, detyrosination, acetylation, polyglutamylation, polyglycylation, phosphorylation, and palmitoylation to achieve complete activity, however, they are not directly involved in determining the dynamic properties of microtubules.[38] In contrast, MAPs directly interact with microtubule dynamics and mediate either stabilization (*e.g.* MAP4, tau) by favoring their polymerization, or destabilization (*e.g.* stathmin, kinesin-13 family) by sequestering tubulin heterodimers and promoting depolymerization.[2]

1.3.4 Natural products that target microtubules

Since microtubules are involved in many important cellular processes, especially in cell division and motility, they represent the major target in cancer chemotherapy identified so far.[3] Many chemically diverse substances, originating from several natural sources (Table 1) are known to bind to tubulin, thereby acting as anti-mitotic, anti-proliferative or apoptosis inducing agents.[39] Besides their effects in cancer cells, some of them also show anti-angiogenic (taxanes, *Vinca* alkaloids, epothilones and tubulysins) and anti-vascular properties (combretastatins, NPI-2358) in tumor endothelial cells.[39]

Table 1   Several important MTAs of different natural sources

Origin	Drug	Microtubule binding site
Plant	Combretastatins (CA-4P, CA-1P, AVE8062)	Colchicine-binding site
	Paclitaxel (Taxol)	Taxane-binding site
	Docetaxel (Taxotere)	Taxane-binding site
	Colchicine and ZD6126	Colchicine-binding site
	Vinca alkaloids (Vincristine, Vinblastine, Vinflunine)	*Vinca*-binding site
	Taccalonolides	Taxane-binding site
Bacterial	Epothilones	Taxane-binding site
	Tubulysins	*Vinca*-binding site
Fungi	NPI-2358	Colchicine-binding site
	Phomopsin	*Vinca*-binding site

Table 1   Continued

Origin	Drug	Microtubule binding site
Marine	Hemiasterlins	*Vinca*-binding site
	Laulimalide	Taxane-binding site
	Pelorusides	Taxane-binding site
	Halichondrins	*Vinca*-binding site
	Dolastatins	*Vinca*-binding site
	Spongistatins	*Vinca*-binding site

Microtubule targeting agents (MTAs) bind to different binding sites on tubulin, thereby varying in affinity, reversibility and microtubule impact. MTAs are classified into two major groups, the microtubule stabilizers, which bind to the 'taxol'-binding site and inhibit depolymerization, and the microtubule destabilizers, which bind to the '*Vinca*'- or 'colchicine'-binding domain, thereby inducing depolymerization (Figure 5, Table 1).
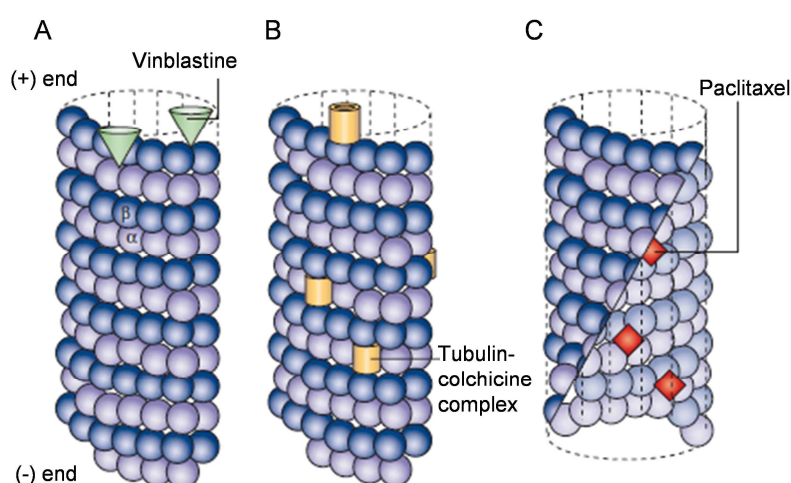
Figure 5   **MTA binding sites on microtubules. A, B:** Binding of MTAs to the *Vinca*-binding site at the (+)-end or colchicine-binding site within the microtubule lattice leads to depolymerization. **C:** MTA binding to the taxol-binding side at the inner surface of the microtubule stabilizes and inhibits depolymerization. Modified according to Jordan and Wilson.[3]

1.3.5 The big problem – resistance to MTAs

Resistance to chemotherapy with MTAs is a huge disadvantage in the combat against cancer. It is often caused by an overexpression of a class of membrane transporter proteins known as ABC-transporters (ATP-dependent drug efflux pumps or ATP-binding cassettes). These membrane pumps decrease the intracellular drug concentration, thereby reducing activity, and lead to cross-resistance (multidrug resistance, MTR) to drugs of different chemical structure. The first and most prominent known ABC-transporter

was P-glycoprotein.[40] Additionally, overexpression of one of the isotypes of βIII-tubulin[41] and changes in expression levels of MAPs (*e.g.* stathmin, MAP2,4 and tau) or mutations in α-tubulin[42, 43] were observed for vincristine and paclitaxel resistant cancer cells. Furthermore, changes of post-translational modifications at the carboxy-terminal domain of β-tubulin[44] and also alterations in the actin cytoskeleton, especially down-regulation of γ-actin, was found in vincristine resistant cancer cell lines.[45, 46] Since there are so many parameters involved in MTA resistance, the challenge will be to find new drugs, which are able to circumvent these obstacles.

1.4 Anti-vascular strategies for tumor treatment

It is well known that a functional network of blood vessels is essential for the growth, development and metastasis of solid tumors. While smaller tumors (< 2 mm) receive their oxygen and nutrients through diffusion from the surrounding tissue, bigger tumors must develop an angiogenic phenotype to ensure the oxygen and nutrient supply they need.[47] The proliferation rate of endothelial cells forming tumor vessels is much higher than compared to normal adult tissue,[48, 49] which results in abnormal vessel structure and function in almost all aspects.[50, 51] Therefore, it is not surprising that targeting the tumor vasculature offers an interesting anti-tumor strategy, which has been intensively explored in recent years.

1.4.1 'Normal' vasculature vs. tumor vasculature

The 'normal' (healthy) vasculature is arranged in a hierarchy of evenly spaced, well differentiated arteries, arterioles, capillaries, venules and veins, which are lined by the vascular endothelium. The blood flow is directed (arteries to veins) and all vessels are perfused. The vasculature consists of a luminal front directed to the plasma and connected to a basement membrane and an abluminal front, which is embedded into the glycocalyx (polysaccharide rich layer) surrounded by stabilizing fibroblasts, smooth muscle cells and the interstitial fluid (Figure 6 A). The primary function of the endothelial barrier is to separate the inner space of the blood vessel from the surrounding tissue, however, its functions as size-selective- and semipermeable barrier are important to control the exchange of cells, fluids and solutes into the surrounding tissue.[52] This so called vascular permeability is strictly regulated. Under physiological conditions, macromolecules (> 3 nm) pass the endothelial barrier transcellularly *via* caveolae mediated endocytosis or *via* vacuole-vesicular organelles. Molecules < 3 nm in diameter

use the paracellular pathway, which is mediated by the coordinated opening and closing of interendothelial cell junctions (IEJ; adherens (AJ) and tight (TJ) junctions).[53] Among AJs, vascular endothelial (VE)-cadherin is exclusively expressed in vessels and the most important transmembrane protein in barrier regulation.[54] Its extracellular domain depends on Ca^{2+} and allows homophilic interaction between two endothelial cells (ECs), whereas its intracellular domain is connected *via* α-, β-, γ- and p120-catenins to the actin cytoskeleton, providing an important link between actinomyosin contraction, VE-cadherin mediated gap formation and increased permeability. Hence, endothelial barrier function depends on both, structural and functional properties of the vasculature.

In contrast to 'normal' vasculature, tumor vasculature is immature and shows no classic hierarchy known from normal tissue. The tumor vasculature is tortuous and unevenly distributed throughout the tumor with irregular vessel diameter, excessive branching, arteriovenous shunts and blind ending vessels (Figure 6 B).[55] The blood flow is sluggish and not all open vessels are continuously perfused, which results in hypoxic and acidic regions.[55, 56] Even the structure of tumor vessels is abnormal. They are dilated, have sparsely developed vessel walls with poor expression of vascular smooth muscle cells and poor connections between pericytes and EC.[5, 57, 58] Furthermore, they have an irregular and structurally abnormal basement membrane.[59] Tumor EC are often irregularly shaped and express faint VE-cadherin accompanied by loose cell-cell connections and intercellular openings, which contribute to hyperpermeability and high interstitial fluid pressure (IFP).[60-62] In summary, compared to 'normal' vasculature, tumor vasculature is extremely leaky and not restrictive; meaning the function of a selective barrier is lost.
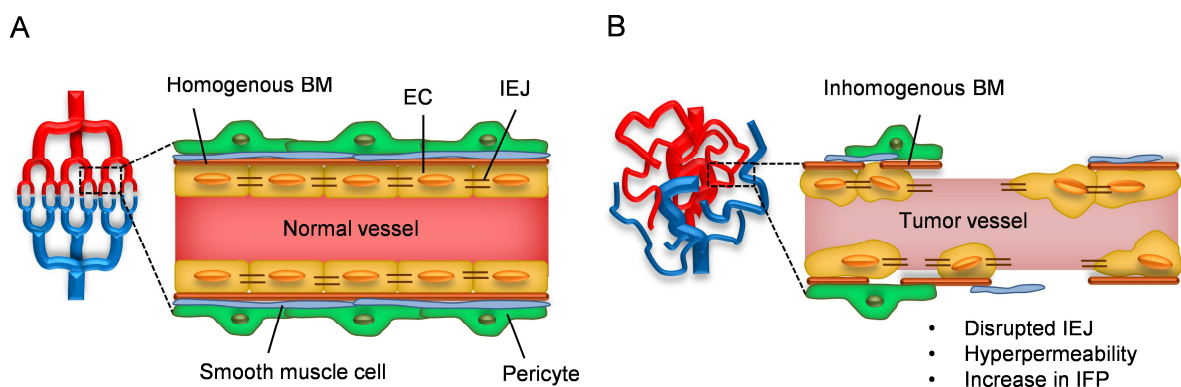
Figure 6   Structure of 'normal' vasculature *vs.* tumor vasculature. A: Normal vasculature. **B:** Tumor vasculature. BM: Basal membrane, EC: Endothelial cell, IEJ: Interendothelial junctions, IFP: Interstitial fluid pressure.

1.4.2 Angiogenesis inhibitors and vascular disrupting agents

Today there are two opposing anti-vascular approaches in clinical trials that show promising anti-tumor properties. Both differ in their treatment schedule and their way of action on their physiological target, the endothelium. The first group comprises the classic angiogenesis inhibitors (AI; *e.g.* bevacizumab or sorafenib), which are administered chronically and act on the periphery of small tumors preventing neovascularization (Figure 7 A).[63] The second group, called vascular disrupting agents (VDAs), acts in a complete different way to AIs. VDAs are administered acutely and they selectively target the already established tumor blood vessels of larger solid tumors.[63-65] As a consequence, either direct apoptotic cell death or cytoskeletal rearrangements occur, which alter the endothelial cell shape.[66, 67] These events emerge particularly in the central part of the tumor, leading to a rapid stop of blood-flow and central necrosis, which can extend to as much as 95% of the tumor mass (Figure 7 B).[68-72] Since they are effective well below their maximum tolerated dose, and lack the classic cytotoxic side effects of chemotherapeutics, they gain importance in anti-tumor treatment.[70, 73]
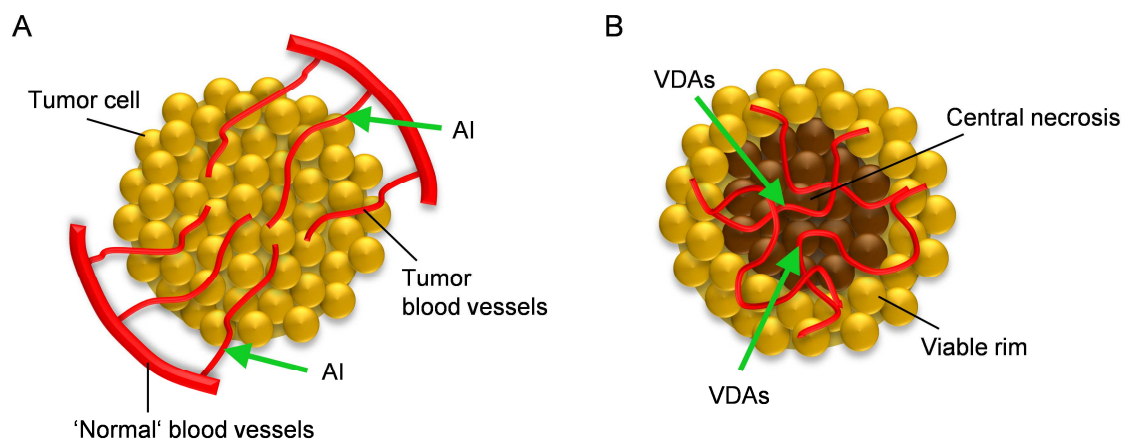
Figure 7   Anti-vascular strategies for tumor treatment. A: Angiogenesis inhibitors (AI) act on the periphery of tumors and prevent neovascularization. **B:** Vascular disrupting agents (VDAs) act on established tumor blood vessels in the central part of the tumor leading to necrosis.

1.4.3 Classes of VDAs

VDAs are divided into two classes, ligand-directed VDAs and small molecule agents (Figure 8). Ligand-directed VDAs are composed of targeting and effector moieties that are linked together usually *via* peptide bonds or chemical cross-linkers. They use antibodies, peptides or growth factors, which are coupled to pro-coagulants or toxins and selectively bind to targets on the tumor endothelium, leading to vessel occlusion.[73, 74] Small molecule agents are further subdivided into synthetic flavonoids and tubulin binding agents. The

latter bind to β-tubulin near the colchicine or *vinca*-binding side, resulting in the depolymerization of endothelial microtubules.[75] Flavonoid VDAs act in a tubulin-independent manner and trigger vascular shutdown either directly by inducing apoptosis, or indirectly by inducing local cytokine production, *e.g.* of tumor necrosis factor α (TNFα) *via* activation of nuclear factor κB (NFκB) signaling.[76-78] Since PT is a known microtubule depolymerizer (see 1.2.3), we aimed to elucidate its potential as a new small molecule VDA in this study.
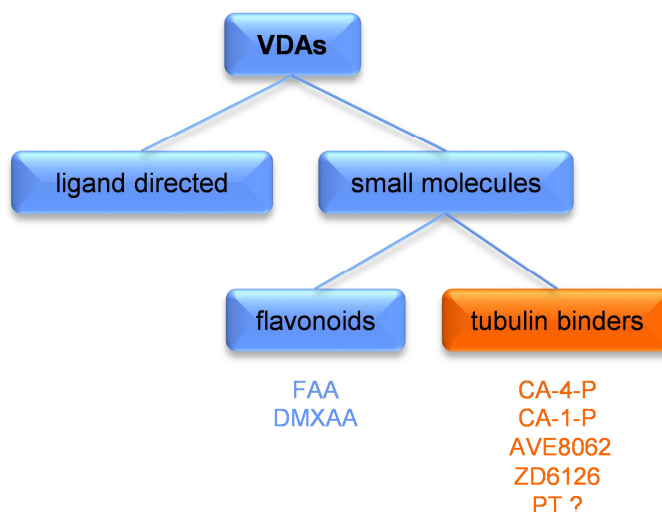
Figure 8   Classes of VDAs.

1.4.4 Mode of action of microtubule targeting VDAs

Despite the fact that certain microtubule targeting VDAs (*e.g.* CA-4-P, CA-1-P and AVE8062) have entered clinical trials, the precise mechanisms leading to the fast shutdown of tumor blood flow (within 30 min)[72] are not fully understood today. Mechanisms in terms of vessel impairment *in vitro* and *in vivo* have as yet only been described for combretastatin A4-phosphate (CA-4-P; isolated from the African bush willow tree *Combretum caffrum*), which represents the lead VDA and has already entered clinical trial phase III in anaplastic thyroid cancer.[7]

1.4.4.1   Effects on tumor vasculature

The proposed way of action is shown in Figure 9. Upon injection, the VDA (*e.g.* CA-4-P) enters ECs from the luminal side of the vasculature and binds to microtubules (step 1). This causes microtubule depolymerization, which triggers actin stress fiber formation and EC contraction. As a consequence, IEJ are disassembled and interendothelial gabs are formed (step 2), which contribute to increased permeability (step 3). The loss of the

endothelial barrier function and the concomitant protein leakage reduces the oncotic pressure differential between the inside and outside of blood vessels, thus disturbing the water balance and cause a transient increase in interstitial fluid pressure (IFP; step 4), which provoke vessel occlusion (step 5). In addition, a rapid and direct vasoconstrictive effect on tumor supplying arterioles and a decrease in longitudinal pressure differential along the vessel further facilitate the reduction in blood flow. The loss of fluid increases blood viscosity and red cells get stacked (step 6). As a consequence, vessel perfusion is disturbed, leading to a deficient supply of oxygen and nutrients followed by tumor necrosis (step 7).[5]
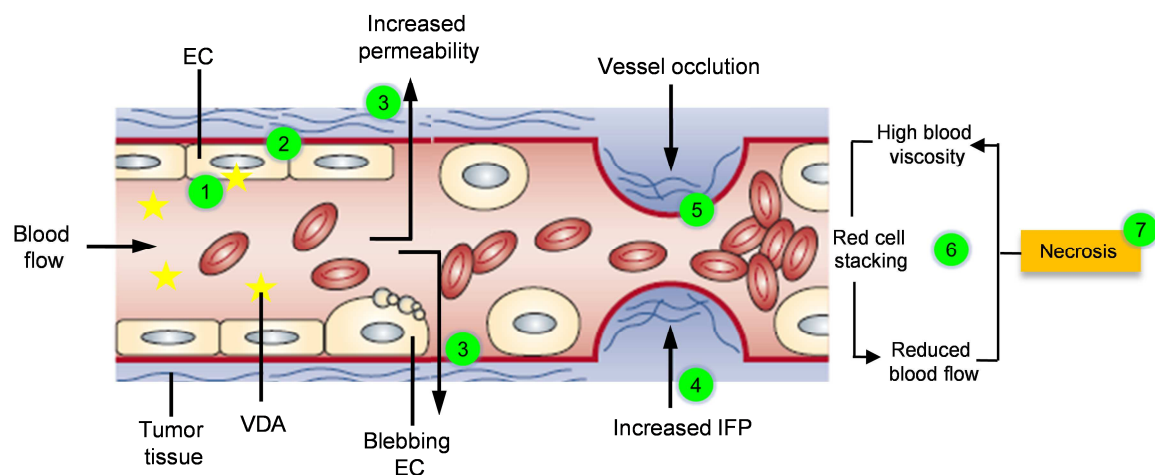
Figure 9   **Proposed mechanism leading to rapid vascular shutdown upon treatment with CA-4-P.** EC: Endothelial cell, IFP: Interstitial fluid pressure, VDA: Vascular disrupting agent. Modified according to Tozer *et al.*[5]

1.4.4.2 Effects on tumor EC

The signal process that controls vascular permeability in ECs is highly complex and the modulation varies under different stimulatory conditions. In case of microtubule binding VDAs, the depolymerization of microtubules is assumed to be the starting point of the signal cascade and triggers a very rapid (within minutes) change in the morphology of ECs (Figure 10). This goes along with the remodeling of the actin cytoskeleton and the appearance of focal adhesions.[67] Upon microtubule depolymerization, the small GTPase RhoA and its downstream effector Rho kinase (ROCK) are activated. The underlying molecular mechanism is not exactly known, but it is suggested that guanine nucleotide exchange factors (GEFs) are released from disrupted microtubules, thus activating inactive RhoA.[79] ROCK phosphorylates the myosin light chain (MLC), which in turn leads

to actinomyosin contraction and to the formation of actin stress fibers. The contractility causes an increased centripedal tension and, consequently, IEJs (especially VE-cadherin), which is connected to the actin cytoskeleton (see 1.4.1) are disassembled.[80] As a result vascular permeability increases and promotes the subsequent steps described above (1.4.4.1, Figure 9).

In addition to the activation of RhoA, ROCK and MLC, microtubule binding VDAs activate the mitogen activated protein kinase (MAPK) p38 (Figure 10).[80] Together with the actinomyosin contraction, p38 MAPK triggers an process called membrane blebbing. Hereby cells round up, F-actin accumulates in surface blebs building a spherical network that surrounds the cytoplasm, and focal adhesions appear malformed.[80] Membrane blebbing contribute to the breakdown of the endothelial barrier and represents an early phenotype of a rapid necrotic cell death, separate from the apoptotic pathway triggered by caspases.[80]
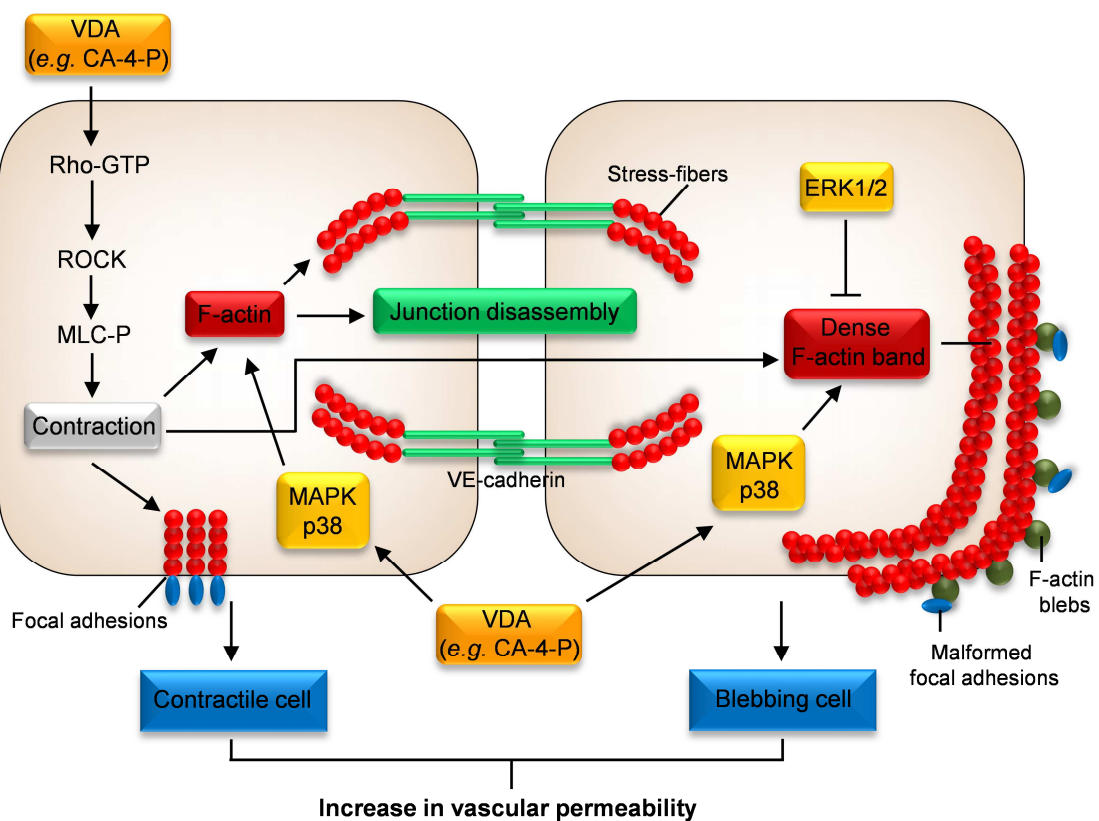
Figure 10   Signal pathway in ECs leading to barrier breakdown and vascular disruption.

1.4.5 Limitations of VDAs

After VDA treatment a viable peripheral rim of tumor cells remains (see 1.4.2; Figure 7 B), which is responsible for the rapid regrowth after a single-dose treatment.[67, 81] A common explanation for this typical VDA phenomenon is that tumor endothelial cells in the center are more accessible to VDAs, possibly due to their different morphology and the occurring high interstitial fluid pressure, which contribute to vessel occlusion when permeability increases, whereas it is tolerated at the periphery (see 1.4.1; Figure 6 B).[5, 73] Moreover, tumor blood vessels at the periphery receive their oxygen and nutrients from the surrounding healthy tissue and are therefore morphologically 'normal' and resistant to the effects of VDAs.[5] To overcome this resistance and the typical failure of tumor growth delay after a single dose, VDAs are usually combined with classic chemotherapy,[49, 82-84] radiation,[69, 85, 86] radioimmunotherapy[87, 88] or AI in preclinical and clinical trials.[89] The combination therapy enhances antitumor efficiency of VDAs; *e.g.* co-treatment with radiation allows two different approaches to act in a complementary and synergistic manner. The VDA acts on the central hypoxic and radio-resistant part of the tumor, whereas the radiation acts on the tumor endothelial cells forming the outer viable rim and promotes suppression of regrowth. Thereby, scheduled treatment and the succession of VDA application are very important to obtain tumor control.[83-85] Currently, there are several VDAs in clinical studies under intensive investigation, working as single agents or in combination.[9] Documented side effects include acute coronary and other thrombophlebitic syndromes, variance in blood pressure, heart rate, and conduction, transient flush and hot flashes, neuropathy, ataxia, and tumor pain.[90] Hence, close monitoring of cardiovascular toxicity is essential.

2 MATERIALS AND METHODS

2.1 Materials

2.1.1 Compounds

Pretubulysin (PT) was synthesized as described previously[11] and was kindly provided by Prof. Dr. U. Kazmaier (Saarland University, Saarbrücken, Germany). Combretastatin A-4 phosphate (CA-4-P) was a kind gift from OXiGENE (Waltham, MA, USA). Both compounds were stored as 10 mM stock solutions in 100% DMSO. Since in all *in vitro* experiments the final DMSO concentration did not exceed 0.1%, side effects in experimental settings could be excluded.

A

Pretubulysin (PT)

B

Combretastatin A-4-phosphate
(CA-4-P)
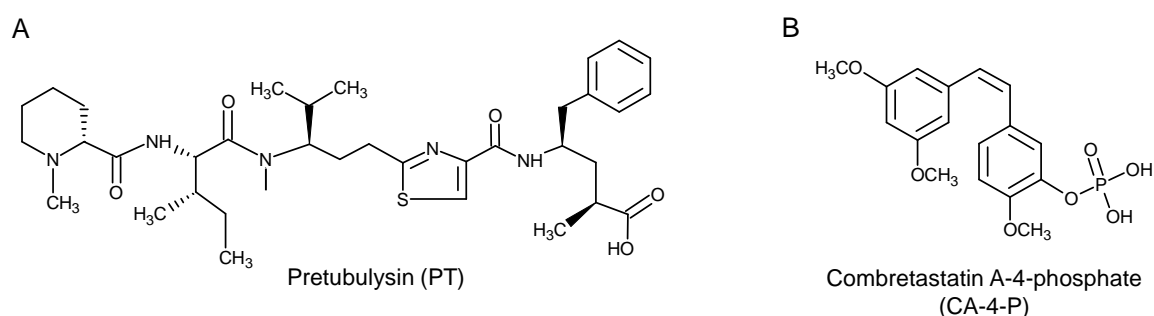
Figure 11   Chemical structure of pretubulysin (A) and combretastatin A-4-phosphate (B)

2.1.2 Biochemicals, dyes, inhibitors and cell culture reagents

Table 2   Biochemicals and dyes

Reagent	Producer
Accustain® paraformaldehyde	Sigma-Aldrich, Taufkirchen, Germany
BC Assay reagent	Interdim, Montulocon, France
Bovine serum albumin (BSA)	Sigma-Aldrich, Taufkirchen, Germany
Bradford Reagent™	Bio-Rad, Munich, Germany
Cell-Titer Blue™ Reagent	Promega, Madison, WI, USA
Coomassie brilliant blue G250	Carl Roth, Karlsruhe, Germany
DMSO	AppliChem, Darmstadt, Germany
EGTA-K	AppliChem, Darmstadt, Germany
FluorSave™ Reagent mounting medium	Merck, Darmstadt, Germany
Formaldehyde, 16% ultrapure	Polysciences Europe GmbH, Eppelheim, Germany

Table 2   Biochemicals and dyes continued

Reagent	Producer
Glutaraldehyde	Merck, Darmstadt, Germany
Histamine	Sigma-Aldrich, Taufkirchen, Germany
Matrigel™	BD Biosciences, Heidelberg, Germany
Non-fat dry milk powder (Blotto)	Carl Roth, Karlsruhe, Germany
Page Ruler™Prestained Protein Ladder	Fermentas, St. Leon-Rot, Germany
Propidium iodide	Sigma-Aldrich, Taufkirchen, Germany
Roti-Quant®	Carl-Roth, Karlsruhe, Germany
Triton X-100	Merck, Darmstadt, Germany
Tween® 20	BDH/Prolabo®, Ismaning, Germany

All other used biochemicals and dyes were obtained from Sigma-Aldrich, AppliChem, Carl Roth or Merck.

Table 3   Inhibitors

Inhibitor	Producer
Aprotinin	Sigma-Aldrich, Taufkirchen, Germany
Complete® mini EDTA free	Roche diagnostics, Penzberg, Germany
Leupeptin hemisulfate salt	Sigma-Aldrich, Taufkirchen, Germany
ML-7	Enzo Life Sciences, Lörrach, Germany
Na_3VO_4	ICN Biomedicals, Aurora, OH, USA
NaF	Merck, Darmstadt, Germany
Phenylmethylsulfonyl fluoride (PMSF)	Sigma-Aldrich, Taufkirchen, Germany
SB203580	Calbiochem, Nottingham, UK
SP600125	Sigma-Aldrich, Taufkirchen Germany
Y-27632	Cayman Chemical, Ann Arbor, MI, USA

Table 4 Cell culture reagents

Reagent	Producer
Amphotericin B 250 µg/ml	AppliChem, Darmstadt, Germany
Collagen G	Biochrom AG, Berlin, Germany
Collagenase A	Roche, Mannheim, Germany
Dulbecco's modified Eagle's medium (DMEM)	Sigma-Aldrich, Taufkirchen, Germany
Endothelial Cell Growth Medium (ECGM) with Supplement Mix #C-39215	PromoCell, Heidelberg, Germany
FCS gold	PAA Laboratories, Pasching, Austria
FCS	PAN Biotech, Aidenbach, Germany
M199 medium	PAA Laboratories, Pasching, Austria
Penicillin/Streptomycin 100x	PAA Laboratories, Pasching, Austria
RPMI 1640	PAN Biotech, Aidenbach, Germany
Trypsin	PAN Biotech, Aidenbach, Germany
EDTA disodium salt dihydrate	Carl Roth, Karlsruhe, Germany

2.2 Cell culture

2.2.1 Buffers, solutions and reagents

The following buffers, solutions and reagents were used for the isolation as well as for the cultivation of endothelial cells:

Table 5 Cell culture buffers

PBS (pH 7.4)		PBS^+ Ca^{2+}/Mg^{2+} (pH 7.4)	
NaCl	123.3 mM	NaCl	136.9 mM
Na_2HPO_4	10.4 mM	KCl	2.7 mM
KH_2PO_4	3.2 mM	Na_2HPO_4	8.1 mM
H_2O		KH_2PO_4	1.5 mM
		$MgCl_2$	0.5 mM
		$CaCl_2$	0.7 mM
		H_2O	

Table 6   Cell culture solutions

Endothelial Cell Growth Medium	
ECGM	500 ml
Supplement Mix #C-39215	23.5 ml
FCS gold	50 ml
Amphothericin B (250 µg/ml)	5 ml
Penicillin (10,000 U/ml)/ Streptomycin (10 mg/ml)	5 ml

Stopping medium	
M199	500 ml
FCS	50 ml

DMEM	
DMEM	10 g
$NaHCO_3$	0.85 g
HEPES	6 g
Amphothericin B (250 µg/ml)	5 ml
Penicillin (10,000 U/ml)/ Streptomycin (10 mg/ml)	10 ml
H_2O	ad 1000 ml

B16-F1 Cell Growth Medium	
DMEM	500 ml
FCS (not heat-inactivated)	50 ml

A-Mel-3 Cell Growth Medium	
RPMI	500 ml
FCS	50 ml
Penicillin (10,000 U/ml)/ Streptomycin (10 mg/ml)	10 ml
$NaHCO_3$	1 g

Freezing medium	
FCS gold	50%
DMSO	8%
Growth medium	

Trypsin/EDTA	
Trypsin	0.05%
EDTA	0.02%
PBS	

Collagen G	
Collagen G	0.001%
PBS	

Collagenase A (HUVEC isolation)	
Collagenase A	0.01%
PBS$^+$ Ca^{2+}/Mg^{2+}	

Before use, FCS gold (fetal calf serum) was partially thawed for 30 min at room temperature (RT), followed by total thawing at 37 °C. Afterwards FCS gold was inactivated at 56 °C for 30 min and aliquots were stored at -20 °C. FCS in DMEM medium was not heat-inactivated. All used cells were routinely tested for mycoplasma contamination using the PCR detection kit Venor[®]GeM (Minerva Biolabs, Berlin, Germany).

2.2.2 Cell lines

All cell lines were cultured in an incubator (Heraeus, Hanau, Germany) with constant humidity at 37 °C and 5% CO_2. Unless otherwise stated, 30 min before use, cell culture flasks, Petri dishes multiwell-plates, and μ-slides were coated with collagen G.

2.2.2.1 HUVECs – human umbilical vein endothelial cells

Human umbilical cords were kindly provided by Klinikum München Pasing, Wolfart Klinik Gräfelfing, Frauenklinik Dr. Krüsmann München, and Rotkreuzklinikum München in accordance with the declaration of Helsinki. Until use, umbilical cords were placed in PBS+Ca^{2+}/Mg^{2+} containing penicillin (100 U/ml) and streptomycin (100 μg/ml), and stored at 4 °C. Every week HUVECs were freshly prepared by digestion of umbilical veins with 0.1 g/liter collagenase A. After 45 min incubation at 37 °C, the digestion reaction was stopped using stopping medium. The cell suspension of each umbilical cord was centrifuged (180 g, 5 min), resuspended in endothelial growth medium, and subsequently plated in a 25 cm^2 flask. After reaching confluence, cells were trypsinized and plated in a 75 cm^2 flask. For experiments HUVECs were grown until confluence and used only at passage #3. HUVECs were used for all assays except for the permeability assays.

2.2.2.2 HMEC-1 – human dermal microvascular endothelial cells

Human Microvascular Endothelial Cells (HMEC-1) were kindly provided from the Centers for Disease Control and Prevention (CDC, Atlanta, GA, USA) and were used until they reached passage #11. The immortalized HMEC-1 cell line was created by transfection of human dermal microvascular endothelial cells with a plasmid coding for the transforming SV40 large T-antigen. This cell line shows endothelial phenotypic, morphologic, and functional characteristics.[91, 92] HMECs were solely used in permeability assays.

2.2.2.3 Hamster A-Mel-3 amelanotic melanoma cell line

The spontaneous accrued hamster amelanotic melanoma A-Mel-3 cell line, that was cultured at the institute for surgical research of the LMU, was solely used for the syngeneic hamster dorsal skinfold experiment (2.11.3). This tumor cell line has intensively been characterized[93, 94] and is able to build a stable tumor vascularization within 4 days. Hamster A-Mel-3 amelanotic melanoma cells were cultured in Roswell Memorial Institute Medium (RPMI 1640) containing heat inactivated FCS (PAN Biotech) and were solely used at passage #20.

2.2.2.4 B16-F1 – mouse skin melanoma cell line

The B16 melanoma arose spontaneously in the skin at the base of the ear of a C57BL/6 mouse, yielding in two different variants: B16-F1 and B16-F10.[95] In this study the less metastatic variant B16-F1, which is known to build highly vascularized tumors[96, 97] was used. B16-F1 cells (No. CRL-6323™) were purchased from ATCC® (American Type Culture Collection, Manassas, VA, USA) and cultivated in DMEM containing non heat-inactivated 10% FCS. B16 F-1 cells were used between passage #21 and #25 in syngeneic tumor models (2.11.4 and 2.11.5).

2.2.3 Passaging

Confluent HUVECs and HMECs were either sub-cultured 1:3 in 75 cm^2 culture flasks or were plated for experiments in dishes, multiwell-plates, E-Plates or µ-Slides. For passaging, medium was removed and cells were washed twice with PBS. Incubation with trypsin/ethylene diamine tetraacetic acid (EDTA) (T/E) followed for 1-2 min at 37 °C. Afterwards, cells were gradually detached and the digestion was stopped using stopping medium. After centrifugation (180 g, 5 min, 20 °C), the pellet was resuspended in growth medium and cells were finally plated. Confluent B16-F1 cells were treated identically but were sub-cultured 1:5 or 1:10 in 150 cm^2 culture flasks. Cell concentration and viability were determined using the ViCELL™ cell viability analyzer (Beckman Coulter, Krefeld, Germany).

2.2.4 Freezing and thawing

Usually HUVECs were used until passage #3 without intermediate freezing or thawing. Before freezing, confluent cells (HMEC-1 and B16-F1) from a 75 cm^2 flask were trypsinized, centrifuged in stopping medium (180 g, 5 min, 20 °C), and resuspended to 1 x 10^6 cells/ml in ice-cold freezing medium. 1.0 ml aliquots were frozen in cryovials at -80 °C for 24 h. Afterwards aliquots were moved to liquid nitrogen for long term storage.

For thawing one cryo-aliquot was rapidly warmed to 37 °C and the content was immediately dissolved in pre-warmed growth medium. In order to remove DMSO, cells were centrifuged again, resuspended in their suitable growth medium and transferred to a 75 cm^2 (HMEC-1) or a 25 cm^2 (B16-F1) culture flask.

2.3 Western blot analysis

2.3.1 Sample preparation

HUVECs were treated as indicated in the respective figure, followed by two washing steps on ice with ice-cold PBS. Immediately after washing, cells were lysed in modified RIPA lysis buffer for phosphoproteins or in 3x Laemmli sample buffer (MLC2, phospho-MLC2 and di-phospho MLC2) and were frozen at -80 °C. Afterwards cell samples were gently thawed on ice, were scraped off using cell scrapers (TPP, Trasadingen, Switzerland), and were transferred to pre-cooled Eppendorf tubes (Peske, Aindling-Arnhofen, Germany). After centrifugation (20,160 g, 10 min, 4 °C) one sample (5 µl) of the supernatant was diluted 1:10 in H$_2$O to determine the protein concentration by Bradford assay or by Bicinchoninic Protein Assay (BCA). The remaining supernatant was mixed with Laemmli sample buffer (3x), heated at 95 °C for 5 min and was kept frozen at -20 °C until Western blot analysis. To guarantee equal protein loading, each protein sample was adjusted by adding 1x Laemmli sample buffer before SDS PAGE.

Table 7   Buffers for protein sample preparation

Lysis buffer for phosphoproteins		3x Laemmli buffer	
Tris/HCl (pH 7.4)	50 mM	Tris/HCl (pH 6.8)	187.5 mM
NaCl	150 mM	SDS (sodium	6%
Nonidet NP 40	1%	dodecyl sulfate)	
Deoxycholic acid	0.25%	Glycerol	30%
SDS	0.1%	Bromphenol blue	0.025%
Na_3VO_4	0.3 mM	H_2O	
NaF	1.0 mM	β-Mercaptoethanol	12.5%
β-Glycerophosphate	3.0 mM		
Pyrophosphate	10 mM		
H_2O			
Freshly added:			
Complete®mini EDTAfree	4.0 mM		
PMSF	1.0 mM		
H_2O_2	600 µM		

2.3.2 Protein quantification

2.3.2.1 Bradford assay

The total amount of protein in cell lysates for Western blot analysis was determined as described previously.[98] Thereby Coomassie Brilliant Blue G250 was used to stain proteins. 10 µl samples were incubated with 190 µl Bradford solution (Roti®-Quant Bradford Reagent, Carl Roth, Karlsruhe, Germany, 1:5 dilution in H_2O) for 5 min at RT upon shaking. Afterwards, absorbance was measured photometrically at 592 nm (Tecan Sunrise Absorbance reader, TECAN, Crailsheim, Germany). Protein standards were obtained by stepwise diluting a 2 mg/ml stock solution of bovine serum albumin (BSA). Linear regression was used to determine the protein concentration of each sample.

2.3.2.2 Bicinchoninic (BCA) protein assay

The total amount of protein in cell lysates for pull down assays was determined using the BCA Protein Assay (BC Assay reagents, Interdim, Montulocon, France) as described earlier.[99] 10 µl samples were incubated with 200 µl BC Assay reagent at 37 °C for 30 min.

Afterwards absorbance of the blue complex was measured photometrically at 550 nm. Protein standards were achieved as described above (2.3.2.1).

2.3.3 SDS-PAGE

After boiling the samples for 5 min at 95 °C, equal amounts of protein were loaded onto a SDS-polyacrylamide gel consisting of a separating and a stacking gel. Proteins were separated according to Laemmli et al.,[100] by discontinuous SDS-polyacrylamide gel electrophoresis (SDS-PAGE) using the Mini-PROTEAN 3 electrophoresis module (Bio-Rad, Munich, Germany). To achieve optimal separation of proteins, the concentration of acrylamide (Rotiphorese™ Gel 30, Carl Roth GmbH & Co. KG, Karlsruhe, Germany) in the separating gel was adjusted to the respective molecular weight. Electrophoresis was performed at 100 V for 21 min (protein stacking) and at 200 V for 45 min (protein separation). To identify the molecular weight of proteins, samples were compared with a pre-stained protein ladder (PageRuler™, Fermentas, St. Leon-Rot, Germany) which was additionally load on the SDS gel.

Table 8   Acrylamide concentration in the separation gel

Protein	Acrylamide conc.
p38, phospho-p38, MYPT-1, phospho-MYPT-1	10%
ERK1/2, phospho-ERK1/2, JNK, phospho-JNK	12%
MLC2, phospho-MLC2, di-phospho-MLC2, HSP27, phopho-HSP27, RhoA	15%

Table 9   Acrylamide gels

Separating gel 10%/12%/15%		Stacking gel	
Rotiphorese™ Gel 30	33.3%/40%/49.7%	Rotiphorese™ Gel 30	17%
Tris (pH 8.8)	375 mM	Tris (pH 6.8)	125 mM
SDS	0.1%	SDS	0.1%
TEMED	0.1%	TEMED	0.2%
APS	0.05%	APS	0.1%
H_2O		H_2O	

Table 10   Electrophoresis buffer

Electrophoresis buffer	
Tris	4.9 mM
Glycine	38 mM
SDS	0.1%
H_2O	

2.3.4 Tank electroblotting

After protein separation, proteins were transferred to a nitrocellulose membrane (Hybond-ECL™, Amersham Bioscience, Freiburg, Germany) *via* tank electroblotting.[101] A blotting sandwich, which was prepared in a box filled with cold 1x tank buffer, was used for bubble free electroblotting. The assembly of the sandwich was as follows: cathode–pad–blotting paper–separating gel (SDS-PAGE)–nitrocellulose membrane–blotting paper–pad–anode. The membrane was equilibrated for 30 min in 1x tank buffer before starting the tank blot. Sandwiches were mounted in the Mini Trans-Blot® system (Bio-Rad, Munich, Germany) and the chamber was filled with cold 1x tank buffer. To avoid excessive heat, a cooling pack was additionally inserted. Transfers were carried out at 4 °C, 100 V for 90 min.

Table 11   Tank blotting buffer

5x Tank buffer		1x Tank buffer	
Tris base	240 mM	5x Tank buffer	20%
Glycine	195 mM	Methanol	20%
H_2O		H_2O	

2.3.5 Protein detection

2.3.5.1 Control-staining of polyacrylamide gels

To verify protein loading and homogeneity, polyacrylamide gels were stained after tank elektroblotting with Coomassie blue for 15 min. To visualize proteins the excess of Coomassie blue was removed using the Coomassie-destaining solution.

Table 12   Coomassie staining and de-staining solutions

Coomassie staining solution		Coomassie de-staining solution	
Coomassie blue	3.0 g	Glacial acetic acid	100 ml
Glacial acetic acid	100 ml	Ethanol	333 ml
Ethanol	450 ml		
H_2O	ad 1 l	H_2O	ad 1 l

2.3.5.2 Protein detection on nitrocellulose membranes

Prior to the immunological detection of the relevant proteins, unspecific protein binding was blocked at RT using either non-fat dry milk powder 5% (Blotto) or BSA 5% for 2 h. Afterwards the membranes were incubated overnight at 4 °C with the respective primary antibody dissolved either in Blotto or BSA (Table 13). After four washing steps with PBS containing 0.1% Tween® 20 (PBS-T), the membrane was incubated with the secondary antibody (Table 14) at RT, followed by four washing steps with PBS-T and one washing step with PBS. All incubation steps were performed under gentle agitation. To visualize the proteins, two different methods were used, depending on the labels of the secondary antibodies: enhanced chemiluminescence or infrared imaging.

2.3.5.2.1 Enhanced chemiluminescence

Membranes were incubated for 2 h with secondary antibodies conjugated to horseradish peroxidase (HRP) (Table 14). For protein detection, luminol (5-amino-2,3-dihydro-1,4-phtalazinedione) served as substrate. The membrane was either incubated with a homemade ECL (enhanced chemiluminescence) solution (2.5 mM luminol, 1 mM p-coumaric acid, 1 M Tris-Base pH 8.5, 30% H_2O_2 and dH_2O) or with a purchased ECL solution (ECL Plus Western Blotting Detection Reagent RPN 2132, GE Healthcare, Munich, Germany) for 1 min in the dark. Luminescence was detected by exposure of the membrane to an X-ray film (Super RX, Fuji, Düsseldorf, Germany), which was developed using the Curix 60 Developing system (Agfa-Gevaert AG, Cologne, Germany) protected from light.

2.3.5.2.2 Infrared imaging

Secondary antibodies coupled to IR(infrared)Dye™ 800 and Alexa Fluor® 680 with emission at 800 and 700 nm, respectively, were used. Membranes were incubated for 1 h followed by four washing steps with PBS-T and one washing step with PBS. Afterwards

protein bands of interest were detected using the Odyssey imaging system (Li-COR Biosciences, Lincoln, NE). Used secondary antibodies are listed in Table 14.

Table 13   Primary antibodies

Antigen	Source	Dilution	In	Provider
β-actin (C4)	mouse monocl.	1:1,000	Blotto 5%	Millipore
β-tubulin	rabbit polycl.	1:1,000	Blotto 5%	Cell Signaling
HSP27	mouse monocl.	1:500	BSA 5%	Cell Signaling
phos.-HSP27^{Ser82}	rabbit polycl.	1:500	BSA 5%	Cell Signaling
ERK1/2	rabbit polycl.	1:1,000	BSA 5%	Cell Signaling
phos.-ERK1/2$^{T202/Y204}$	mouse monocl.	1:1,000	BSA 5%	Cell Signaling
JNK	rabbit polycl.	1:500	BSA 5%	Cell Signaling
phos.-JNK$^{T183/Y185}$	rabbit polycl.	1:500	BSA 5%	Cell Signaling
MLC2 (FL-172)	rabbit polycl.	1:500	Blotto 5%	Santa Cruz
phos.-MLC2^{Ser19}	mouse monocl.	1:1,000	Blotto 5%	Cell Signaling
phos.-MLC2$^{T18/S19}$	rabbit polycl.	1:1,000	BSA 5%	Cell Signaling
MYPT1 (H-130)	rabbit polycl.	1:500	Blotto 5%	Santa Cruz
phos.-MYPT1^{Thr696}	rabbit polyc.l	1:500	Blotto 5%	Millipore
p38	rabbit polycl.	1:1,000	BSA 5%	Cell Signaling
phos.-p38$^{T180/Y182}$	rabbit polycl.	1:1,000	BSA 5%	Cell Signaling
RhoA	mouse monocl.	1:666	BSA 3%	Thermo Scientific

Table 14   Secondary antibodies

Antibody	Dilution	In	Provider
Goat anti-mouse IgG1 HRP	1:1,000	Blotto 1%	Biozol
Goat anti-rabbit HRP	1:10,000	Blotto 1%	Dianova
Alexa Fluor® 680 goat anti-mouse IgG	1:10,000	Blotto 1%	Molecular Probes
IRDye™ 800W goat anti-rabbit IgG	1:10,000	Blotto 1%	LI-COR Biosciences

2.4 Active RhoA Pull-Down assay

HUVECs were grown to confluence in 100 mm dishes and treated with vehicle control or PT as indicated. Active RhoA isolation was performed according to the manufacturer´s protocol (Active Rho Pull-Down and Detection Kit No. 16116, Thermo Scientific, Rockford, IL, USA). An immobilized glutathione, which has been covalently attached to agarose-resin beats, binds to glutathione-S-transferase (GST)-fusion proteins of the Rhotekin-bining domain (RBD), which specifically pull down active RhoA out of the whole cell lysate. After purification, protein concentrations were determined by the BCA Protein Assay (2.3.2.2.), mixed with 2x Laemmli sample buffer (Kit), and stored at -20 °C until SDS-PAGE and Western Blot analysis (2.4). After Western blot analysis, quantification was carried out using the ImageJ 1.45s software (National Institutes of Health, USA).
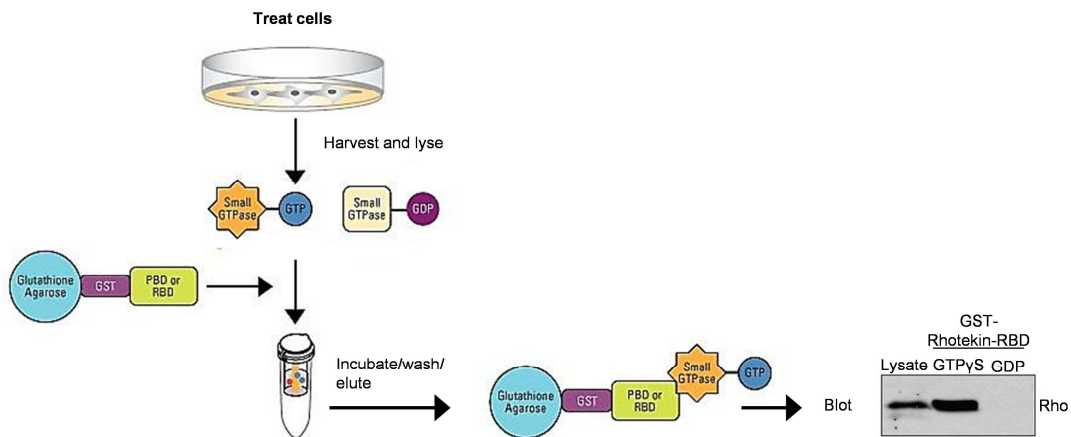
Figure 12   Schematic overview about the functional principle of the RhoA pull-down assay. Adapted according to Thermo Scientific (www.piercenet.com).

2.5 Immunocytochemistry and confocal laser scanning microscopy

Immunofluorescence images of fixed cells were obtained by using a Zeiss LSM 510 META confocal microscope (Zeiss, Oberkochen, Germany) and 40x or 63x oil immersions objectives, respectively.

2.5.1 F-actin, pp-MLC2, and EC junction staining

HUVECs were cultured to confluence on 8-well μ-Slides (ibiTreat; IBIDI GmbH, Martinsried, Germany) and incubated with PT as indicated. For stainings using inhibitors, HUVECs were either pre-treated for 30 min (Y-27632, 10 μM) or for 1 h (SB203580, 20

µM or SP600125, 25 µM), followed by 1 h PT treatment. After stimulation cells were washed with warm PBS$^+$ (Ca^{2+}/Mg^{2+}), fixed for 10 min with 10% Accustain$^®$ paraformaldehyde at RT (ppMLC, vinculin and F-actin), or with ice-cold acetone at -20 °C for 10 min (VE-cadherin, claudin-5 and F-actin). After three washing steps with PBS, cells were permeabilized (only ppMLC, vinculin and F-actin) for 30 min with 0.2% Triton X-100/ 0.1% Tween$^®$ 20 in PBS. Washed cells were incubated for 20 min with 2% BSA in PBS to block unspecific binding. Afterwards cells were incubated over night at 4 °C with the primary antibody (Table 15). Following three washing steps with PBS, cells were incubated for 1 h at RT with the respective AlexaFluor$^®$-labeled secondary antibody, with rhodamine-phalloidine for F-actin staining, or with Hoechst 33342 (Bisbenzimide) for nuclei staining (Table 16). After three washing steps, cells were embedded in FluorSave™ Reagent mounting medium and covered with 8 mm x 8 mm glass coverslips (custom made by Helmut Saur Laborbedarf, Reutlingen, Germany). Slides were stored at 4 °C protected from light until use.

2.5.2 Microtubule staining

HUVECs were cultured as described above, and were treated with PT or CA-4P as indicated. To visualize solely polymerized microtubules and to diminish background staining, monomeric and dimeric tubulin subunits were removed using the cell extraction buffer (CEB; 80 mM PIPES pH 6.9, 1 mM MgCl$_2$, 5 mM EGTA-K and 0.5% TritonX-100). After incubation for 30 s, cells were fixed for 10 min by adding glutaraldehyde to final 0.5%. Redundant glutaraldehyde was removed and quenched for 7 min with 0.1% NaBH$_4$ in PBS. After washing with PBS, cells were blocked and stained as described in (2.5.1.).

Table 15   Primary antibodies

Antigen	Source	Dilution	In	Provider
Claudin-5	rabbit polycl.	1:50	BSA 0.2%	Invitrogen
phos.-MLC2$^{T18/S19}$	rabbit polycl.	1:400	BSA 2%	Cell Signaling
VE-cadherin (F-8)	mouse monocl.	1:400	BSA 0.2%	Santa Cruz
Vinculin (clone hVIN-1)	mouse monocl.	1:100	BSA 2%	Sigma-Aldrich
α-tubulin	rabbit polycl.	1:400	BSA 0.2%	Abcam

Table 16   Secondary antibodies and dyes

Antibody/dye	Dilution	In	Provider
Alexa Fluor® 633 goat anti-mouse IgG	1:400	BSA 0.2%	Molecular Probes
Alexa Fluor® 488 goat anti-rabbit IgG	1:400	BSA 0.2%	Molecular Probes
Alexa Fluor® 488 goat anti-mouse IgG	1:400	BSA 0.2%	Molecular Probes
Hoechst 33342 (Bisbenzimide)	1:1000	BSA 0.2%	Sigma-Aldrich
Rhodamine phalloidine	1:400	BSA 0.2%	Molecular Probes

2.6 Permeability assays

2.6.1 Impedance measurement

Changes in endothelial permeability were measured by impedance sensing using the xCELLigence Real-time-cell-analyzer (RTCA) DP Instrument (Roche, Penzberg, Germany), consisting of the RTCA control unit, the RTCA DP station, which was placed in a humidified incubator maintained at 37 °C with 5% CO_2, and the E-Plate16 (Figure 13). The electronic sensors at the bottom of the E-Plate 16 provided a continuous and quantitative measurement of cell index (CI) in each well, which represents a dimensionless value derived from measured electrical impedance changes. 4 x 10^4 HMECs per well were seeded on gold electrodes and grown up to 2.5 days to obtain confluency. At CI maximum, normalization was performed and HMECs were treated with PT as indicated. Impedance was measured at 25 kHz every 10 s up to 12 h. Quantitative analysis was performed at time-point 1 h after PT treatment.
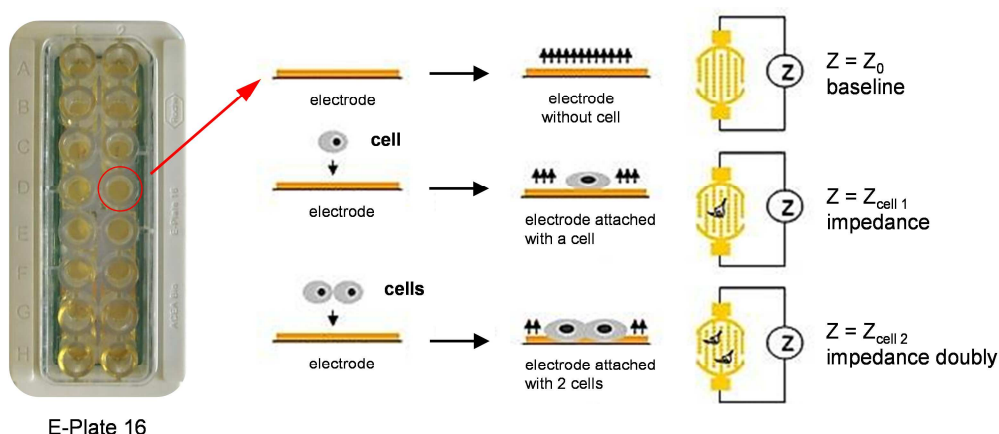

Figure 13   Principle of impedance sensing using the E-Plate 16. Attachment of cells to the electrode (yellow) affect the local ionic environment, thus leading to an increase in impedance. Partially adapted according to ACEA Biosciences (www.aceabio.com).

2.6.2 Macromolecular permeability assay

HMECs were grown to confluency on collagen G-coated 12-well Transswell® inserts (0.4 µm; Corning, New York, NY, USA). Shortly before PT treatment, fluorescein isothiocyanate (FITC)-dextran (40 kDa; 1 mg/ml; Sigma-Alrich, Taufkirchen, Germany) was used as a tracer and added to the upper compartment of the Transswell® chamber. HMECs were treated with PT as indicated. After 30, 60, 120, and 240 min, the amount of FITC-dextran in the lower compartment was determined by a SpectraFluorPlus plate reader (ex: 485 nm, em: 535 nm; Tecan, Crailsheim, Germany). Mean fluorescence of samples from untreated cells at t = 4 h was defined as 1.
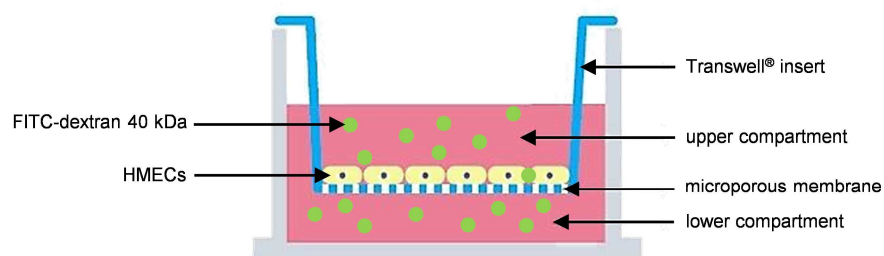
Figure 14   Scheme of a Transswell® insert in combination with a HMEC monolayer. Partially adapted according to Genetimes Technology (www.genetimes.hk).

2.7 Cell viability assays

2.7.1 CellTiter-Blue® cell viability assay

Metabolic activity was measured by the CellTiter-Blue® Reagent, which uses resazurin as an indicator dye of cell viability. Resazurin (non-fluorescent) is reduced by viable cells into resorufin (highly fluorescent). The assay was performed according to the manufacturer´s protocol (Promega Corp., Madison, WI, USA). HUVECs were grown to confluency in 96-well plates and were either simultaneously treated with PT and resazurin (4 h) or were pre-treated with PT for 22 h, and then resazurin was added for 4 h. Fluorescence (ex: 560 nm; em: 590 nm) was detected by a SpectraFluorPlus plate reader, which correlates to the number of viable cells.

2.7.2 Flow cytometry

This method was used to determine apoptotic and necrotic cells as well as for cell cycle measurement upon treatment with PT. Therefore two different FACS machines, the FACSCalibur (apoptosis, cell cycle) and the FACSCanto II (necrosis; both Becton Dickinson, Heidelberg, Germany) were used. The necessary FACS buffers were either self-made (FACSCalibur, Table 17) or were purchased from BD Biosciences (FACSCanto II, BD FACSFlow™ No. 342003).

Table 17   FACS buffer for FACSCalibur

Sheat fluid pH 7.4	
NaCl	8.1 g
KH_2PO_4	0.3 g
Na_2HPO_4	2.4 g
KCl	0.3 g
Na_2EDTA	0.4 g
LiCl	0.4 g
NaN_3	10 mM
H_2O	ad 1 l

2.7.2.1 Quantification of apoptotic cell death

Quantification of apoptosis was carried out as described by Nicoletti *et al.*[102] by counting the nuclei with subdiploid DNA content after staining with propidium iodide (PI). Confluent HUVECs, grown in 24-well plates, were either left untreated (control) or were pretreated with PT as indicated. After treatment, the supernatant of each well was collected and cells were washed two times with PBS. Afterwards, cells were trypsinized with T/E, resuspended in the supernatant and centrifuged (10 min, 4 °C, 600 g). Following two washing steps with PBS and subsequent centrifugation (10 min, 4 °C, 600 g), cells were incubated in a hypotonic fluorochrome solution (HFS) overnight. Cells were analyzed by flow cytometry (FACSCalibur), whereby events left of the G0/G1 peak in the histogram were considered as apoptotic cells.

Table 18   HFS solution

HFS solution	
Sodium citrate	0.1%
Triton X-100	0.1%
Propidium iodide	50 µg/ml
PBS	ad 1 ml

2.7.2.2 Cell cycle analysis

After incubation in HFS solution (see above) HUVECs were measured by using the fluorescence channel 2 (FL2, em: 585) in the logarithmic mode. Since PI intercalates in the DNA and PI-fluorescence depends on the status of cellular chromatin, the different cell cycle phases can be distinguished. Most cells are in the G0/G1 cell cycle phase with 2n chromosome set (= diploid), lacking the sister chromatids. Cells in the G2/M phase are in the process of cell division, meaning that these cells have a 2n chromosome set, but furthermore the sister chromatides as duplicates (= tetraploid). The additional sister chromatide allows the differentiation of the G2/M-phase to G0/G1-phase, which results in a higher fluorescence peak due to the increased amount of propidium-iodide intercalation. The S-phase is the synthesis phase. In this phase the chromatids duplicated and the fluorescence peak is located between the fluorescence peaks of G0/G1 and G2/M-phase. Using the Flow cytometry analysis software FlowJo 7.6, regions for each fluorescence peak according to their chromatin states (percentages of cells in the single cell cycle states) were measured and set into relation of the total cell number.

2.7.2.3 Quantification of necrotic cell death

To assess the number of cells undergoing necrosis or late apoptosis, PI-staining was performed. Confluent HUVECs grown in 24-well plates were pretreated with PT as indicated. After treatment, cells were incubated with 10 µg/ml PI at 37 °C for 30 min. One control well was incubated with 0.01% Triton and served as positive control. The supernatant of each well was collected and centrifuged for 10 min at 600 g. In parallel, the remaining cells were washed two times with PBS and trypsinized with T/E. After centrifugation the supernatant was removed and trypsinized cells (in stopping medium) were added. Following centrifugation for 10 min at 600 g, cells were analyzed by flow cytometry (FACSCanto II).

2.7.3 Monitoring of morphological changes

HUVECs were cultured to confluence in 24-well plates and were treated with PT as indicated. After 1 h and 24 h images were taken using a Canon EOS 450 D digital camera and a Zeiss-Axiovert-25 microscope (10x objective; Zeiss, Oberkochen, Germany). Afterwards HUVECs were washed twice with PBS and fresh ECGM was added. 24 h later images of the same wells were taken again.

2.8 VE-cadherin quantification *via* FACS analysis

The amount of extracellular VE-cadherin upon PT treatment was determined by FACS analysis as described in (2.7.2.). Confluent HUVECs were treated as indicated, fixed for 10 minutes in 4% methanol-free formaldehyde (Polyscience, Warrington, PA, USA), centrifuged (10 min, 219 g, RT), washed with PBS and centrifuged again. After incubation with anti-VE-cadherin-FITC antibody (1 h, RT) extracellular VE-cadherin was detected by flow cytometry (FACSCanto II).

Table 19   Primary antibody

Antigen	Source	Dilution	Provider
VE-cadherin (CD144)-FITC	rabbit polycl.	1:14 in PBS	Acris Antibodies

2.9 Endothelial tube disruption assays

2.9.1 Tube disruption (*in vitro*)

μ-slide angiogenesis (Ibidi GmbH) were coated with cold Matrigel® by adding 10 μl to the lower compartment of the slide. After setting (37 °C, 30 min), 1.2×10^4 HUVECs in ECGM were seeded onto the Matrigel®, and grew until thin endothelial tubes become visible (approx. 16 h). Established tubes were treated with PT as indicated and images of each well were taken using the TILLvisION 4.0.1.2 (TILL Photonics, Gräfelfing, Germany) system with an Axiovert 200 microscope (10x objective; Zeiss, Jena, Germany). The images were analyzed with the tube formation module of WIMASIS Image Analysis (Munich, Germany), which identifies cellular tubes on a variety of parameters (*e.g.* depending on brightness and contrast differences, length and width of structure) by an

automated mathematic algorithm. Drug effects were assessed at time point 6 h after treatment, analyzing total tube length, total tubes, and total branching points.

2.9.2 Mouse aortic ring assay (*ex vivo*)

Aortae from adult female C57BL/6 mice were prepared in PBS, cleaned from fat tissue, cut and embedded into Matrigel®. After 30 min incubation at 37 °C, aortic rings were covered with ECGM. Once endothelial cell sprouting occurred (after 10 d), aortic rings were treated with PT as indicated and images were taken using a Zeiss Axiovert 200 inverted light microscope (10x objective; Zeiss) connected to an IMAGO-QE camera and the appending software TILLvisION 4.0.1.2. (TILL Photonics). One representative image of 14 aortic rings prepared from six different mice aortae (animal #1 and #6: 3 rings, each; animal #2: 4 rings; animal #3 and #5: 1 ring, each; animal #4: 2 rings) is shown. Quantification was carried out using the ImageJ 1.45s software.

2.10 Cytosolic calcium imaging

Intracellular calcium measurement was carried out using a static tempered system. The fluorescent dye Fura-2[103] was used to detect ratiometrically changes of cytosolic calcium concentrations. Upon calcium binding, the excitation maximum of Fura-2 is shifted from 380 nm to 340 nm, whereas the emission wavelength of 510 nm remains unchanged. This results in a direct correlation between the emission ratio of 340/380 and the amount of cytosolic calcium. For measurements, a membrane permeable derivative named Fura-2-acetoxymethyl ester (Fura-2-AM, Biotrend, Cologne, Germany), which is cleaved to Fura-2 by cellular esterases after passing the membrane, was used. HUVECs were grown to confluency on 8-well µ-slides (Ibidi GmbH) and incubated for 30 min at 37 °C with 2 µM Fura-2-AM in HEPES buffer (Table 20). Afterwards cells were washed twice (HEPES) and treated with PT as indicated. Fluorescence measurements were performed at 37 °C, 80% humidity and 5,2% CO_2 under light protection. For each sample, a total period of 55 min with images being acquired every 5 s was analyzed with the TILLvisION Software 4.0.1.2 (TILL Photonics). Each data point of the different graphs was calculated from a randomly chosen rectangle containing at least 25 adjacent cells, of which mean values are expressed. To obtain a positive calcium signal and to confirm that cells are still alive after PT treatment, 10 µM histamine was added at time point 45 min and data were recorded for further 10 min. For data acquisition, a Zeiss Axiovert 200 M (40x objective; Zeiss) microscope, a polychromator illumination system (VisiChrome High Speed, Xenon lamp,

Visitron Systems, Puchheim, Germany) and a thermoelectric-cooled CCD camera (Photometrics Coolsnap HQ, Visitron Systems) were utilized.

Table 20   HEPES buffer for Ca^{2+} measurement

HEPES buffer (pH 7.4)	
$CaCl_2$	2.5 mM
NaCl	125 mM
NaH_2PO_4	1.3 mM
$MgCl_2$	1.5 mM
KCl	3 mM
HEPES	10 mM
Glucose	10 mM
H_2O	

2.11 *In vivo* experiments

2.11.1 Animals

All animal care and experimental procedures were in accordance with the local animal protection legislation (Government of Upper Bavaria). Experiments were carried out using male Syrian golden hamsters (6-8 weeks old, 60 ± 5 g body weight) and female C57BL/6 mice (6-12 weeks old, 20 ± 5 g body weight) both purchased from Charles River (Sulzbach, Germany). The animals were maintained in a specific pathogen-free environment, with food and water provided *ad libitum*.

2.11.2 Determining the maximum tolerated dose (MTD) of PT

Different concentrations of PT (1, 10, 30 and 50 mg/kg in PBS) were injected intravenously (IV) into the tail vein of female C57BL/6 mice. Weight was measured every day up to 8 days.

2.11.3 Hamster dorsal skinfold chamber measurement

This experiment was carried out in cooperation with Donata Gellrich from the Walter-Brendel-Center for Experimental Medicine (LMU Munich).

To perform quantitative fluorescence analysis of tumor microcirculation *in vivo*, a dorsal skinfold chamber consisting of two titanium plates was surgically implanted into the dorsal skin as described earlier.[93, 94, 104] 24 h after microsurgery, the chambers were proven to fulfill the criteria of an intact microcirculation and if they passed, a dense tumor cell suspension (2 µl, ~2 x 10^5 cells) of the hamster A-Mel-3 amelanotic melanoma was inoculated onto the striated skin muscle layer. For intravenous (IV) injection of fluorescent tracers and PT, permanently indwelling fine polyethylene catheters (PE10, inner diameter 0.28 mm, Portex, Hythe, UK) were additionally implanted into the right jugular vein, seven days upon tumor cell inoculation. All surgical procedures were performed under intraperitoneal anesthesia with ketamine (100 mg/kg b.w., Ketavet®; Parke-Davis, Berlin, Germany) and xylazine (10mg/kg b.w., Rompun®; Bayer, Leverkusen, Germany), and animals were kept warm using common heating plates. Ten days after tumor cell implantation, intravital microscopy was performed. The awake animals were immobilized in a Perspex tube on a purpose build stage (Effenberger, Munich, Germany) under a modified Zeiss microscope (Axiotech vario; Zeiss, Oberkochen, Germany). To visualize tumor microcirculation, fluorescein isothiocyanate (FITC-)labeled dextran (MW 500 kDa; 0.05-0.1 ml of a 5% solution in 0.9% NaCl; Sigma, Deisenhofen, Germany) was injected IV prior to PT injection, and determination of the baseline followed. A total of 5 regions of interest (ROIs) per animal were randomly selected and FITC-labeled plasma was selectively observed by epi-illumination with a 100 W mercury vapour lamp and specific fluorescence filter sets (excitation 450-490 nm, emission ≥ 515 nm). Directly upon FITC injection, 10 mg/kg PT or vehicle control (5% DMSO) was administered IV and data were recorded for 30, 60 and 120 min. Three microcirculation parameters in each of the five ROIs per animal were quantified: capillary red blood cell velocity (v_{RBC} in mm/s), capillary diameter (D in µm) and functional vessel density (*FVD* in 1/mm) defined as the total length of perfused capillaries per area. The images acquired by a CCD camera (Sony XC-77CE; Sony, Cologne, Germany) were recorded on digital video tape (Sony DVCAM DSV 45P; Sony, Cologne, Germany) and quantitative assessment of microcirculatory parameters and tumor growth was performed off-line using the Cap Image software (Zeintl, Heidelberg, Germany) as described in detail by Zeintl[105] and Klyscz.[106] Vessel diameters and red blood cell velocity were measured in at least 3 vessels per ROI in order to improve the steadiness of data analysis.
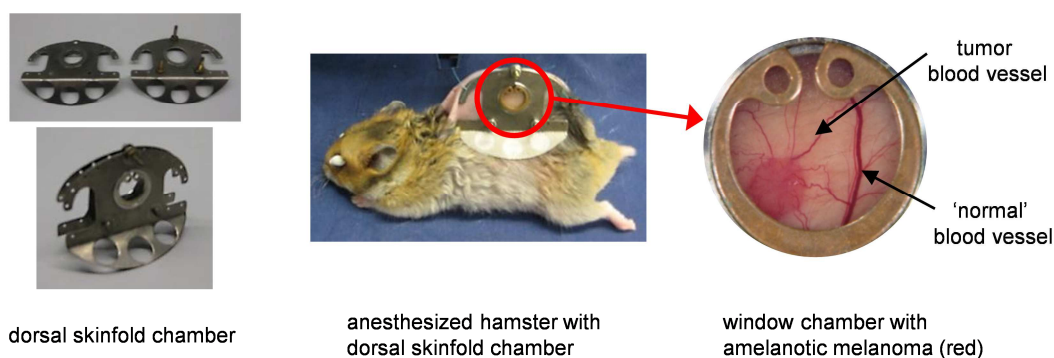
| dorsal skinfold chamber | anesthesized hamster with dorsal skinfold chamber | window chamber with amelanotic melanoma (red) |

Figure 15   Images of dorsal skinfold chamber preparation. Window chamber image (right) kindly provided by Donata Gellrich.

2.11.4 B16-F1 mouse melanoma tumor model (single dose)

C57BL/6 mice were injected subcutaneously (s.c.) into the left hind limb with 100 µl of a 1×10^6 B16-F1 mouse melanoma cell suspension in PBS, using a 0.40 x 20 mm needle and a 0.01 – 1 ml Inject-F Tuberculin Luer solo syringe (B. Braun, Melsungen, Germany). The mice were entered into experiments once tumors reached a size of approximately 650 mm^3 (assessed by π/6 x width x height x length). PT was prepared in PBS and injected IV into the tail vein at a dose of 10 mg/kg, using a 0.30 x 12 mm needle (B. Braun). Control mice received IV 5% DMSO in PBS. 24 h after treatment, 10 mg/kg of the perfusion marker Hoechst 33342 (Sigma-Aldrich) was injected IV 1 min before tumor removal. After tumor preparation, one half of the tumor was flash frozen in frozen section medium (Thermo Fisher Scientific, Bonn, Germany) (2.11.4.1), and the second tumor-half was fixed in 4% (4 days) and 1% (1 week) paraformaldehyde (2.11.4.2).

2.11.4.1 Quantification of Hoechst 33342 perfusion and vessel density

10 µm cryo-sections were prepared using a microtome cryostate HM 500 (Microm, Walldorf, Germany) to visualize Hoechst 33342 perfusion and vessel density (CD31). Upon air-drying (15 min, RT) tumor-sections were washed twice in PBS, were fixed for 10 min in 4% paraformaldehyde and were blocked with 2% BSA containing 0.5% Triton X-100 for 30 min. Afterwards tumor sections were incubated with an rat anti-mouse CD31 monoclonal antibody (BD Pharmingen^{TM}, Heidelberg, Germany) 1:100, over night at 4 °C. Secondary antibody Alexa Fluor® 546 goat anti-rat 1:400 for 2 h (Invitrogen, Karlsruhe, Germany) was used for detection. Hoechst 33342 and CD31 staining were visualized using a Zeiss LSM 510 Meta confocal microscope and a 40x magnification. Overall thirteen random fields at the tumor periphery as well as in the tumor center of two sections per tumor were analyzed. For quantification, Hoechst 33342 fluorescence intensity was

determined using ImageJ 1.44p software according to Grosios *et al*[107] and vessel density was quantified by counting CD31 pos. vessel-like structures.

2.11.4.2 Haematoxylin and eosin staining (H&E)

After paraformaldehyde fixation, dehydration and paraffin embedding, 5 µm tumor sections of PT (10 mg/kg, IV) and DMSO (5%, IV) pre-treated mice were cut by a Leica RM2265 rotary microtome (Leica Biosystems, Wetzlar, Germany) and stained using haematoxylin and eosin according to the manufacturer´s protokoll (H&E; Sigma Aldrich, Steinheim, Germany). Afterwards tumor histology of two different sections of DMSO- and PT-treated mice was analyzed under 4x magnification using the Olympus CellSens Entry software in combination with an Olympus DP25 camera, connected to an Olympus Bx41 stereomicroscope (Olympus, Munich, Germany). The area of necrotic regions was determined by ImageJ 1.44p software.

2.11.5 B16-F1 mouse melanoma tumor model (multiple doses)

The preparation of the repeated treatment approach was performed as described under 2.11.4, but started once tumors reached a size of about 90 mm^3. PT (10 mg/kg) or DMSO (5% in PBS) was injected IV every third day up to 3 times. Tumor size was determined every day (assessed by π/6 x width x height x length), and daily measurement of mouse weight served as health control.

2.12 Statistical analysis

The number of independently performed experiments (n) is stated in the respective figure legend. If HUVECs were used, a different cell preparation from different donors was performed each time. Bar graph data are expressed as means ± S.E.M. Statistical analysis was performed with Prism software (version 5.04; GraphPad Software, San Diego, CA, USA). For comparison of two groups an unpaired t-test was performed. Three or more groups were compared by one-way analysis of variance (ANOVA) followed by a Newman-Keuls multiple comparison post-test. Statistical significance is assumed if $p \geq 0.05$.

3 RESULTS

3.1 PT induces typical hallmarks of vascular disruption in ECs *in vitro*

Previous work already demonstrated that PT shows an anti-angiogenic potential in proliferating EC *in vitro* as well as *in vivo*[16] and is even able to inhibit cancer cell migration and survival.[15] In the present study we aimed to investigate the potential of PT to induce typical hallmarks of vascular disruption. Since VDAs are described in literature to induce first significant effects within a few hours after treatment,[70-72] we designed our experiments by using short incubation times with PT (1-6 h). We first focused on PT induced EC effects *in vitro* and simulated an intact vasculature by using confluent endothelial monolayers.

3.1.1   PT induces the depolymerization of microtubules

Eirich *et al.*[108] and Rath *et al.*[16] already demonstrated that PT is able to directly target microtubules and to induce their depolymerization in proliferating EC. To investigate if PT is able to destroy microtubules in our system (confluent ECs), we performed immunofluorescence stainings of polymerized microtubules. Untreated HUVECs showed intact, polymerized, filamentous microtubules, whereas PT treatment for 1 h with 10, 30, 100 and 300 nM induced a concentration-dependent microtubule depolymerization (Figure 16 upper panel). Combretastatin A-4-phosphate (CA-4P), the lead VDA, showed depolymerization in a similar extent under the same conditions (Figure 16 lower panel), suggesting that PT is of comparable potency regarding its tubulin-destroying action.
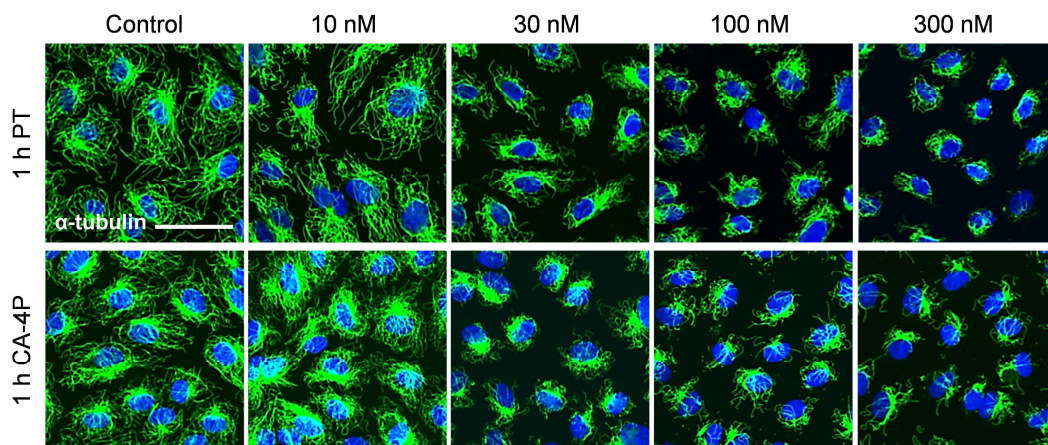

Figure 16   PT leads within 1 h to a concetration-dependent depolymerization of microtubules. Confluent HUVECs were either left untreated (control) or were pre-treated for 1 h with 10, 30, 100, and 300 nM PT or CA-4P. After washing out of tubulin-monomers and -dimers, remaining polymerized microtubules were stained with an anti-α-tubulin antibody (green) and nuclei were visualized by Hoechst 33342 (blue). One representative experiment out of four is shown. Scale bar represents 50 μm.

3.1.2 PT triggers actin stress fiber formation, disrupts EC junctions, and induces reorganization of focal adhesions

Besides alterations of the microtubule cytoskeleton, PT caused morphological changes of HUVECs and induced intracellular gap formation, which is indicative for actin cytoskeleton changes and the disassembly of cell-cell contacts. We treated confluent HUVECs with 30 and 300 nM PT (10 and 100 nM data not shown) and analyzed (*via* immunofluorescence stainings) F-actin, adherens junctions (VE-cadherin), tight junctions (claudin-5) and focal adhesions (vinculin). 1 h incubation with 300 nM PT led to the formation of prominent actin stress fibers across the cell body and induced disruption of adherens and tight junctions, thereby forming huge intracellular openings (Figure 17, arrow heads, lowest panel). In contrast, control cells showed the typical appearance of junctions at the cell margin (Figure 17 upper panel). Focal adhesions were not disassembled but showed a strong redistribution into pronounced clustered structures.
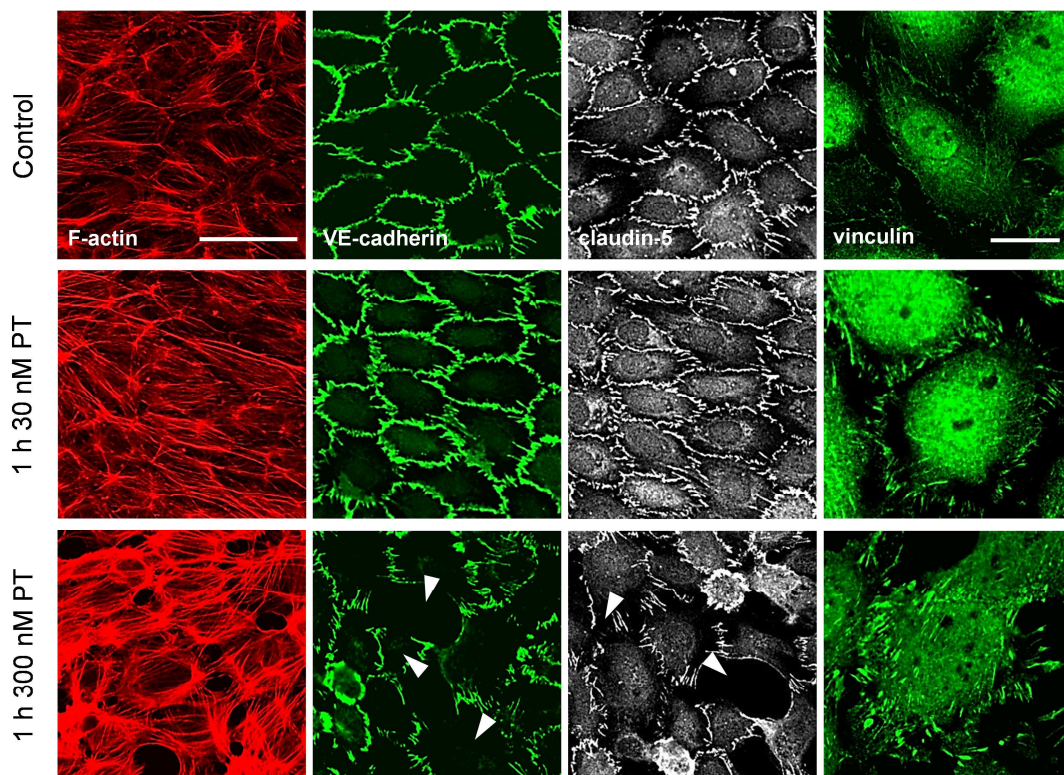

Figure 17   PT treatment induces F-actin formation, disrupts cell-cell connections and reorganizes focal adhesions within 1 h. HUVECs were treated with vehicle control, 30 or 300 nM PT for 1 h and were stained for actin with rhodamine phalloidine (red), for adherens and tight junctions with antibodies against VE-cadherin (left green) and claudin-5 (white), and for focal adhesions using an anti-vinculin antibody (right green). Arrowheads indicate intracellular openings. Images were taken by the confocal laser scanning microscope with a 40x magnification. One representative experiment out of three is shown. Scale bars represent 50 µm (for F-actin, VE-cadherin and claudin-5) and 20 µm (for vinculin).

3.1.3 PT rapidly induces endothelial barrier breakdown

Cellular changes, as described in 3.1.1 and 3.1.2 are in general accompanied by an increase in endothelial permeability.[109] To prove if PT has any influence on this parameter, we performed two different permeability assays. In addition, we quantified the amount of extracellular VE-cadherin since it is known to play an important role in regulating endothelial barrier function.[110]

3.1.3.1 Impedance sensing

First, we measured impedance of confluent HMECs grown on gold-electrodes (Figure 18). We observed a time- and concentration-dependent decrease in electrical impedance (*i.e.* increase in permeability) that reaches the minimum (50%) within 1.5 h upon treatment with 100 nM or (40%) within 1 h upon 300 nM PT (Figure 18 A). Quantification of all tested concentrations at time point 1 h resulted in an IC_{50} value of 71 nM (Figure 18 B).
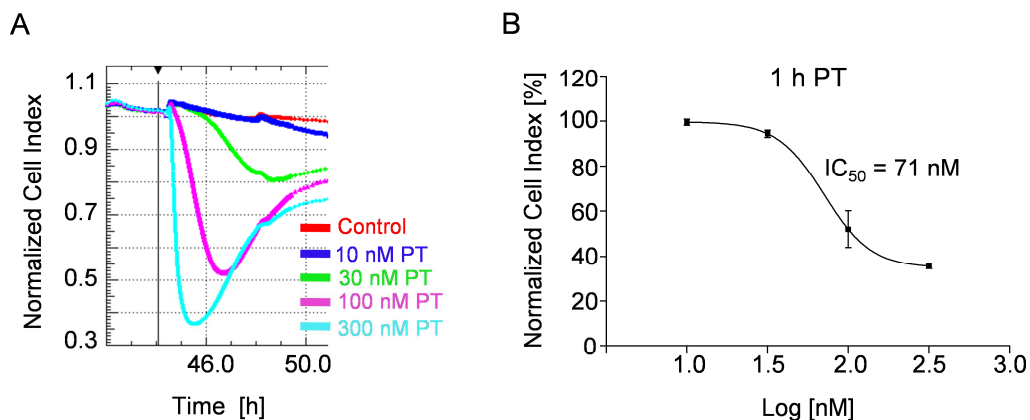

Figure 18   PT decreases electrical impedance. A: HMECs were seeded on gold electrodes, grown to confluence and treated with 10, 30, 100 and 300 nM PT. The vertical black line represents the time point of normalization. Impedance was measured every 10 s up to 12 h. One representative graph out of four is shown. **B:** Quantitative analysis of impedance sensing was performed at time point 1 h after treatment. Data is expressed as normalized cell index, a dimensionless parameter derived from the measured impedance changes (PT mean ± SEM, n = 4).

3.1.3.2 Macromolecular permeability

In a second approach performed with HMECs, we measured PT-induced permeability to macromolecules, by using FITC-labeled dextran (40 kDa) as a tracer. After collecting the supernatant of the lower compartment, we obtained a time- and concentration-dependent increase in transendothelial permeation of dextran (*i.e.* increase in permeability), whereby 100 and 300 nM PT led to a significant increase in permeability within 4 h compared control cells (Figure 19 A,B).
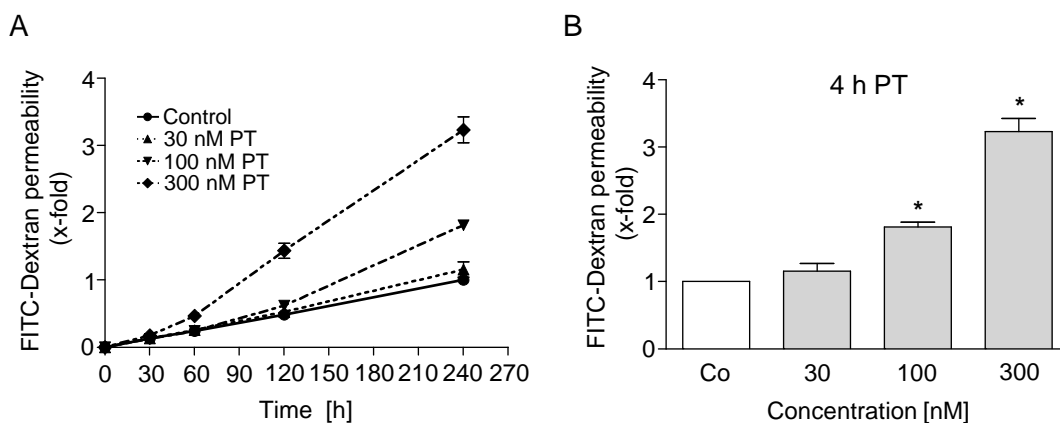

Figure 19   PT treatment increases permeability to macromolecules. A: HMECs were grown to confluence on Transwell™ inserts and were treated with vehicle control (●), 30 nM PT (▲), 100 nM PT (▼) and 300 nM PT (♦). FITC-labeled dextran (40 kDa) was used as a tracer and added to the upper compartment of the chamber. After 30, 60, 120 and 240 min the amount of FITC-dextran in the lower compartment of the chamber was determined. **B:** Quantitative analysis was performed at time point 4 h. Control values were set as 1. *$*P \leq 0.05$ versus control, n = 4.

3.1.3.3 PT reduces extracellular VE-cadherin expression

From literature it is known that especially adherens junctions (composed of vascular endothelial cadherin, VE-cadherin) are one of the major components in regulating the endothelial barrier function[53]. Several signal molecules (*e.g.* Rho, Ca^{2+}, and Src) affect VE-cadherin either by phosphorylation and internalization or by its organization and expression at the cell surface.[110] To assess whether PT treatment influences the expression pattern of VE-cadherin, we determined the extracellular amount of VE-cadherin by FACS analysis. Upon 2 h treatment with 30, 100 and 300 nM PT we observed a concentration-dependent decrease of VE-cadherin of about 80% and 300 nM PT (Figure 20).
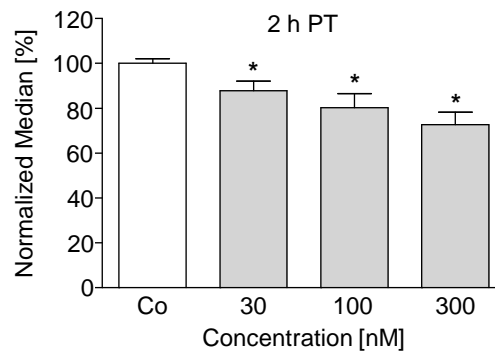
Figure 20   PT mediates hyperpermeability *via* reduced extracellular VE-cadherin expression. Confluent HUVECs were treated for 2 h with 30, 100 and 300 nM PT. After staining with an anti-VE-cadherin-FITC antibody, cells were analyzed by flow cytometry. Quantitative analysis was performed at time point 2 h. Data are expressed as mean ± S.E.M. (n=4). *$P \leq 0.05$ versus control.

Based on this data, we suggest that the PT-mediated hyperpermeability might be a result of a reduced VE-cadherin expression at the cell surface, as well as an increased actinomyosin contraction (indicated by actin stress fibers) that causes cell retraction and disruption of the VE-cadherin complex (see 3.1.2).

3.1.4 PT disrupts established endothelial tubes

Since the main hallmark of microtubule-targeting VDAs is the selective disruption of established tumor blood vessels, we aimed to investigate if PT is able to destroy pre-existing endothelial tubes *in vitro and ex vivo*.

3.1.4.1 PT disrupts endothelial tubes *in vitro*

HUVECs were seeded on Matrigel™ and were allowed to form endothelial tubes for 16 h. Tubes were then treated with vehicle control, 10, 30, 100, or 300 nM PT (10 and 300 nM are not shown). Images were taken before (0 h) as well as after 3 h and 6 h PT treatment (Figure 21 A). We observed a concentration-dependent disruption of PT-treated tubes starting at 1.5 h after PT addition (not shown), leading to almost complete disruption within 6 h and 100 nM PT (indicated by arrowheads). We furthermore evaluated and quantified the total tube length, the total amount of tubes as well as the total branching points. After 6 h, all parameters of PT-treated tubes were significantly reduced compared to control tubes (Figure 21 B-D).
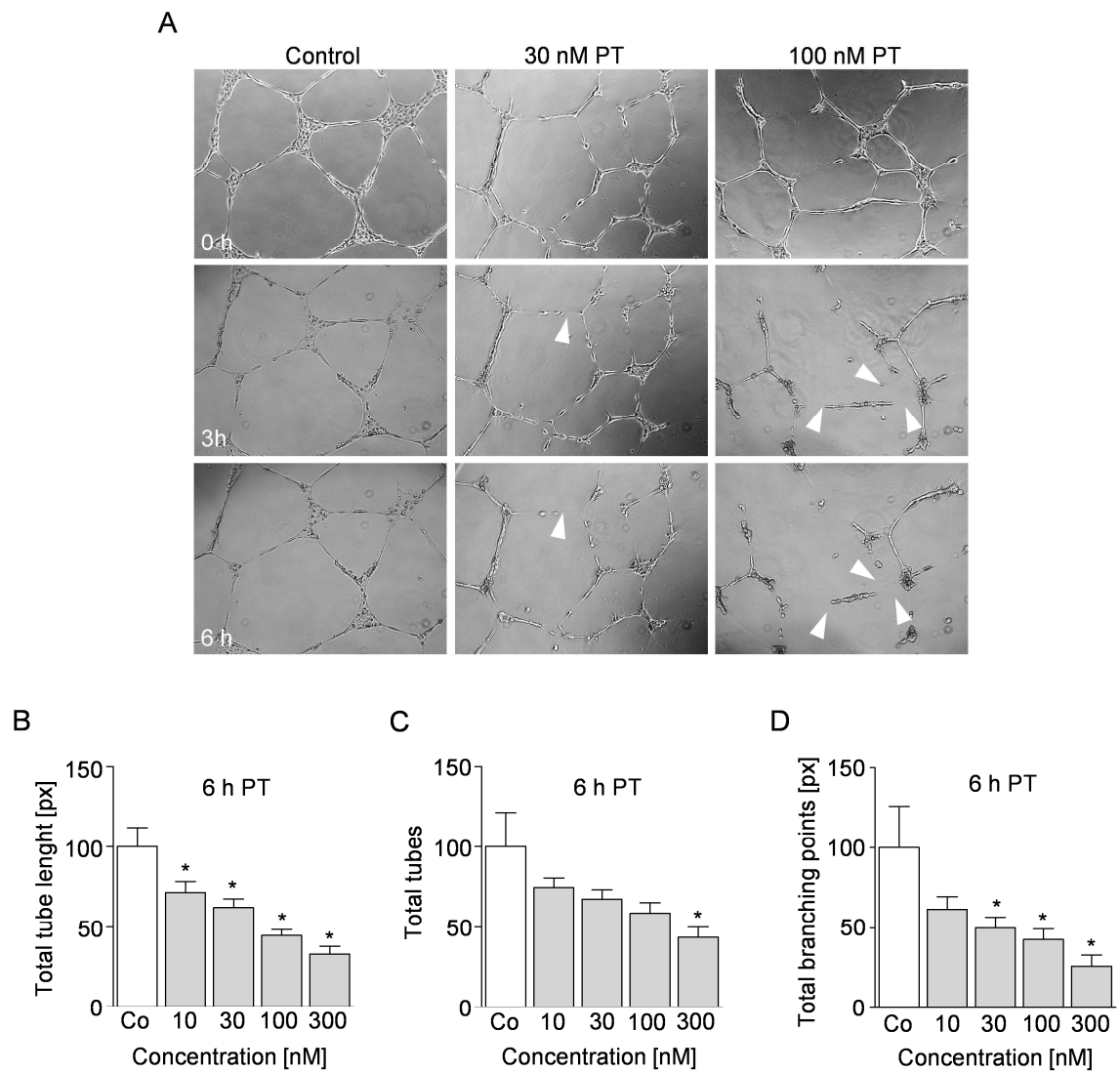
Figure 21   PT disrupts established endothelial tubes *in vitro*. A: HUVECs were seeded on Matrigel™. After 16 h thin endothelial tubes were formed and treated with PT (vehicle control, 30 and 300 nM). Phase contrast images before (0 h) and after 6 h treatment were taken. Original magnification: 10x for all panels. **B-D:** Tube disruption was quantified by the WIMASIS module for tube formation at time point 6 h after PT treatment. Total tube length (B), total number of tubes (C) and total number of branching points (D) were chosen for analysis. Control values were set as 100%. *P ≤ 0.05 versus control, n = 6.

3.1.4.2 PT disrupts endothelial sprouts *ex vivo*

To confirm our observations and to provide a better relation to the *in vivo* situation, we additionally performed an *ex vivo* aortic ring assay. Aortic rings prepared from mouse aortae were embedded into Matrigel™. Once endothelial sprouts occurred (after 10 d) we treated them with 300 nM PT and took images after 3 h and 6 h (Figure 22 A). In accordance to the *in vitro* approach, *ex vivo* grown aortic sprouts were disrupted within 6 h after PT treatment (Figure 22 A indicated by the arrowheads). Quantification of the total sprout area confirmed our observations and resulted in a significant disruption already after 3 h (Figure 22 B).
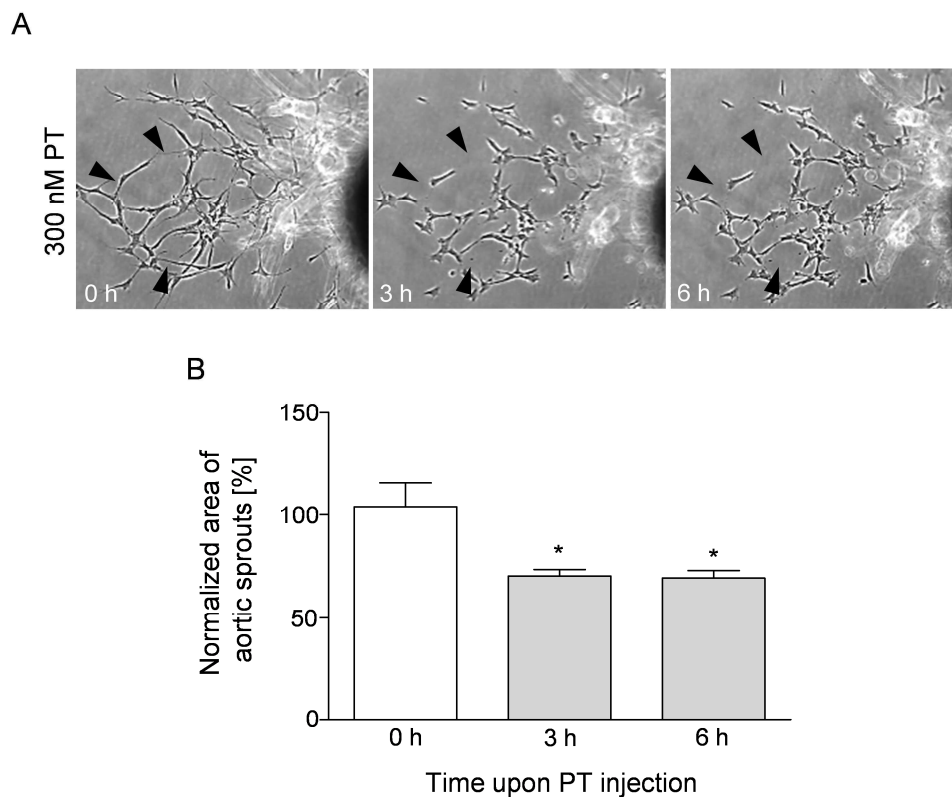

Figure 22   PT disrupts established endothelial sprouts *ex vivo*. A: Aortic rings were prepared and placed into Matrigel™. Once endothelial sprouts were established, they were treated with 300 nM PT. Phase contrast images before (0 h) as well as after 3 h and after 6 h treatment were taken. Arrowheads indicate disrupted sprouts. One representative experiment out of fourteen is shown. Original magnification: 10x (for all panels). **B:** Quantification was performed using ImageJ 1.45s software. Normalized data (0 h) are expressed as mean ± S.E.M. *$P \leq 0.05$ versus control (n = 14).

This result demonstrates that PT is able to disrupt established endothelial tubes *in vitro* and *ex vivo*.

3.1.5 PT treatment is not cytotoxic for ECs

3.1.5.1 Metabolic activity

To prove that the observed cellular changes, induced by PT, are not of cytotoxic nature, we measured metabolic activity using the CellTiter-Blue® reagens resazurin. HUVECs were either simultaneously treated with 10, 30, 100 and 300 nM PT plus resazurin (Figure 23 A) or were pre-treated for 22 h with PT, followed by addition of resazurin for 4 h (Figure 23 B). Metabolic activity was determined by fluorescence measurement of the resazurin metabolite resorufin. PT treatment for 4 h resulted in only a marginal decrease in metabolic activity. Even after 26 h of treatment, only a minimal decrease of about 20% was observed.
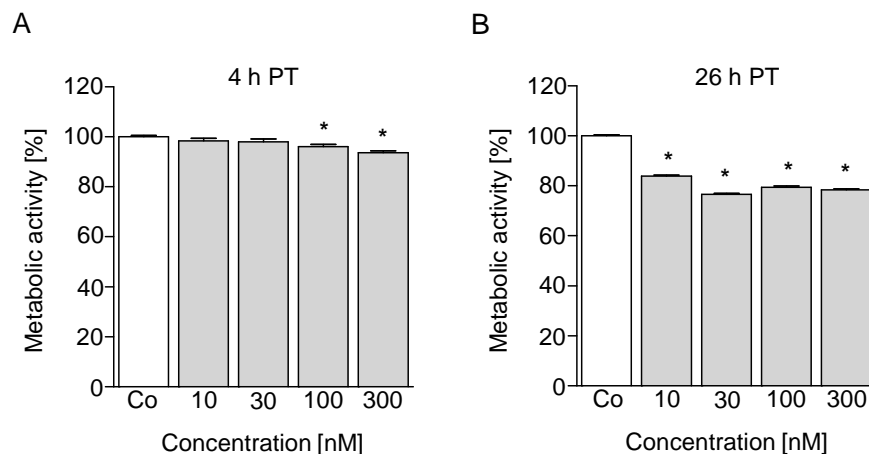

Figure 23   Short-term treatment with PT did not change metabolic activity and only marginally decresaes it upon 26 h PT treatment. A, B: Metabolic activity was measured by the CellTiter-Blue® assay. Confluent HUVECs were either simultaneously treated with 10, 30, 100 and 300 nM PT plus resazurin for 4 h (A) or were pre-treated for 22 h with PT, followed by addition of resazurin for 4 h (B). Metabolic activity was determined by fluorescence measurement of the resazurin metabolite resorufin. Control values were set as 100%. *$P \leq 0.05$ versus control, n=4 (A), n=6 (B).

3.1.5.2 Quantification of apoptotic and necrotic cells

By FACS analysis we determined the number of apoptotic cells *via* counting the amount of subdiploid DNA content (Figure 24 A) and necrotic cells *via* propidium iodide staining (Figure 24 B). In addition, we also measured the cell cycle (Figure 24 C). After treatment with 10, 30, 100 and 300 nM PT for 24 h we observed, compared to control cells, a concentration-dependent increase of about 10% in apoptotic cells (Figure 24 A) and an increase of about 15% in dead cells (Figure 24 B). We could not detect any G2/M arrest

(Figure 24 C), which plays an important role in the onset of apoptosis-mediated cell death. To assess the amount of induced cell death, we used 0.01% Triton (T) as positive control. An increase of about 60% compared to control cells (Figure 24 B) was detected. This result indicates that PT only marginally induces apoptosis and necrosis, which is far away from typical substances that trigger cell death.
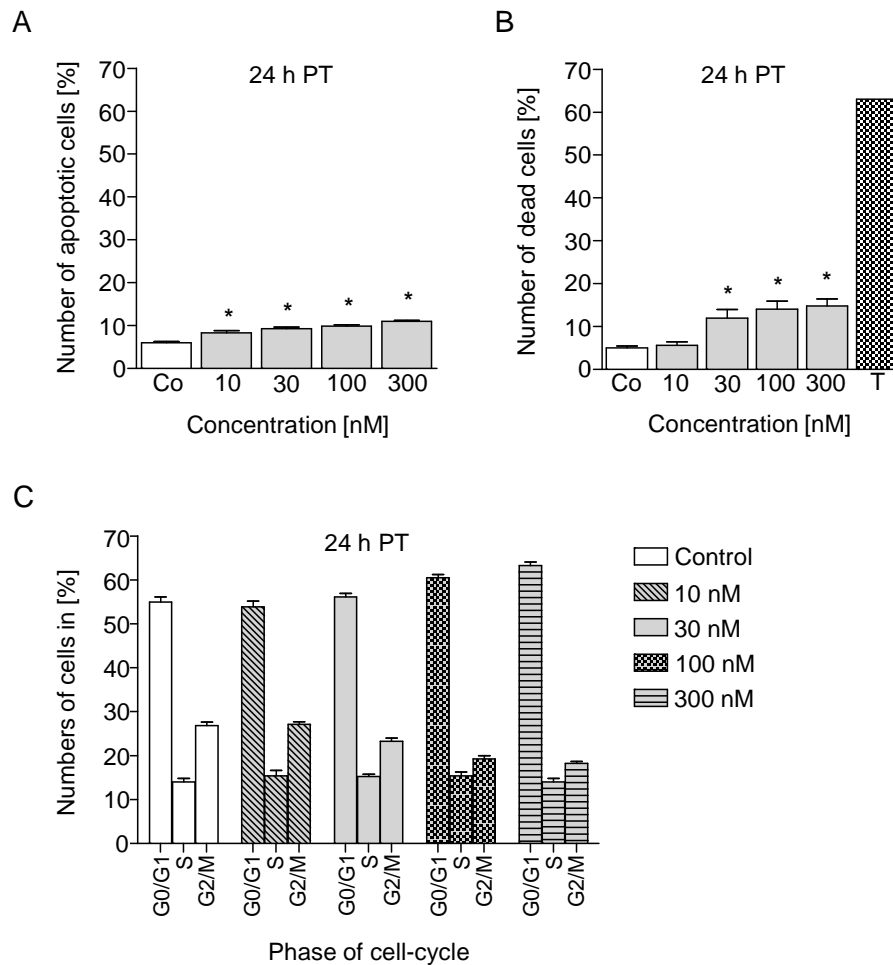

Figure 24 **PT only marginally induced cytotoxicity after 24 h. A-C:** The number of apoptotic (A), and necrotic (B) cells as well as cell-cycle phases (C) were determined using confluent HUVECs, which were either pre-treated with vehicle control or with 10, 30, 100 and 300 nM PT for 24 h. After permeabilization (A and C), cells were stained with propidium iodide (PI) and analyzed by flow cytometry. 0.01% Triton (T) served as positive control (only B). Quantification was performed at time point 24 h. *$P \leq 0.05$ versus control, n=3 (A-C).

3.1.5.3 Recovery after withdrawal of PT

To confirm our data (3.1.5.1 and 3.1.5.2) and to demonstrate that the applied PT concentration is not toxic to endothelial cells, we treated an intact confluent HUVEC monolayer with 10, 30, 100 and 300 nM PT (10 and 100 nM data not shown) and took pictures after 1 h and 24 h (Figure 25 A,B upper panel). Incubation with 30 nM for 1 h resulted in no obvious cellular changes, however, after 24 h treatment cell retraction was visible (Figure 25 A). In contrast, already after 1 h incubation with 300 nM PT (Figure 25 B) we observed that cells retract and intracellular openings occur, which were still evident after 24 h. Removal of PT and addition of fresh medium for 24 h resulted in a complete restoration of the HUVEC monolayer, and no difference between 1 h or 24 h PT-treated cells was visible. A few dead cells could be observed, indicating that a small number of cells underwent apoptosis or necrosis.
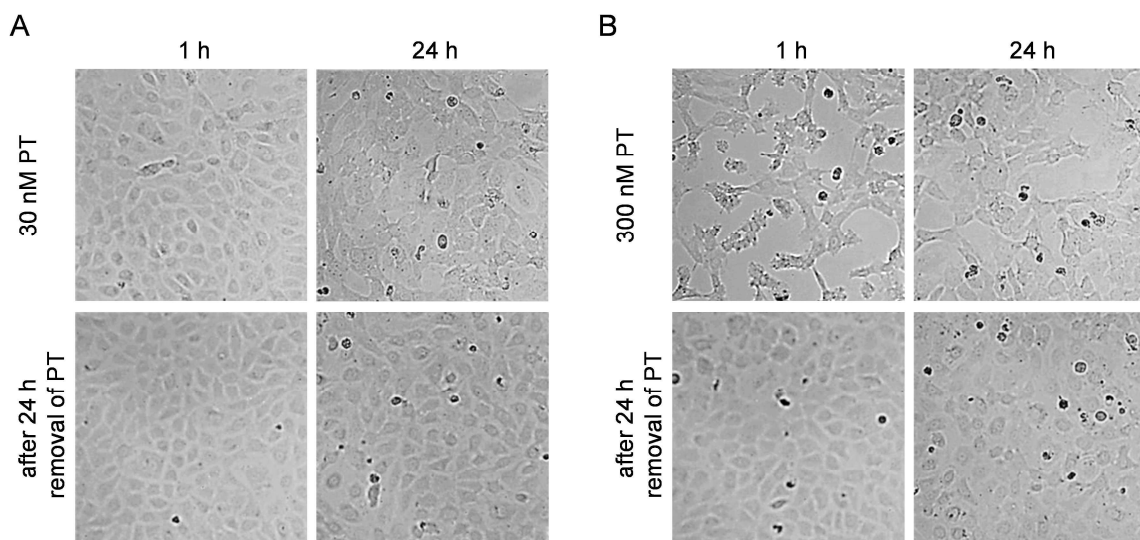
Figure 25   PT-induced cellular effects are reversible. A,B: Confluent HUVECs were treated with 30 nM PT (A) or 300 nM PT (B) for 1 h or 24 h (upper row). After removal of PT, cells were washed twice and fresh growth medium (ECGM) was added. After 24 h incubation without PT (lower panel) the same well was photographed using brightfield microscopy. One representative experiment out of three is shown. Original magnification: 10x (for all panels).

In summary, we could show that PT exhibits typical features of a vascular disrupting agent in ECs *in vitro*.

1. PT binds to microtubules and induces their depolymerization
2. PT leads to an enormous actin stress fiber formation and EC junction disruption
3. PT strongly increases endothelial permeability
4. PT destroys established endothelial tubes

PT did neither considerably influence the metabolic activity of HUVECs, nor induce short time apoptosis and cell death. After withdrawal of PT, HUVECs were able to fully rebuild their normal morphology, indicating that PT treatment is not cytotoxic.

3.2 PT-induced signaling cascades leading to actin stress fiber formation and hyperpermeability

Since PT treatment provokes prominent alterations of the actin cytoskeleton, leading to weak cell-cell connections and to endothelial hyperpermeability, we next focused on the possible underlying signaling cascades. In literature there are several pathways described that impair endothelial barrier function, however, in the context of vascular disruption, only two, the RhoA/ROCK/MLC and the p38 MAPK pathways have been described so far to play important roles.[80, 111] We therefore proved whether these pathways are also involved in our system. Additionally, we investigated the influence of intracellular calcium $[Ca^{2+}]_i$ since it is well known that $[Ca^{2+}]_i$ is an important upstream regulator of PKC, Src, Rho and MLCK, which in turn promote actinomyosin contraction, junction disruption and endothelial hyperpermeability.[112]

3.2.1 Involvement of the RhoA/ROCK/MLC pathway

3.2.1.1 RhoA

We performed an active RhoA pull down assay and collected GTP-bound RhoA after 15, 30, and 60 minutes of 300 nM PT pre-treatment. The amount of active RhoA was analyzed by Western blotting (Figure 26 A). We observed an induction of active RhoA within 30 min, which significantly increased by about 100% after 1 h PT treatment (Figure 26 B). The supernatant, which contains inactive GDP-bound RhoA, served as control.
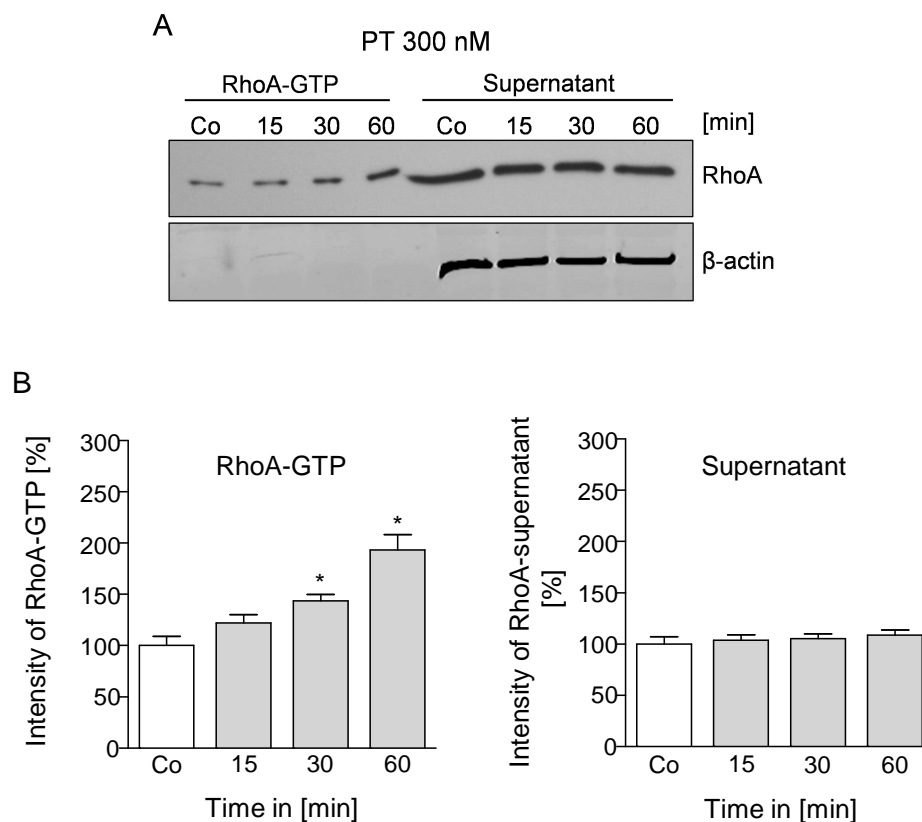
Figure 26   **PT treatment activates RhoA GTPase within 30 min. A:** Confluent HUVECs were either pre-treated with vehicle control (Co) or with 300 nM PT for 15, 30 and 60 min. Active RhoA isolation was performed as described in the materials and methods section. One representative experiment out of four is shown. **B:** Quantitative evaluation was performed by ImageJ 1.45s. Data are expressed as mean ± S.E.M. *$P \leq 0.05$ vs. control (n = 4).

3.2.1.2 MLC2

To investigate whether known downstream targets of RhoA were activated, we first focused on myosin light chain (MLC). Due to the fact that active RhoA was detectable within 1 h treatment, we used this time point for immunocytochemistry experiments. HUVECs were pre-treated with 300 nM PT and stained for F-actin with rhodamine phalloidine and for MLC with an anti-diphospho MLC(Thr18/Ser19) antibody (Figure 27 A). Control cells showed F-actin in peripheral bands along the cell margin and a weak, basal activation of MLC(Thr18/Ser19). In contrast, PT-treated HUVECs exhibited stress fiber formation and MLC(Thr18/Ser19) activation, which could additionally be confirmed by Western blot analysis, by which we observed a clear induction of MLC(Ser19) and MLC(Thr18/Ser19) within 30 minutes of PT treatment (Figure 27 B).
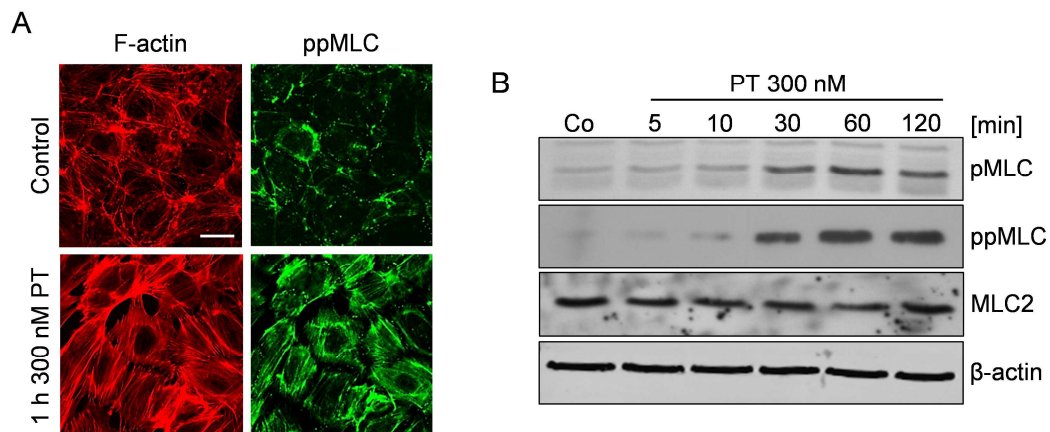

Figure 27   PT treatment activates MLC(Ser19) and MLC(Thr18/Ser19) within 30 min. A: Immunocytochemistry and confocal microscopy of di-(Thr18/Ser19) phosphorylated MLC2 upon treatment with 300 nM PT for 1 h. One representative experiment out of three is shown. Scale bar represents 50 µm. **B:** Activation of mono(Ser19)- and di(Thr18/ser19)-phosphorylated MLC2 was analyzed by Western blotting. Confluent HUVECs were either pre-treated with vehicle control (Co) for 120 min or 5, 15, 30, 60 and 120 min with 300 nM. One representative blot out of four is shown.

3.2.1.3 MLCP and MLCK

The observed increase in MLC phosphorylation could be mediated through inactivation of myosin light chain phosphatase (MLCP) by phosphorylation of the catalytic domain, called MYPT1, or by activation of the myosin light chain kinase (MLCK). By Western blot analysis we could show that PT treatment did neither change the phosphorylation status of MYPT1 (Figure 28 A) nor alter MLC phosphorylation when combined with the MLCK inhibitor ML-7 (Figure 28 B). This indicates that neither MLCP nor MLCK are involved in PT-induced signaling.
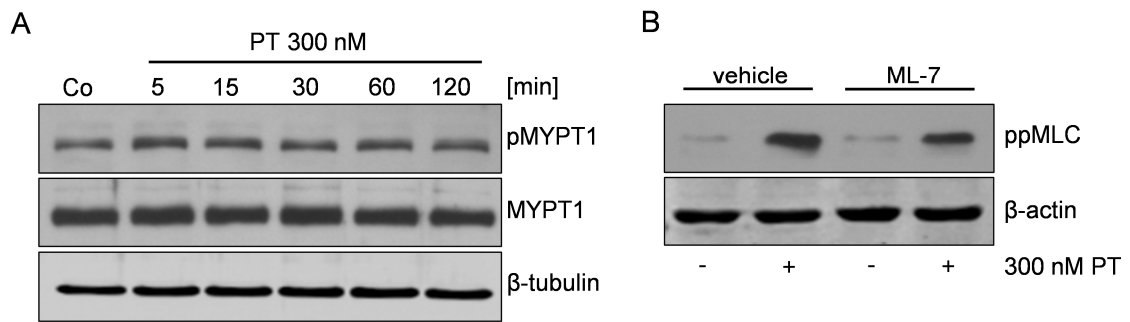
A

PT 300 nM

Co   5   15   30   60   120   [min]

pMYPT1

MYPT1

β-tubulin

B

vehicle   ML-7

ppMLC

β-actin

-      +   -   +   300 nM PT

Figure 28   MLCP and MLCK are not involved in PT-induced MLC2 activation. A,B: Involvement of MLCP (A) and MLCK (B) in terms of MLC2 activation was analyzed by Western blotting. **A:** Confluent HUVECs were either pre-treated with vehicle control (Co) for 120 min or for 5, 15, 30, 60 and 120 min with 300 nM PT. Afterwards MLCP activation was analyzed using an specific anti-MYPT1 antibody. **B:** Confluent HUVECs were pre-treated with the MLCK inhibitor ML-7 (10 µM, 30 min) followed by PT treatment (300 nM, 1 h). MLCK involvement was determined using an di(Thr18/ser19)-phosphorylated MLC2 antibody (downstream target of MLCK). One representative blot out of three is shown, each.

3.2.1.4 ROCK

A second possibility to induce MLC activation is *via* the Rho kinase (ROCK), which phosphorylates MLC at Ser19 and, therefore, leads to a direct MLC activation. To determine whether the actin response or the MLC activation were mediated by ROCK, we pre-treated HUVECs with the ROCK inhibitor Y-27632 (Figure 29). PT-induced stress fiber formation was clearly reduced by this inhibitor and also MLC(Thr18/Ser19) activation was completely prevented.

Control   Y27632   300 nM PT   Y+300 nM PT

F-actin

ppMLC
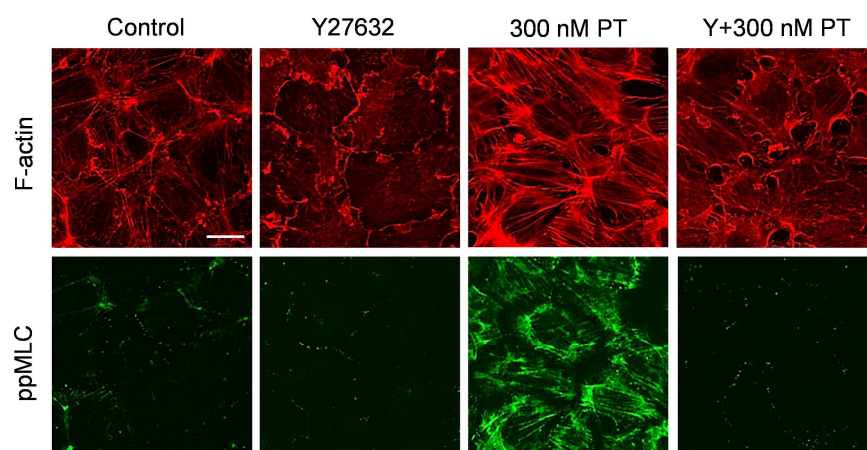
Figure 29   PT-induced actin stress fiber formation and MLC activation depends on ROCK. Immunocytochemistry and confocal microscopy of F-actin (rhodamine phalloidine) and di-(Thr18/Ser19) phosphorylated MLC2 after treatment with vehicle control (1 h), with the ROCK inhibitor Y27632 (10 µM, 1 h), with 300 nM PT (1 h) or in combination with Y27632 (10 µM, 30 min pre-treatment) plus PT (300 nM, 1 h). One representative experiment out of three is shown. Scale bar represents 50 µM**.**

To prove if the PT-mediated hyperpermeability was also reduced, we measured impedance *via* the xCELLigence System (*i.e.* permeability, see 2.6.1). We treated HUVECs either with the ROCK inhibitor for 30 min, or with 300 nM PT, or in combination (30 min Y27632 followed by PT treatment). Indeed, quantification at time point 1.5 h upon PT treatment revealed that pre-treatment with the ROCK inhibitor partially reversed the PT-induced decrease in impedance.
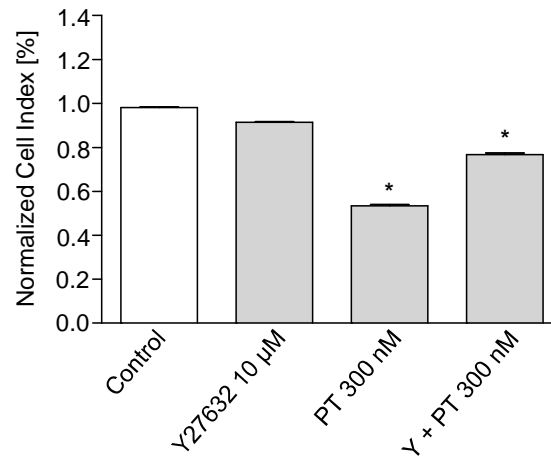

Figure 30   PT triggers hyperpermeability *via* ROCK. HUVECs were seeded on gold electrodes, grown to confluence and treated either with Y27632 (10 µM), with 300 nM PT or in combination (30 min Y27632 followed by PT). Quantitative analysis of impedance sensing was performed at time point 1.5 h after PT treatment. Data is expressed as normalized cell index, a dimensionless parameter derived from the measured impedance changes. PT mean ± S.E.M. *$P \leq 0.05$ vs. control (n = 1).

Thus, we could show that ROCK plays a central role in the PT-induced signaling pathway. Furthermore, we observed RhoA activation and subsequent MLC phosphorylation within 1 h PT treatment, which perfectly correlates with microtubule depolymerization described in chapter (3.1.1.). Therefore, we assume that a link between microtubule depolymerization and RhoA-ROCK-MLC pathway activation exist.

3.2.2 Involvement of MAPK pathways

Besides the Rho pathway, mitogen-activated protein kinases (MAPKs) (p38, c-Jun N-terminal kinases (JNK) and extracellular regulated kinase (ERK1/2)), are known to be involved in stress fiber formation and hyperpermeability[113]. By Western blot, we could show that JNK (Figure 31 B) and p38 MAPK, as well as its downstream target heat shock protein 27 (HSP27; Figure 31 A) were phosphorylated (*i.e.* activated) within 30 min upon PT treatment, whereas ERK1/2 was not affected (Figure 31 C).
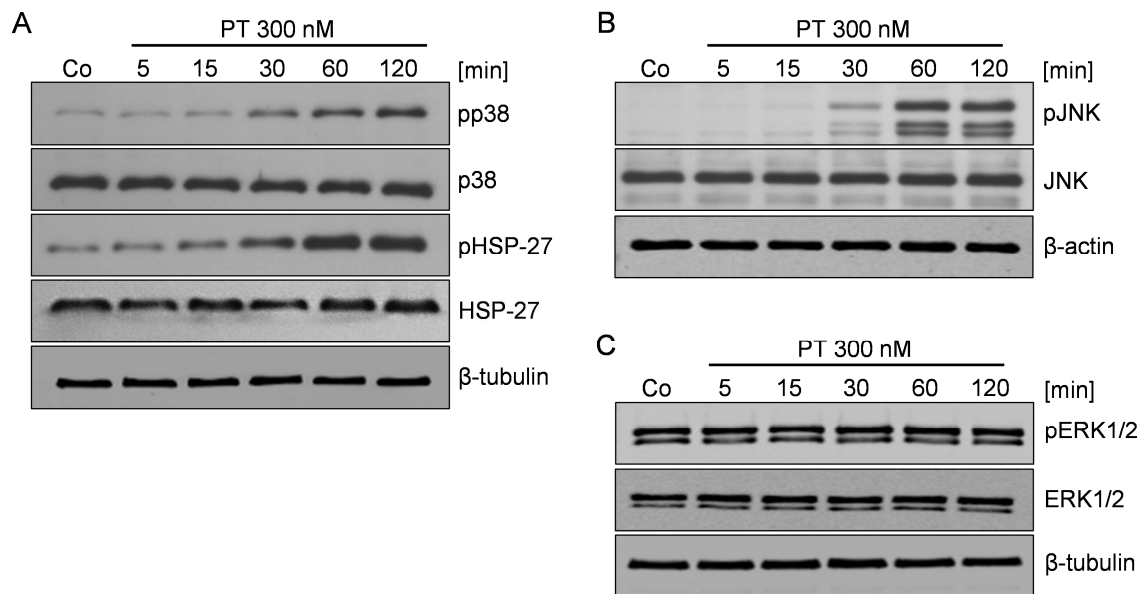

Figure 31   PT activates JNK and p38 MAPK but not ERK1/2. A-C: Confluent HUVECs were either pre-treated with vehicle control (Co) or with 300 nM PT for 5, 15, 30, 60 and 120 min. Activation of p38 MAPK, HSP27, JNK and ERK1/2 were analyzed by Western blotting using specific antibodies. One representative experiment out of three is shown each.

3.2.3 p38 MAPK and JNK

In the next step we focused on p38 MAPK and JNK. Both are described to be activated upon microtubule depolymerization,[114-117] however, only p38 MAPK is known so far to be involved in microtubule-associated actin remodelling and hyperpermeability in endothelial cells.[114, 115] To investigate the role and importance of both MAPKs in terms of actin alterations upon PT treatment, we used specific inhibitors for p38 MAPK (SB203580, Figure 32 A) and JNK (SP600125, Figure 32 B). Interestingly, although we prove

functionality of the inhibitors (data not shown), they could not prevent the PT-induced actin stress fiber formation, cell retraction and gap formation.
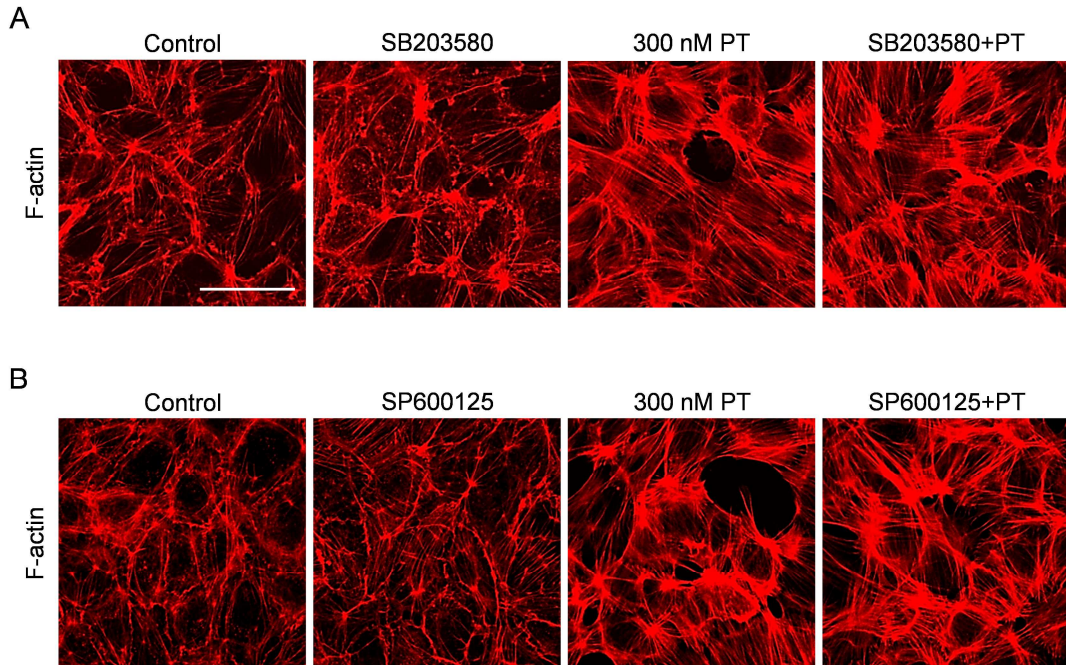

Figure 32   MAPK inhibitors SB203580 and SP600125 could not prevent stress fiber formation upon PT treatment. A,B: Immunocytochemistry and confocal microscopy of F-actin (rhodamine phalloidine) after treatment with vehicle control (1 h), with the p38 MAPK inhibitor SB203580 (20 μM, 1 h, A), with the JNK inhibitor SP600125 (25 μM, 1 h, B), with 300 nM PT (1 h) or in combination. One representative experiment out of three is shown. Scale bar represents 50 μM.

To elucidate the effects on endothelial permeability, we measured impedance as described above (3.1.3.1). We pre-treated confluent HUVECs for 30 min with the p38 MAPK inhibitor SB203580. Followed by a treatment with 100 and 300 nM PT. As expected, similar to the control (red line), single treatment with the inhibitor (pink line) did not influence the permeability and combination treatment with the inhibitor plus PT did not prevent the observed decrease in impedance (*i.e.* increase in permeability; cyan *vs.* green line and purple *vs.* blue line). However, compared to single PT treatment, the onset of hyperpermeability was shifted to later time points.
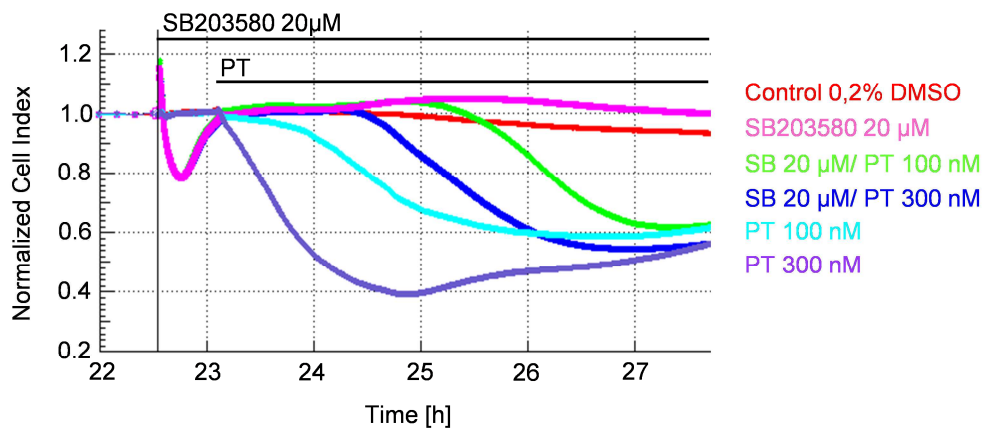
Figure 33   p38 MAPK is not involved in PT-mediated hyperpermeability. HUVECs were seeded on gold electrodes, grown to confluence and treated either with SB203580 (20 µM), with 100 and 300 nM PT or in combination (30 min SB203580 followed by PT). Data is expressed as normalized cell index, a dimensionless parameter derived from the measured impedance changes (PT mean ± SEM, n = 3).

3.2.4 Involvement of intracellular calcium [Ca^{2+}]$_i$

Since a rise in cytosolic Ca^{2+} has been established as the initial and pivotal signal that precedes endothelial contraction, junction disruption and hyperpermeability, we tested whether cytosolic calcium levels were affected by PT treatment. Therefore, HUVECs were pre-treated with Fura-2-AM (30 minutes 2 µM). Afterwards, 300 nM PT was added and [Ca^{2+}]$_i$ levels were recorded for 45 minutes (Figure 34). To obtain a positive calcium signal and to confirm that cells are still alive, 10 µM histamine was added at time point 45 minutes and data were recorded for further 10 minutes. We could not detect any changes in cytosolic calcium levels upon PT treatment, suggesting that calcium does not play a role in PT-triggered signaling.
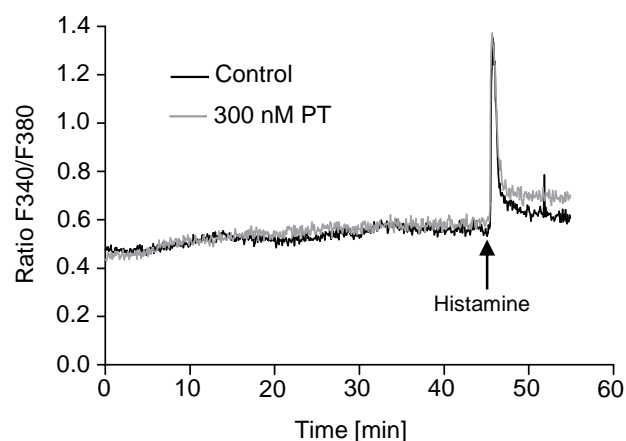
Figure 34 **PT does not affect intracellular calcium levels.** The change of intracellular Ca2+ $[Ca2+]_i$ was monitored using confluent HUVECs which were pre-incubated with FURA-2-AM for 30 min. After replacing FURA-2-AM by HEPES cells were treated for 45 min with 300 nM PT (grey line) or were left untreated (black line). At the end, histamine (100 µM) was added as positiv control and were recorded for further 10 min. One representative figure out of three is shown.

In summary, we suggest that the cellular effects (*i.e.* actinomyosin contraction, junction disassembly and hyperpermeability) of PT are mainly mediated by the RhoA/ROCK/MLC2 pathway, whereby ROCK plays a pivotal role. In contrast, MLCK, MLCP, p38 MAPK, JNK or calcium seem to be not involved. The proposed signal pathway induced by PT is shown below (Figure 35).
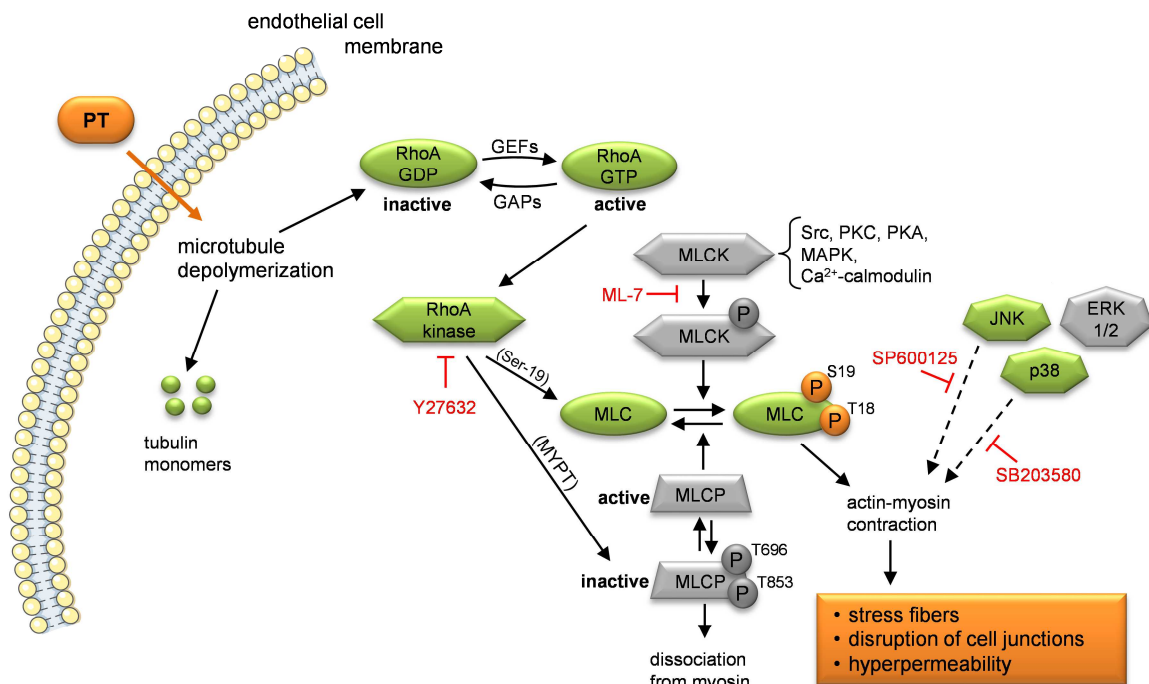
Figure 35 **Proposed signal pathway leading to cellular effects upon PT treatment.** Microtubule dissasembly activates RhoA, which in turn activates ROCK. Direct phosphorylation of MLC *via* ROCK triggers actomyosin-mediated contraction, junction disruption and hyperpermeability. JNK and p38 MAPK are also activated, however they are not essential for the PT induced cellular effects. Green: affected by PT, grey: not affected by PT. Dotted arrow line indicates no direct interaction.

3.3 Single dose treatment with PT selectively affects tumor vasculature *in vivo*

The selective and fast shut down of blood flow in established tumor vessels is the main and most important hallmark of VDAs.[70, 72] Therefore, we aimed to elucidate if PT is able to reduce tumor blood flow *in vivo*. We analyzed vessel quantity and perfusion as well as tumor histology upon single dose treatment with PT by using two different animal models.

3.3.1 Determining the maximum tolerated dose (MTD) of PT

Before we started with the *in vivo* tumor models we determined the MTD of PT. We systematically tested four different dosages of PT (1, 10, 30 and 50 mg/kg; Figure 36) that were IV injected into the tail vein of female C57BL/6 mice. We measured the mouse weight (indicator of health) every day up to 8 days. 1 and 10 mg/kg PT were well tolerated and there was no difference compared to control mice. In contrast, mice treated with 30 and 50 mg/kg PT showed loss of weight and were apathetic. Therefore, a concentration between 10 and 30 mg/kg is suggested as the MTD of PT.
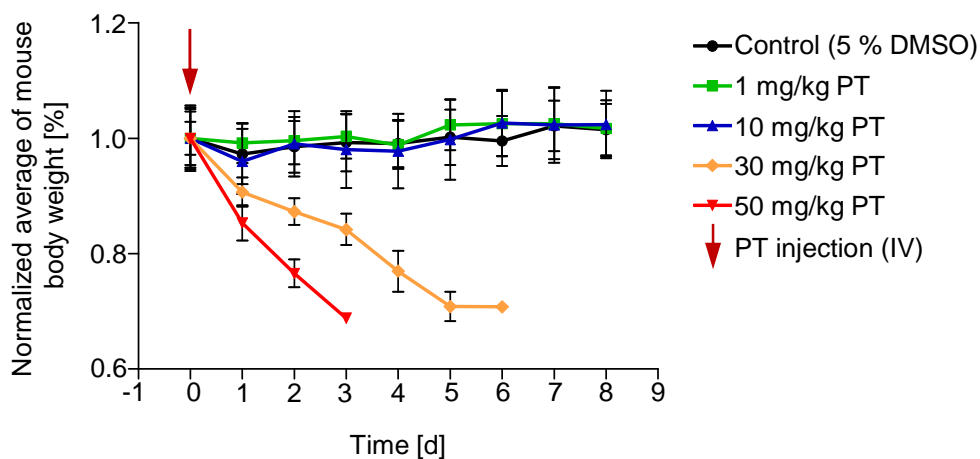
Figure 36 *In vivo* **evaluation of the MTD of PT.** Female C57BL/6 mice were treated with different concentrations of PT (1, 10, 30, and 50 mg/kg; IV into the tail vein). To monitor the state of health, mouse weight was measured every day up to 8 days after PT injection. 1 and 10 mg/kg PT was well tolerated, whereas 30 and 50 mg/kg was not tolerated and the experiment had to be stopped early. Data are expressed as mean ± S.E.M (n = 4, 1 mg/kg) and (n = 5, control, 10, 30 and 50 mg/kg). For clarity, the mouse weight of control mice was normalized to 1.

3.3.2 PT selectively diminished tumor blood flow in a hamster dorsal skinfold chamber model

We elucidated the capability of single dose treatment with PT to reduce tumor blood flow in a hamster dorsal skinfold chamber model, bearing hamster A-Mel-3 amelanotic melanomas (for details see 2.11.3). We simultaneously analyzed tumor blood vessels within the melanoma, and 'normal' blood vessels of the surrounding healthy tissue. FITC-labeled dextran was injected IV to visualize blood perfusion and to determine the baseline. Upon IV injection of 10 mg/kg PT, we observed first perfusion irregularities in tumor blood vessels after 30 minutes (data not shown), which were clearly detectable after 2 h (Figure 37 A, arrowheads, lower panel). In contrast, blood perfusion of 'normal' vessels was not affected (Figure 37 A, upper panel). Additionally, we quantified the velocity of red blood cells, the diameter of the vessels, and the functional vessel density. All three parameters were significantly reduced in tumor blood vessels compared to non-tumor blood vessels (Figure 37 B). Treatment with vehicle control (5% DMSO) did not reduce these parameters, neither in tumor nor in 'normal' blood vessels (Figure 37 C).
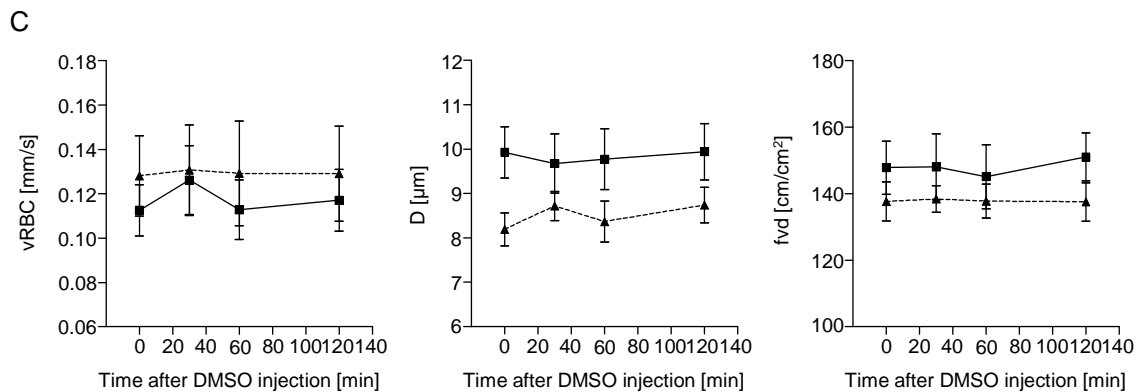
C
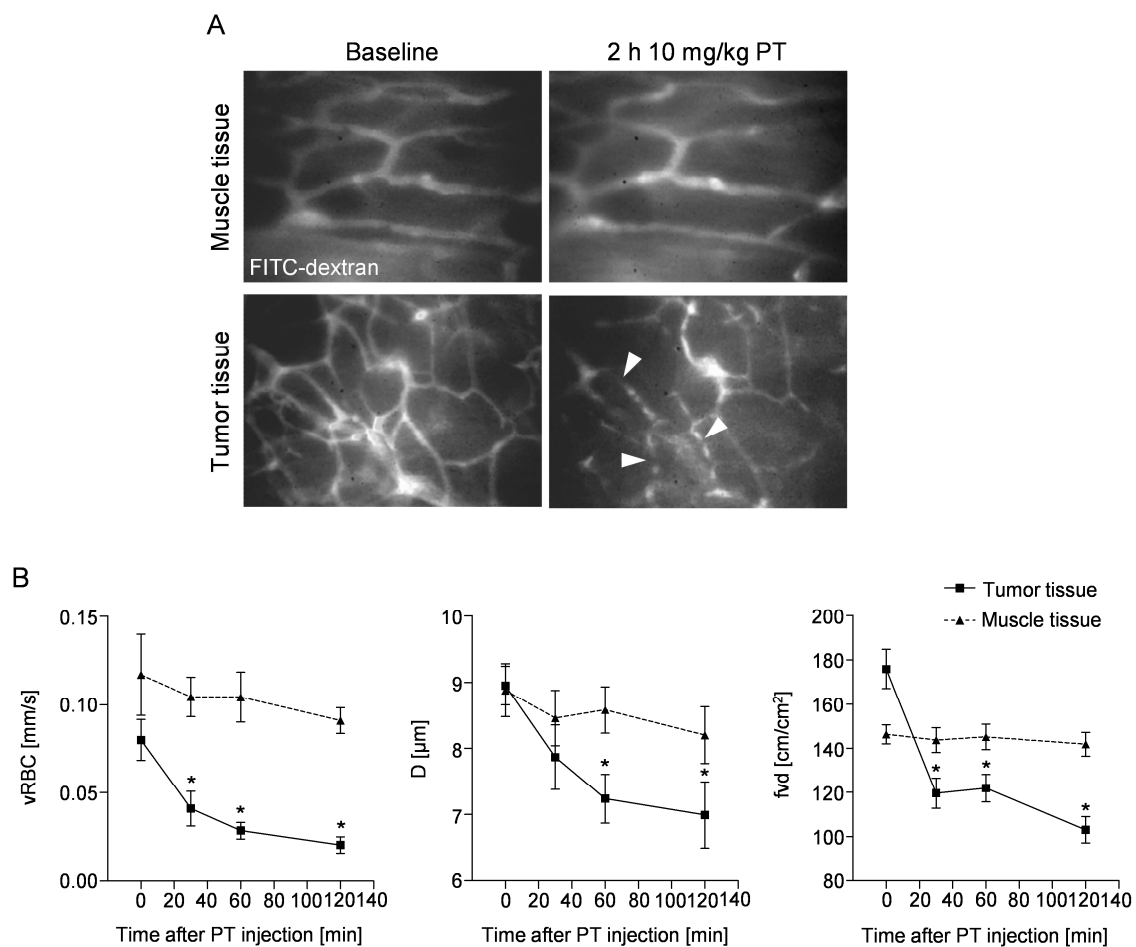
Figure 37 **Single dose of PT selectively reduces tumor blood flow, tumor vessel diameter and functional tumor vessel density. A:** Hamster A-Mel-3 amelanotic melanoma tumors were grown 2-D in hamster dorsal skinfold chambers. FITC-dextran (MW 500 kDa) was pre-injected IV 5 min before PT injection (10 mg/kg) to visualize tumor and healthy microcirculation and to determine the baseline. Every 30 min up to 2 h, 30 s were recorded on digital video tape. Upon 2 h PT injection, normal tissue appears to be not affected, whereas tumor tissue showed regions of lesser perfusion, indicated by the arrowheads. One representative image of intravital microcopy is shown. **B, C:** Five regions of interest per tumor and normal tissue were selected upon PT (B) and DMSO (C) treatment to perform quantitative analysis of microcirculation parameters over a time period of 2 h. Red blood cell velocity (vRBC) [mm/s], vessel diameter (D) [µm] and functional vessel density (fvd) [cm/cm^2] were evaluated offline by an image analysis system. *P, $\leq$ 0.05 versus muscle tissue (PT n = 6, DMSO n = 3).

3.3.3 PT reduces tumor vessel perfusion without affecting the density of tumor vessels in an ectopic B16-F1 mouse melanoma tumor model

To determine whether single dose treatment with PT causes tumor cell death due to tumor blood-flow shutdown we used highly vascularized B16-F1 mouse melanoma tumors (for details see 2.11.4), which grew subcutaneously in the hind limb of C57BL/6 mice. When tumors reached a size of approx. 650 mm^3, we injected IV 10 mg/kg PT or 5% DMSO (vehicle control). 24 h later Hoechst 33342 was IV injected as perfusion marker, and mice were sacrificed after 1 min. Both, the tumor rim as well as the tumor center of PT- or vehicle-treated mice were analyzed (Figure 38). In control tumors, Hoechst 33342 fluorescence (*i.e.* perfusion) was detectable nearly in equal intensity at the rim as well as in the center, whereas PT-treated tumors showed a lesser Hoechst 33342 intensity at the rim and almost no staining in the center (Figure 38 A,B). In contrast, CD31 positive endothelial cells were similarly distributed throughout the tumors, indicating that tumor vessel density was not altered by PT (Figure 38 A,C).
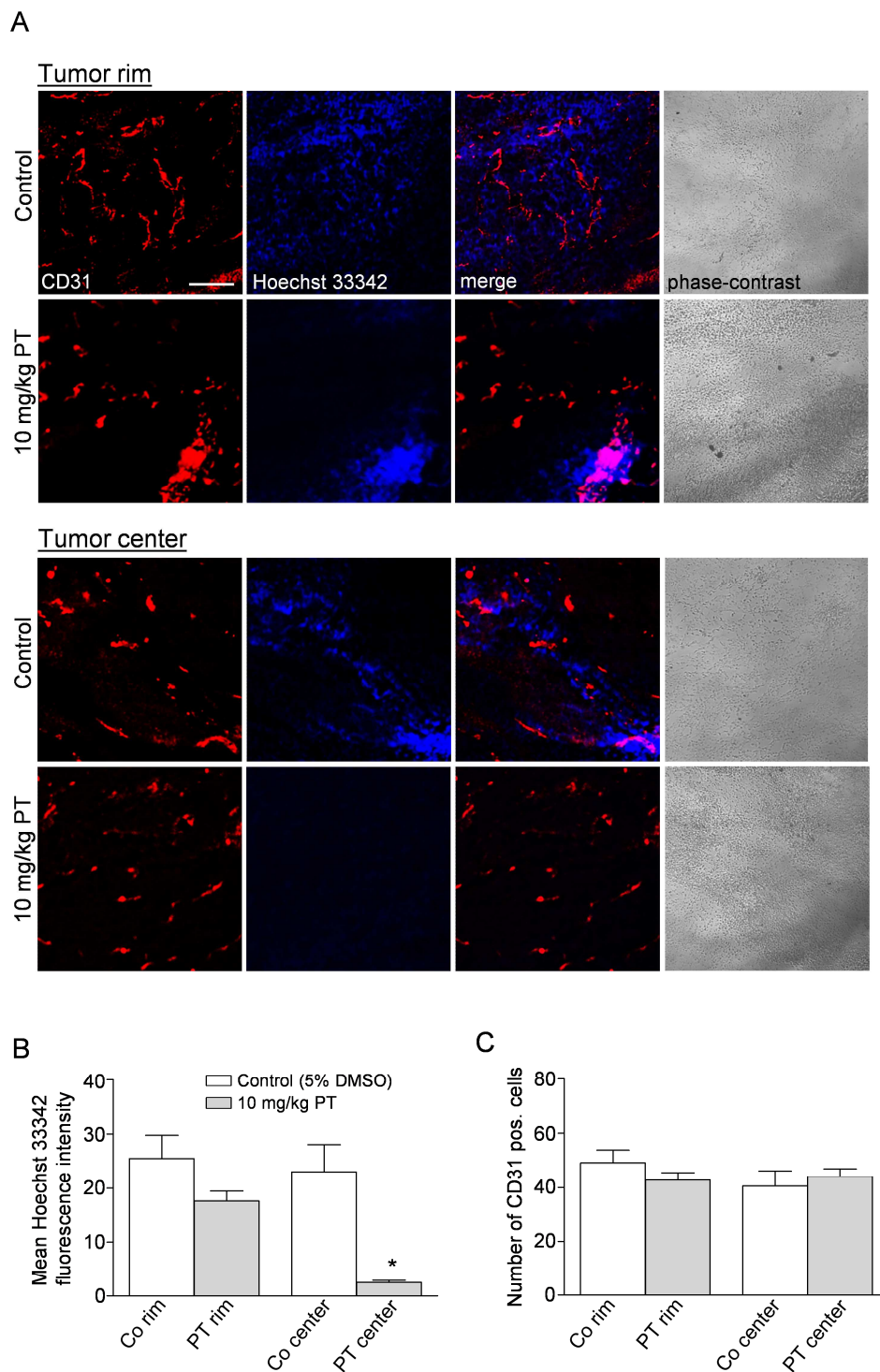
Figure 38   Single dose of PT significantly reduces Hoechst 33342 perfusion in B16-F1 tumor centers, whereby vessel density was not affected. A: B16-F1 mouse melanoma cells were subcutaneously injected into the left hind limb of female C57BL/6 mice. If tumors reached a size of approx. 650 mm³, either DMSO control (5%, 24 h) or PT (10 mg/kg, 24 h) was injected IV. Hoechst 33342 (10 mg/kg) was used as perfusion marker and was injected IV 1 min befor tumor removal. After embedding in frozen tissue medium, cryosections of 10 µm were prepared and stained with an anti-CD31 antibody to visualize endothelial cells. To obtain an overview of the tumor tissue, phase-contrast images were additionally taken. Representative images of control and PT-treated tumor centers and rims are shown. Scale bar represents 200 µm. B, C: For quantification, thirteen pictures of the tumor center and rim of two different sections were taken to analyze the intensity of Hoechst 33342 fluorescence (B) and to count CD31-positive endothelial cells (C). *P, ≤ 0.05 versus control (PT n = 8, DMSO n = 6).

3.3.4 PT induces enormous central necrosis in B16-F1 mouse melanoma tumors

Haematoxylin and eosin staining (H&E) of the same tumors as described above (3.3.3) revealed that single dose treatment with PT resulted in enormous central necrosis (Figure 39 A), which spanned almost 30% of the whole tumor area (Figure 39 B). Control tumors showed central necrosis as well, but only 5% of the whole tumor area were affected and could be ascribed to the big tumor size.
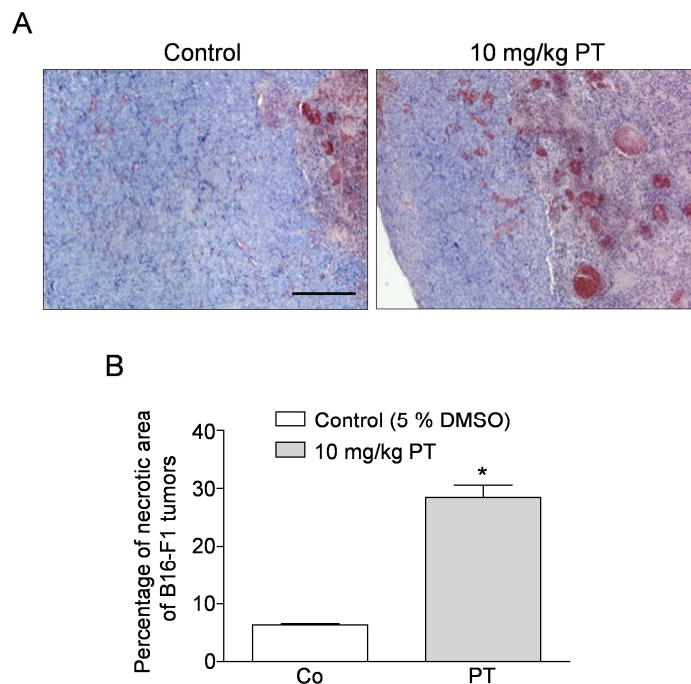
Figure 39   Single dose of PT induces necrosis in B16-F1 tumor centers. A: B16-F1 mouse melanoma cells were subcutaneously injected into the left hind limb of female C57BL/6 mice. If tumors reached a size of approx. 650 mm^3, either DMSO control (5%, 24 h) or PT (10 mg/kg, 24 h) was injected IV. After tumor resection, formalin-fixation and paraffin embedding sections of 5 µm were prepared and stained with H&E. Scale Bar: 400 µm. **B:** Two sections per tumor were photographed using 4x magnification as described in the materials and methods section (2.10.3.2). Quantification of necrotic tumor areas was performed using ImageJ software. *P, ≤ 0.05 versus control (PT n = 9, DMSO n = 6).

Taken together, we clearly could show in two different tumor models that single dose treatment with PT induces a rapid and selective shut-down of tumor blood flow and reduces Hoechst 33342 perfusion *in vivo*, whereas the overall vessel density was not affected. As a result, massive tumor cell necrosis in tumor centers occurred.

3.4 Multiple dose treatment of PT decelerates tumor growth *in vivo*

To evaluate the therapeutical efficiency of PT, we used the same tumor model as described above (3.3.3), but PT treatment started as soon as tumors reached a size of about 90 mm^3. 10 mg/kg PT was applied IV into the tail vein on day 0, 3 and 6, and we determined the overall capacity of PT to affect tumor growth and its tolerability. We observed that the increase in tumor growth was strongly diminished by PT compared to control tumors (Figure 40 A) and that the repeated application of PT was well tolerated since no significant change of mouse weight was measurable (Figure 40 B).
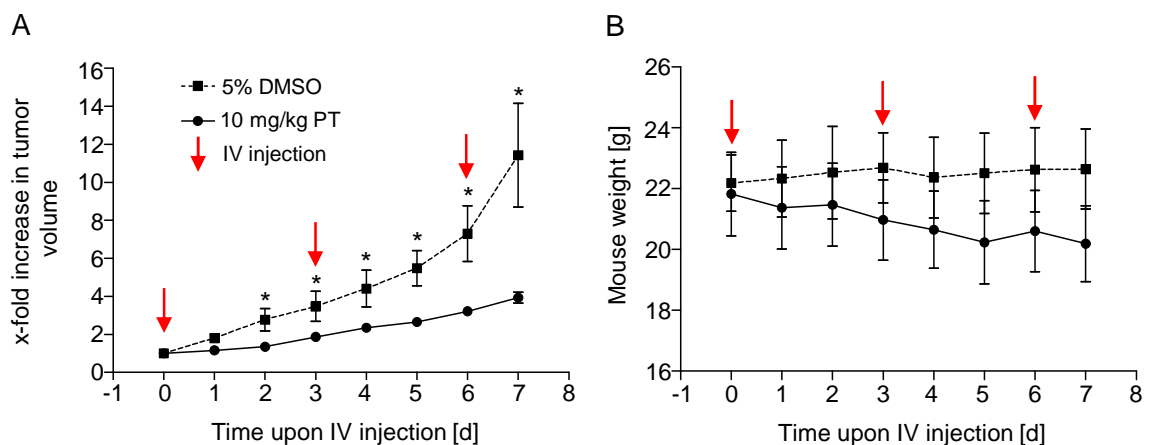
Figure 40   Multiple dose treatment with PT decelerates tumor growth. A: B16-F1 mouse melanoma cells were subcutaneously injected into the left hind limb of female C57BL/6 mice. When tumors reached a size of approx. 90 mm^3, either DMSO control (5%) or PT (10 mg/kg) was injected IV on day 0, 3 and 6 (indicated by red arrows). Increased tumor size was assessed as described in the Materials and Methods section (2.10.4) and is displayed as x-fold increase in tumor volume compared to the starting point (0 d). *P, ≤ 0.05 versus control (PT n = 6, DMSO n = 5). **B:** Mouse weight was measured every day to monitor tolerability of PT.

This result demonstrates that multiple dose treatment with PT was well tolerated and led to a significant impairment of tumor growth *in vivo*. Although we assume that the observed effect was not exclusively mediated through the vascular disrupting potential of PT (also anti-angiogenesis and tumor growth-inhibiting effects are involved), we suggest that the potential of PT as a VDA may play an important part in this context.

In summary, we clearly demonstrated by using *in vitro, ex vivo* and *in vivo* experiments that PT exhibits strong vascular disrupting actions.

4 DISCUSSION

Vascular disrupting agents (VDAs) have gained importance in clinical trials since they represent an effective and additional way to conventional chemotherapy. However, the fact that only a few VDAs have overcome the pre-clinical status and have been introduced into clinical trials, indicate that there are many difficulties that need to be solved. Indeed, VDAs are effective below their maximum tolerated dose (MTD) and complement the anti-vascular effects of angiogenesis inhibitors (AI), but they also show some disadvantages in terms of resistance, scheduling and side-effects. Therefore, it is pivotal for the development of the next generation VDAs to address these issues and to improve their potential benefits. In this regard, natural compounds with their huge variety of new structures offer a considerable source of potential new agents.

In the present study we introduce pretubulysin (PT), a new synthetic accessible natural compound of myxobacterial origin that shows typical VDA hallmarks in endothelial cells *in vitro* as well as in different tumor models *in vivo*. Furthermore, it was well tolerated thus, representing a serious new candidate for further clinical evaluation.

4.1 PT treatment elicits typical hallmarks of vascular disruption in ECs *in vitro*

4.1.1 The impact of PT on microtubules

It is well known that microtubule disassembly induced by VDAs (*e.g.* CA-4-P) or other microtubule destabilizers (*e.g.* nocodazole) leads to various tissue- and cell specific signaling responses. For instance, microtubule depolymerization in fibroblasts attenuates polarity and migration,[118] whereas in neutrophils polarity and migration are induced.[119] In endothelial cells, microtubule disassembly impairs proliferation[16] and time-dependently correlates with RhoA-ROCK-MLC as well as with p38 MAPK activation. Both pathways are known to contribute to actin remodeling, cell contraction and increased vascular permeability. [80, 114, 115, 120] In the present study, we show that the novel tubulin degrading agent PT is able to directly target microtubules and induces concentration-dependent microtubule disassembly in a confluent HUVEC monolayer. This result confirms previous studies of Eirich *et al.*[108] and Rath *et al.*,[16] which demonstrated that PT directly binds to the β-tubulin subunit of microtubules and induces depolymerization in proliferating human microvascular endothelial cells (HMECs). In addition, we observed that PT-mediated microtubule depolymerization time-dependently correlates with an activation of RhoA, phosphorylation of MLC, actin stress fiber formation, junction disruption and with an

increase in permeability. These observed effects are typical for tubulin binding VDAs described in literature, which showed that microtubule depolymerization seems to be the trigger.[80]

4.1.2 The link between PT-mediated microtubule depolymerization and actin stress fiber formation

The exact mechanism how microtubule depolymerization is linked to actin remodeling is not completely investigated so far. However, the fact that PT-mediated microtubule disruption correlates with RhoA activation let us speculate that it could be mediated through guanosine nucleotide exchange factors (GEFs) that are linked to microtubules.[121, 122] GEFs together with GDP-dissociation inhibitors (GDIs) and GTPase-activating proteins (GAPs) regulate the activity-status of small GTPases like Rho, Rac, and Cdc42. Recent studies showed that GEF-H1, a Rho specific GEF, is inactive when it is bound to microtubules, whereas depolymerization results in its release and activation, accompanied by induction of stress fiber formation and MLC phosphorylation.[79] Since these effects are also obvious upon PT treatment, we hypothesize that GEF-H1 might be involved.

Among several RhoA targets it is known from previous work that microtubule targeting agents induce MLC phosphorylation and actin remodeling leading to endothelial hyperpermeability by a RhoA dependent activation of Rho kinase (ROCK).[80, 120, 123] Thereby, the binding of Rho-GTP to ROCK facilitates interactions of ROCK with target proteins (*e.g.* MLC) and regulates the translocation of the protein complex to the target side.[124] By using a specific ATP-competitive ROCK inhibitor (Y27632) we could show that PT-mediated stress fiber formation as well as MLC phosphorylation were reduced. This result indicates an important role of ROCK.

Besides the direct phosphorylation of MLC at Ser19, it is also possible that ROCK indirectly acts on MLC *via* phosphorylation of the regulatory subunit (MYPT-1) of myosin light chain phosphatase (MLCP). In case of phosphorylation, MYPT-1 dissociates from myosin and MLCP activity is inhibited.[123] We used a side-specific antibody to phospho-MYPT-1 (Thr696) and could show that PT-induced ROCK activity does not increase MYPT-1 phosphorylation. This result suggests that PT-mediated activation of MLC only occurs through direct interaction of ROCK.

The counterpart of MLCP, in terms of MLC phosphorylation and activation, is MLCK. Its activity is mainly regulated by the calcium binding protein calmodulin, which binds in the presence of Ca^{2+} to the calmodulin binding domain and release autoinhibition. This in turn

leads to MLC phosphorylation at Ser19 and Thr18, which causes a shift in the tertiary protein structure of MLC and increases actinomyosin contraction. Although the contribution of intracellular Ca^{2+} is controversy discussed and some microtubule binding VDAs and destabilizing MTA act without affecting MLCK,[80, 120, 123] we proved an eventual involvement by using the specific MLCK inhibitor ML-7, and additionally performed intracellular Ca^{2+} measurements. As supposed, PT treatment neither affects MLCK nor alters intracellular Ca^{2+} levels. Thus, strengthens our hypothesis that the observed cellular effects are directly mediated *via* the RhoA-ROCK-MLC pathway.

4.1.3 PT and the microtubule mediated process of membrane blebbing

Besides the RhoA-ROCK-MLC pathway, it is also known that actin remodeling and hyperpermeability, triggered by microtubule disassembly, could be mediated through mitogen-activated protein kinases (MAPKs).[125] Thereby, especially p38 MAPK, a known important regulator of actin remodeling,[126, 127] was reported to be involved in the action of microtubule disrupting compounds[114, 115] and mediates, *via* HSP27, stress fiber formation.[126] In fact, we could show that JNK and particularly p38 MAPK as well as its downstream target HSP27 were strongly phosphorylated by PT. However, treatment with specific inhibitors revealed that activation of p38 MAPK and JNK are not needed to mediate the effects of PT in our system. This observation differs completely from other known microtubules targeting agents, which use the p38 MAPK pathway in addition to the RhoA-ROCK-MLC pathway.[114, 115] We speculate that the PT-induced activation of p38 MAPK might be associated with the process of early membrane blebbing, which was observed at higher concentrations of PT after long-term treatment (data not shown). Early membrane blebbing was intensively described by a study of Kanthou and Tozer[80], in which they could show that membrane blebbing occurred upon the disruption of microtubules. This phenomenon depended on the activation of p38 MAPK, but was independent of MLCK-mediated MLC phosphorylation and, remarkably, of apoptotic blebbing.[80] The underlying mechanisms of how p38 MAPK control membrane blebbing are not clear, but involvement of HSP27, RhoA, and ERK are discussed.[128] Furthermore, membrane blebbing was not observed in either smooth muscle cells or fibroblasts, in which CA-4-P, the lead VDA, induced stress fibers. This selectivity possibly reflects differences in regulation and composition of cytoskeletal systems in ECs.[129]

In addition to the classic p38 MAPK pathways inducing stress fiber formation, hyperpermeability and membrane blebbing, it is conceivable that p38 MAPK directly influences microtubules. For instance, tau, a microtubule associated protein, stabilizes in its unphosphorylated form microtubules and promote their assembly. Due to phosphorylation at multiple Ser/Thr sites by a number of kinases including p38 MAPK, tau-mediated stabilization is diminished, and microtubule depolymerization occurs.[130] It is imaginable that PT-mediated activation of p38 MAPK on the one hand induces membrane blebbing, and on the other hand promotes additional microtubule depolymerization *via* positive feedback mechanisms. However, this assumption needs to be further evaluated.

4.1.4 The influence of PT on endothelial junctions

Besides morphological changes, a further major consequence of VDA treatment involves the maintenance of endothelial barrier integrity. It is known from previous studies, describing VDA action (*e.g.* CA-4-P) that increased paracellular permeability is one of the earliest effects that occur in endothelial cells *in vitro*[80] and in tumor vasculature *in vivo.*[72] This phenomenon was also observed for PT, which concentration-dependently increased permeability within 30 minutes in cultured EC and led to an enormous FITC-dextran extravasation in tumor vessels. Interestingly, *in vitro*, the rise in permeability could partially be inhibited by using the ROCK inhibitor Y27632, suggesting a link between the signal pathways associated with PT action, morphological EC changes and functional properties of the endothelial barrier. The latter is regulated by adherens junctions, especially vascular endothelial (VE) cadherin, and tight junctions consisting of claudin-5, which represent the most important junction proteins to control permeability. In the present study we demonstrated that within 1 h PT treatment, VE-cadherin as well as claudin-5 was disrupted and huge intracellular gaps occurred. At the same time we observed an increase in permeability and cell contraction, indicating a link between junction disruption, hyperpermeability and actinomyosin contraction. In literature, internalization and cleavage of VE-cadherin, as well as tyrosine phosphorylation *via* SRC or Rho-GTPases, are intensively discussed to impair junction integrity, however, the specific consequences regarding vascular permeability are still unknown.[110] Since PT-mediated cellular effects occur within minutes, we suggest that VE-cadherin modifications as described above might be too slow to explain the rapid effect of PT. Therefore, we assume that the observed increase in permeability is mediated by actinomyosin that is coupled to the catenin complex of VE-cadherin. In this case, PT treatment would trigger cell contraction *via* stress fiber formation, which in turn alters VE-cadherin organization and promotes

intracellular gap formation. According to this hypothesis, removal of PT causes reestablishment of a normal EC monolayer with intact junctions and relaxed actin fibers (data not shown), indicating that VE-cadherin reorganization occurs temporarily and seems to be actinomyosin dependent.

In addition, it is known that VE-cadherin regulates by using the phosphatidylinositol-3-OH kinase PI(3)K-AKT-FoxO-pathway the expression of claudin-5 and influences angiogenesis.[131] Thus, it is conceivable that PT-triggered VE-cadherin disruption also affects this pathway. Possibly, VE-cadherin destruction is associated with reduced phosphorylation of the pro-survival signaling of the kinase AKT, which in turn activates members of the FoxO transcription factors. As a result FoxO translocates to the nucleus and inhibits claudin-5 expression. This hypothesis would be in agreement with our results showing that VE-cadherin and claudin-5 junction disruption occurred in a similar way. Furthermore, a previous study by Vincent *et al.*[132] demonstrated that the lead VDA CA-4-P also disrupts VE-cadherin, which was associated with reduced AKT phosphorylation. Actually we have not focused on AKT signaling in this study, hence, this point is still an assumption and requires further investigations.

4.1.5 Cytotoxic profile of PT treatment in confluent ECs

The cytoskeletal rearrangements, which occurred upon PT treatment affected not only the endothelial barrier function but also led to enormous cell shape changes and disruption of established tubes, suggesting that PT might be toxic to HUVECs. Cytotoxicity assays, however, revealed that PT neither considerably reduces metabolic activity nor induces apoptosis or necrosis after 24 h treatment. Furthermore, we could not detect any G2/M arrest, which plays an important role in the onset of apoptotic cell death. Our findings are in contrast to data from previous studies, in which PT as well as the lead VDA CA-4-P was shown to induce G2/M arrest and apoptosis within 24-48 h.[16, 66, 133] The reason for this different result may be due to the fact that we worked with confluent, quiescent HUVECs, whereas the mentioned studies used proliferating ones, which are susceptible to the blockade of the spindle apparatus. This assumption is supported by own experiments showing that proliferating HUVECs pre-treated with PT show a four times higher induction of apoptosis and G2/M arrest than confluent ones (data not shown). Confluent HUVECs treated with CA-4-P also did not undergo metabolic changes, G2/M arrest, apoptosis or necrosis (data not shown). Toxicity studies by Dark *et al.*[70] confirmed our hypothesis, but the reason why proliferating cells are more sensitive to treatment is not fully understood.

Moreover, HUVECs are even able to reassume their normal morphology after withdrawal of PT indicating that treatment is not cytotoxic.

4.2 PT selectively targets tumor vasculature *in vivo*

4.2.1 Mechanisms leading to selective blood flow shutdown

By using different *in vivo* tumor models, we showed that PT treatment induces within 2 h a significant reduction in tumor blood perfusion, whereby perfusion of 'normal' (healthy) tissue seems to be not affected. These events are highly characteristic for tubulin-binding VDAs as previously described for CA-4-P.[73, 134] We can not exclude that 'normal' blood vessels are not at all affected by PT, but we suggest that a mature endothelium covered by pericytes is more stable and, thus, resistant to PT treatment. This hypothesis is also based on previous data, which showed that *in vitro* co-culture of HUVECs with smooth muscle cells are lesser affected than ECs alone.[132] Additionally, differences between tumor and 'normal' vasculature in regard to structure, organization, blood flow, permeability, interstitial fluid pressure, proliferation rate or modifications of tubulin and actin between tumor- and normal vasculature could contribute to the selectivity observed for PT, but are still a matter of debate.[5, 135] Upon PT treatment, tumor vessel perfusion was significantly reduced in tumor centers and was accompanied by necrosis. Interestingly, the distribution of endothelial vessels seems to be not affected and independent of treatment. This suggests that vessels in the tumor center are much lesser perfused, possibly due to constriction or local occlusion by red blood cells, which might occur through endothelial cell shape changes or blebbing.[67] It is also conceivable that the reduced blood velocity caused by PT might contribute to radial movements of erythrocytes far away from the main direction of flow. This enhances collisions and leads to the stacking of red blood cells, thereby evoking an increase in blood viscosity that further facilitates vessel occlusion (Figure 41).[134] An increase in hypoxia, as it is described for CA-4-P, may additionally promote tumor cell death *via* increased production of vasoactive mediators (*e.g.* endothelin), however, this point has not been investigated so far (Figure 41).

4.2.2 Therapeutic potential of PT

Besides the single dose schedule, we also wanted to mimic a more therapeutical setting. We injected PT metronomically (three times, every third day) and measured tumor size as well as mouse weight. Although this model does not allow to discriminate between effects of PT on cancer cells and on the tumor vasculature, the strong tumor growth-decelerating action of PT clearly demonstrates the overall anti-cancer potential of the compound. Importantly, PT seems to be well tolerated since no obvious side effects were detected and the animals did not exhibit significant weight changes. In summary, compared to other xenograft studies,[66, 70] PT shows comparable effects in terms of blood flow shut-down, induction of necrosis and overall anti-tumor activity, although a ten times lower concentration was used. These aspects, plus the good tolerance, let us suggest that PT might be a novel interesting candidate for further preclinical and clinical testing.

4.2.3 Possible adverse effects of PT treatment

Despite the fact that PT, like other VDAs, causes extensive tumor necrosis, it is important to keep in mind that the deficiency in oxygen on the one hand induces tumor cell death, but on the other hand also may stimulate signal pathways that promote angiogenesis.[128] The latter consequence might be the main reason why single treatments with VDAs still fail to prevent tumor regrowth.[81] For instance, hypoxia, which mainly occurs upon vessel occlusion, is a strong inducer of hypoxia-inducible factor (HIF)-1α and related to angiogenic gene expression. In literature, it was shown that CA-4-P induces a strong expression of HIF-1α in cultured ECs, which undoubtably activates angiogenic pathways.[135] Additionally, endothelial progenitor cells, which are mobilized from the bone marrow upon VDA treatment, specifically home into the supplying mother vessels and can also contribute to angiogenic activity.[136] Therefore, CA-4-P treatment is still used in combination with other chemotherapeutic agents or AI that inhibit neovascularization. In this regard, scheduling and the succession of VDA application are very important to obtain tumor control.[83-85] Indeed, we cannot say whether PT treatment induces such signaling cascades leading to angiogenic activity, however, the possibility exists and should be kept in mind when tumors are treated with PT.

The proposed mechanism for the shut-down in tumor blood flow after treatment with PT is shown below (Figure 41).
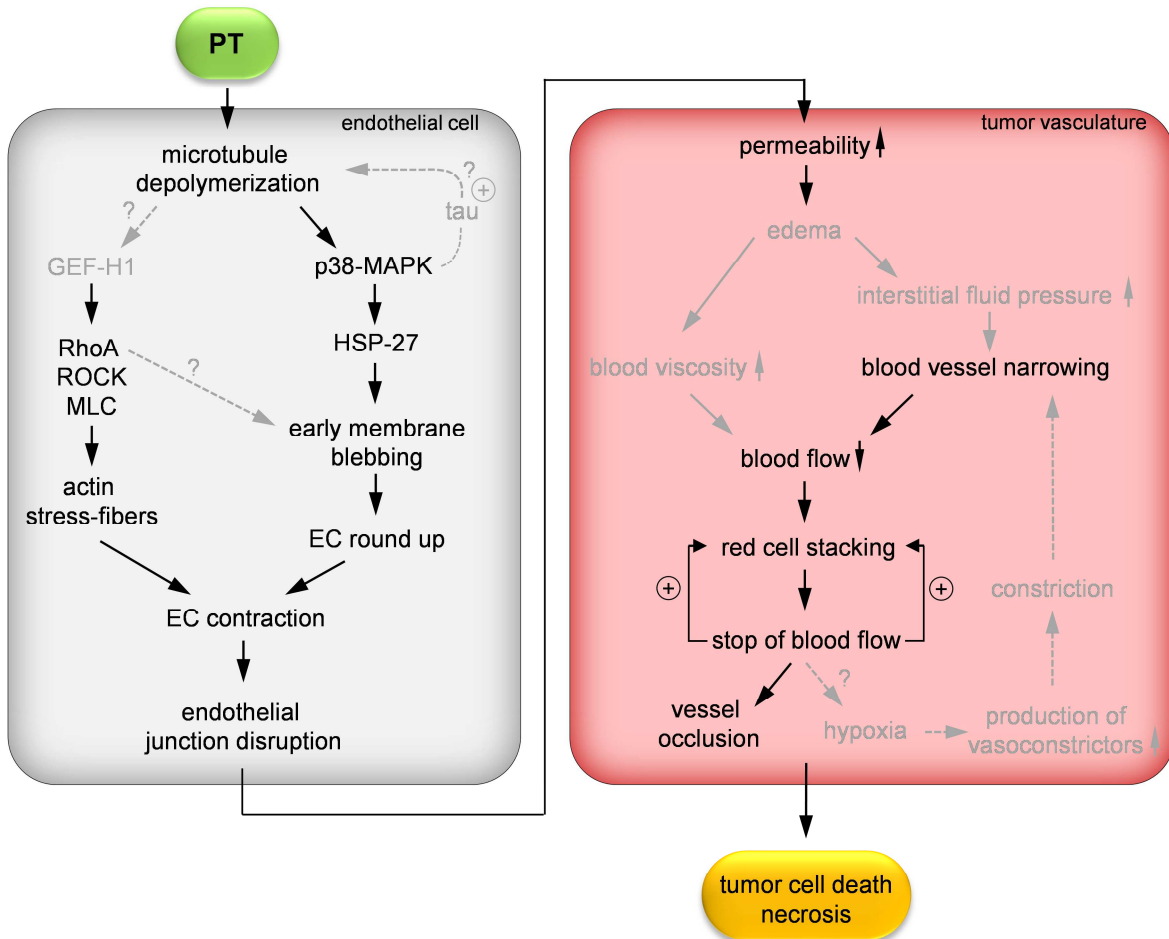

Figure 41   Mode of action of PT on ECs and on tumor vasculature. Microtubule dissasembly activates the RhoA/ROCK/MLC pathway as well as the p38 MAPK pathway. Both evoke actin stress fiber formation and EC contraction. As a result, endothelial junctions are disrupted and permeability increases. At the end, reduced blood flow and tumor cell death induced by necrosis occur. The dashed and grey arrows indicate potential additional pathways activated by PT, however, these were not investigated. EC: endothelial cell.

5 SUMMARY AND CONCLUSION

Vascular disrupting agents (VDAs), in contrast to angiogenesis inhibitors (AI), selectively target the established tumor vasculature of larger solid tumors. They rapidly (within minutes) induce vessel occlusion and blockage of blood flow followed by tumor necrosis. Within the class of VDAs, natural compounds, that induce microtubule depolymerization in ECs are the most successful VDAs tested in clinical trials today. Unfortunately, the number of drug candidates is still limited and some compounds suffer from severe side effects. Thus, there is still a great need to advance this promising field by discovering and characterizing new substances.

In the present study we evaluated pretubulysin (PT), a novel myxobacterial compound, which represents a biosynthetic precursor of the microtubule depolymerizing peptide tubulysin. Structurally, PT is a linear tetrapeptide and synthetically fully accessible. It shows nearly the same tubulin degrading activity than tubulysin and also its anti-angiogenic activity as well as its potential to inhibit tumor cell growth was intensively investigated in previous studies. Since PT showed already profound anti-vascular and microtubule targeting properties in proliferating ECs, we hypothesized that PT also might have vascular disrupting potential in a quiescent endothelium. Therefore, we performed an in-depth characterization of this agent, both *in vitro* and in different *in vivo* tumor models.

Indeed, we could show for the first time that PT elicits typical hallmarks of vascular disruption in ECs. It rapidly (within 30 minutes) induces endothelial hyperpermeability, disrupts endothelial junctions, redistributes focal adhesions and destroys established endothelial tubes. In addition, PT-mediated tubulin depolymerization increases stress fiber formation and EC contraction by activation of the RhoA/ROCK/MLC pathway independent of MLCK, MLCP or calcium. In contrast to the available VDAs, p38 MAPK activation was not found to be involved. Even long-term treatment with PT did not induce biological relevant apoptosis, necrosis or metabolic activity changes, indicating that PT treatment was not cytotoxic. *In vivo*, a single dose of PT (10 mg/kg) significantly and selectively decreased blood flow and vessel diameter in tumors, but not in the neighboring healthy tissue. Additionally, single doses of PT caused enormous tumor cell necrosis within 24 h. Repeated PT doses strongly decelerated tumor growth and were well tolerated.

In conclusion, we demonstrated that PT exerts strong vascular disrupting activities in vitro and selectively impairs tumor blood perfusion in vivo, thereby being efficient at non-toxic doses. Its availability in larges scales provides the opportunity for chemical modification and optimization, which opens up the field for further investigations. Since PT exhibits prominent hallmarks of established VDAs that are tested in clinical trials, we assume that this natural compound represents a novel, promising pharmacological option for anti-vascular tumor treatment.

6 REFERENCES

1.   Schwartz EL. Antivascular actions of microtubule-binding drugs. *Clin Cancer Res*. 2009:15:2594-2601.

2.   Pasquier E, Kavallaris M. Microtubules: A dynamic target in cancer therapy. *IUBMB Life*. 2008:60:165-170.

3.   Jordan MA, Wilson L. Microtubules as a target for anticancer drugs. *Nat Rev Cancer*. 2004:4:253-265.

4.   Furst R, Vollmar AM. A new perspective on old drugs: Non-mitotic actions of tubulin-binding drugs play a major role in cancer treatment. *Pharmazie*. 2013:68:478-483.

5.   Tozer GM, Kanthou C, Baguley BC. Disrupting tumour blood vessels. *Nat Rev Cancer*. 2005:5:423-435.

6.   Pettit GR, Singh SB, Hamel E, Lin CM, Alberts DS, Garcia-Kendall D. Isolation and structure of the strong cell growth and tubulin inhibitor combretastatin a-4. *Experientia*. 1989:45:209-211.

7.   Sosa JA, Elisei R, Jarzab B, et al. A randomized phase ii/iii trial of a tumor vascular disrupting agent fosbretabulin tromethamine (ca4p) with carboplatin (c) and paclitaxel (p) in anaplastic thyroid cancer (atc): Final survival analysis for the fact trial. *J Clin Oncol*. 2011:29:supplement, abstract 5502.

8.   Cooney MM, Radivoyevitch T, Dowlati A, Overmoyer B, Levitan N, Robertson K, Levine SL, DeCaro K, Buchter C, Taylor A, Stambler BS, Remick SC. Cardiovascular safety profile of combretastatin a4 phosphate in a single-dose phase i study in patients with advanced cancer. *Clin Cancer Res*. 2004:10:96-100.

9.   Hollebecque A, Massard C, Soria JC. Vascular disrupting agents: A delicate balance between efficacy and side effects. *Curr Opin Oncol*. 2012:24:305-315.

10.   Ullrich A, Herrmann J, Müller R, Kazmaier U. Synthesis and biological evaluation of pretubulysin and derivatives. *European J Org Chem*. 2009:2009:6367-6378.

11.   Ullrich A, Chai Y, Pistorius D, Elnakady YA, Herrmann JE, Weissman KJ, Kazmaier U, Muller R. Pretubulysin, a potent and chemically accessible tubulysin precursor from angiococcus disciformis. *Angew Chem Int Ed Engl*. 2009:48:4422-4425.

12.   Sandmann A, Sasse F, Muller R. Identification and analysis of the core biosynthetic machinery of tubulysin, a potent cytotoxin with potential anticancer activity. *Chem Biol*. 2004:11:1071-1079.

13.   Kaur G, Hollingshead M, Holbeck S, Schauer-Vukasinovic V, Camalier RF, Domling A, Agarwal S. Biological evaluation of tubulysin a: A potential anticancer and antiangiogenic natural product. *Biochem J*. 2006:396:235-242.

14. Sasse F, Steinmetz H, Heil J, Hofle G, Reichenbach H. Tubulysins, new cytostatic peptides from myxobacteria acting on microtubuli. Production, isolation, physico-chemical and biological properties. *J Antibiot (Tokyo)*. 2000:53:879-885.

15. Herrmann J, Elnakady YA, Wiedmann RM, Ullrich A, Rohde M, Kazmaier U, Vollmar AM, Muller R. Pretubulysin: From hypothetical biosynthetic intermediate to potential lead in tumor therapy. *PLoS One*. 2012:7:e37416.

16. Rath S, Liebl J, Furst R, Ullrich A, Burkhart JL, Kazmaier U, Herrmann J, Muller R, Gunther M, Schreiner L, Wagner E, Vollmar AM, Zahler S. Anti-angiogenic effects of the tubulysin precursor pretubulysin and of simplified pretubulysin derivatives. *Br J Pharmacol*. 2012:167:1048-1061.

17. Newman DJ, Cragg GM. Natural products as sources of new drugs over the 30 years from 1981 to 2010. *J Nat Prod*. 2012:75:311-335.

18. Mishra BB, Tiwari VK. Natural products: An evolving role in future drug discovery. *Eur J Med Chem*. 2011:46:4769-4807.

19. Weissman KJ, Muller R. Myxobacterial secondary metabolites: Bioactivities and modes-of-action. *Nat Prod Rep*. 2010:27:1276-1295.

20. Reichenbach H. Myxobacteria, producers of novel bioactive substances. *J Ind Microbiol Biotechnol*. 2001:27:149-156.

21. Kiskowski MA, Jiang Y, Alber MS. Role of streams in myxobacteria aggregate formation. *Phys Biol*. 2004:1:173-183.

22. Schneiker S, Perlova O, Kaiser O, et al. Complete genome sequence of the myxobacterium sorangium cellulosum. *Nat Biotechnol*. 2007:25:1281-1289.

23. Bode HB, Muller R. The impact of bacterial genomics on natural product research. *Angew Chem Int Ed Engl*. 2005:44:6828-6846.

24. Reichenbach H, Hofle G. Biologically active secondary metabolites from myxobacteria. *Biotechnol Adv*. 1993:11:219-277.

25. Höfle G, Glaser N, Leibold T, Karama U, Sasse F, Steinmetz H. Semisynthesis and degradation of the tubulin inhibitors epothilone and tubulysin. *Pure Appl. Chem. *. 2003:75:167-178.

26. Peltier HM, McMahon JP, Patterson AW, Ellman JA. The total synthesis of tubulysin d. *J Am Chem Soc*. 2006:128:16018-16019.

27. Pando O, Dorner S, Preusentanz R, Denkert A, Porzel A, Richter W, Wessjohann L. First total synthesis of tubulysin b. *Org Lett*. 2009:11:5567-5569.

28. Shibue T, Hirai T, Okamoto I, Morita N, Masu H, Azumaya I, Tamura O. Total syntheses of tubulysins. *Chemistry*. 2010:16:11678-11688.

29.   Erickson HP, O'Brien ET. Microtubule dynamic instability and gtp hydrolysis. *Annu Rev Biophys Biomol Struct*. 1992:21:145-166.

30.   Moritz M, Braunfeld MB, Guenebaut V, Heuser J, Agard DA. Structure of the gamma-tubulin ring complex: A template for microtubule nucleation. *Nat Cell Biol*. 2000:2:365-370.

31.   Stanton RA, Gernert KM, Nettles JH, Aneja R. Drugs that target dynamic microtubules: A new molecular perspective. *Med Res Rev*. 2011:31:443-481.

32.   Desai A, Mitchison TJ. Microtubule polymerization dynamics. *Annu Rev Cell Dev Biol*. 1997:13:83-117.

33.   Mitchison TJ, Kirschner M. Dynamic instability of microtubule growth. *Nature*. 1984:312:237-242.

34.   Margolis RL, Wilson L. Opposite end assembly and disassembly of microtubules at steady state in vitro. *Cell*. 1978:13:1-8.

35.   McIntosh JR, Grishchuk EL, West RR. Chromosome-microtubule interactions during mitosis. *Annu Rev Cell Dev Biol*. 2002:18:193-219.

36.   Wilson L, Panda D, Jordan MA. Modulation of microtubule dynamics by drugs: A paradigm for the actions of cellular regulators. *Cell Struct Funct*. 1999:24:329-335.

37.   Farrell KW, Jordan MA, Miller HP, Wilson L. Phase dynamics at microtubule ends: The coexistence of microtubule length changes and treadmilling. *J Cell Biol*. 1987:104:1035-1046.

38.   Conde C, Caceres A. Microtubule assembly, organization and dynamics in axons and dendrites. *Nat Rev Neurosci*. 2009:10:319-332.

39.   Pasquier E, André N, Braguer D. Targeting microtubules to inhibit angiogenesis and disrupt tumour vasculature: Implications for cancer treatment. *Current Cancer Drug Targets*. 2007:7:566-581.

40.   Safa AR. Identification and characterization of the binding sites of p-glycoprotein for multidrug resistance-related drugs and modulators. *Curr Med Chem Anticancer Agents*. 2004:4:1-17.

41.   Kavallaris M, Burkhart CA, Horwitz SB. Antisense oligonucleotides to class iii beta-tubulin sensitize drug-resistant cells to taxol. *Br J Cancer*. 1999:80:1020-1025.

42.   Martello LA, Verdier-Pinard P, Shen HJ, He L, Torres K, Orr GA, Horwitz SB. Elevated levels of microtubule destabilizing factors in a taxol-resistant/dependent a549 cell line with an alpha-tubulin mutation. *Cancer Res*. 2003:63:1207-1213.

43.   Rouzier R, Rajan R, Wagner P, et al. Microtubule-associated protein tau: A marker of paclitaxel sensitivity in breast cancer. *Proc Natl Acad Sci U S A*. 2005:102:8315-8320.

44. Kavallaris M, Tait AS, Walsh BJ, He L, Horwitz SB, Norris MD, Haber M. Multiple microtubule alterations are associated with vinca alkaloid resistance in human leukemia cells. *Cancer Res*. 2001:61:5803-5809.

45. Verrills NM, Liem NL, Liaw TY, Hood BD, Lock RB, Kavallaris M. Proteomic analysis reveals a novel role for the actin cytoskeleton in vincristine resistant childhood leukemia--an in vivo study. *Proteomics*. 2006:6:1681-1694.

46. Verrills NM, Po'uha ST, Liu ML, Liaw TY, Larsen MR, Ivery MT, Marshall GM, Gunning PW, Kavallaris M. Alterations in gamma-actin and tubulin-targeted drug resistance in childhood leukemia. *J Natl Cancer Inst*. 2006:98:1363-1374.

47. Hanahan D, Folkman J. Patterns and emerging mechanisms of the angiogenic switch during tumorigenesis. *Cell*. 1996:86:353-364.

48. Denekamp J. Endothelial cell proliferation as a novel approach to targeting tumour therapy. *Br J Cancer*. 1982:45:136-139.

49. Chaplin DJ, Hill SA. The development of combretastatin a4 phosphate as a vascular targeting agent. *Int J Radiat Oncol Biol Phys*. 2002:54:1491-1496.

50. Baluk P, Hashizume H, McDonald DM. Cellular abnormalities of blood vessels as targets in cancer. *Curr Opin Genet Dev*. 2005:15:102-111.

51. Naik E, O'Reilly LA, Asselin-Labat ML, Merino D, Lin A, Cook M, Coultas L, Bouillet P, Adams JM, Strasser A. Destruction of tumor vasculature and abated tumor growth upon vegf blockade is driven by proapoptotic protein bim in endothelial cells. *J Exp Med*. 2011:208:1351-1358.

52. Vandenbroucke E, Mehta D, Minshall R, Malik AB. Regulation of endothelial junctional permeability. *Ann N Y Acad Sci*. 2008:1123:134-145.

53. Azzi S, Hebda JK, Gavard J. Vascular permeability and drug delivery in cancers. *Front Oncol*. 2013:3:211.

54. Dejana E. Endothelial cell-cell junctions: Happy together. *Nat Rev Mol Cell Biol*. 2004:5:261-270.

55. Carmeliet P, Jain RK. Angiogenesis in cancer and other diseases. *Nature*. 2000:407:249-257.

56. Tozer GM, Lewis S, Michalowski A, Aber V. The relationship between regional variations in blood flow and histology in a transplanted rat fibrosarcoma. *Br J Cancer*. 1990:61:250-257.

57. Dvorak HF, Nagy JA, Dvorak JT, Dvorak AM. Identification and characterization of the blood vessels of solid tumors that are leaky to circulating macromolecules. *Am J Pathol*. 1988:133:95-109.

58.   Kobayashi H, Tsuruchi N, Sugihara K, Kaku T, Saito T, Kamura T, Tsukamoto N, Nakano H, Taniguchi S. Expression of alpha-smooth muscle actin in benign or malignant ovarian tumors. *Gynecol Oncol.* 1993:48:308-313.

59.   Baluk P, Morikawa S, Haskell A, Mancuso M, McDonald DM. Abnormalities of basement membrane on blood vessels and endothelial sprouts in tumors. *Am J Pathol.* 2003:163:1801-1815.

60.   Hobbs SK, Monsky WL, Yuan F, Roberts WG, Griffith L, Torchilin VP, Jain RK. Regulation of transport pathways in tumor vessels: Role of tumor type and microenvironment. *Proc Natl Acad Sci U S A.* 1998:95:4607-4612.

61.   Hashizume H, Baluk P, Morikawa S, McLean JW, Thurston G, Roberge S, Jain RK, McDonald DM. Openings between defective endothelial cells explain tumor vessel leakiness. *Am J Pathol.* 2000:156:1363-1380.

62.   Boucher Y, Baxter LT, Jain RK. Interstitial pressure gradients in tissue-isolated and subcutaneous tumors: Implications for therapy. *Cancer Res.* 1990:50:4478-4484.

63.   Siemann DW, Bibby MC, Dark GG, Dicker AP, Eskens FA, Horsman MR, Marme D, Lorusso PM. Differentiation and definition of vascular-targeted therapies. *Clin Cancer Res.* 2005:11:416-420.

64.   Landuyt W, Verdoes O, Darius DO, Drijkoningen M, Nuyts S, Theys J, Stockx L, Wynendaele W, Fowler JF, Maleux G, Van den Bogaert W, Anne J, van Oosterom A, Lambin P. Vascular targeting of solid tumours: A major 'inverse' volume-response relationship following combretastatin a-4 phosphate treatment of rat rhabdomyosarcomas. *Eur J Cancer.* 2000:36:1833-1843.

65.   Denekamp J. The tumour microcirculation as a target in cancer therapy: A clearer perspective. *Eur J Clin Invest.* 1999:29:733-736.

66.   Iyer S, Chaplin DJ, Rosenthal DS, Boulares AH, Li LY, Smulson ME. Induction of apoptosis in proliferating human endothelial cells by the tumor-specific antiangiogenesis agent combretastatin a-4. *Cancer Res.* 1998:58:4510-4514.

67.   Tozer GM, Kanthou C, Parkins CS, Hill SA. The biology of the combretastatins as tumour vascular targeting agents. *Int J Exp Pathol.* 2002:83:21-38.

68.   Siemann DW. The unique characteristics of tumor vasculature and preclinical evidence for its selective disruption by tumor-vascular disrupting agents. *Cancer Treat Rev.* 2011:37:63-74.

69.   Chaplin DJ, Pettit GR, Hill SA. Anti-vascular approaches to solid tumour therapy: Evaluation of combretastatin a4 phosphate. *Anticancer Res.* 1999:19:189-195.

70.   Dark GG, Hill SA, Prise VE, Tozer GM, Pettit GR, Chaplin DJ. Combretastatin a-4, an agent that displays potent and selective toxicity toward tumor vasculature. *Cancer Res*. 1997:57:1829-1834.

71.   Davis PD, Dougherty GJ, Blakey DC, Galbraith SM, Tozer GM, Holder AL, Naylor MA, Nolan J, Stratford MR, Chaplin DJ, Hill SA. Zd6126: A novel vascular-targeting agent that causes selective destruction of tumor vasculature. *Cancer Res*. 2002:62:7247-7253.

72.   Tozer GM, Prise VE, Wilson J, Cemazar M, Shan S, Dewhirst MW, Barber PR, Vojnovic B, Chaplin DJ. Mechanisms associated with tumor vascular shut-down induced by combretastatin a-4 phosphate: Intravital microscopy and measurement of vascular permeability. *Cancer Res*. 2001:61:6413-6422.

73.   Thorpe PE. Vascular targeting agents as cancer therapeutics. *Clin Cancer Res*. 2004:10:415-427.

74.   Pilat MJ, Lorusso PM. Vascular disrupting agents. *J Cell Biochem*. 2006:99:1021-1039.

75.   Dumontet C, Jordan MA. Microtubule-binding agents: A dynamic field of cancer therapeutics. *Nat Rev Drug Discov*. 2010:9:790-803.

76.   Ching LM, Zwain S, Baguley BC. Relationship between tumour endothelial cell apoptosis and tumour blood flow shutdown following treatment with the antivascular agent dmxaa in mice. *Br J Cancer*. 2004:90:906-910.

77.   Baguley BC. Antivascular therapy of cancer: Dmxaa. *Lancet Oncol*. 2003:4:141-148.

78.   Ching LM, Cao Z, Kieda C, Zwain S, Jameson MB, Baguley BC. Induction of endothelial cell apoptosis by the antivascular agent 5,6-dimethylxanthenone-4-acetic acid. *Br J Cancer*. 2002:86:1937-1942.

79.   Krendel M, Zenke FT, Bokoch GM. Nucleotide exchange factor gef-h1 mediates cross-talk between microtubules and the actin cytoskeleton. *Nat Cell Biol*. 2002:4:294-301.

80.   Kanthou C, Tozer GM. The tumor vascular targeting agent combretastatin a-4-phosphate induces reorganization of the actin cytoskeleton and early membrane blebbing in human endothelial cells. *Blood*. 2002:99:2060-2069.

81.   Hill SA, Chaplin DJ, Lewis G, Tozer GM. Schedule dependence of combretastatin a4 phosphate in transplanted and spontaneous tumour models. *Int J Cancer*. 2002:102:70-74.

82.   Siim BG, Lee AE, Shalal-Zwain S, Pruijn FB, McKeage MJ, Wilson WR. Marked potentiation of the antitumour activity of chemotherapeutic drugs by the

antivascular agent 5,6-dimethylxanthenone-4-acetic acid (dmxaa). *Cancer Chemother Pharmacol*. 2003:51:43-52.

83. Grosios K, Loadman PM, Swaine DJ, Pettit GR, Bibby MC. Combination chemotherapy with combretastatin a-4 phosphate and 5-fluorouracil in an experimental murine colon adenocarcinoma. *Anticancer Res*. 2000:20:229-233.

84. Siemann DW, Mercer E, Lepler S, Rojiani AM. Vascular targeting agents enhance chemotherapeutic agent activities in solid tumor therapy. *Int J Cancer*. 2002:99:1-6.

85. Murata R, Siemann DW, Overgaard J, Horsman MR. Interaction between combretastatin a-4 disodium phosphate and radiation in murine tumors. *Radiother Oncol*. 2001:60:155-161.

86. Horsman MR, Murata R, Breidahl T, Nielsen FU, Maxwell RJ, Stodkiled-Jorgensen H, Overgaard J. Combretastatins novel vascular targeting drugs for improving anti-cancer therapy. Combretastatins and conventional therapy. *Adv Exp Med Biol*. 2000:476:311-323.

87. Pedley RB, Hill SA, Boxer GM, Flynn AA, Boden R, Watson R, Dearling J, Chaplin DJ, Begent RH. Eradication of colorectal xenografts by combined radioimmunotherapy and combretastatin a-4 3-o-phosphate. *Cancer Res*. 2001:61:4716-4722.

88. Ng QS, Mandeville H, Goh V, Alonzi R, Milner J, Carnell D, Meer K, Padhani AR, Saunders MI, Hoskin PJ. Phase ib trial of radiotherapy in combination with combretastatin-a4-phosphate in patients with non-small-cell lung cancer, prostate adenocarcinoma, and squamous cell carcinoma of the head and neck. *Ann Oncol*. 2012:23:231-237.

89. Siemann DW, Shi W. Efficacy of combined antiangiogenic and vascular disrupting agents in treatment of solid tumors. *Int J Radiat Oncol Biol Phys*. 2004:60:1233-1240.

90. Cooney MM, van Heeckeren W, Bhakta S, Ortiz J, Remick SC. Drug insight: Vascular disrupting agents and angiogenesis--novel approaches for drug delivery. *Nat Clin Pract Oncol*. 2006:3:682-692.

91. Ades EW, Candal FJ, Swerlick RA, George VG, Summers S, Bosse DC, Lawley TJ. Hmec-1: Establishment of an immortalized human microvascular endothelial cell line. *J Invest Dermatol*. 1992:99:683-690.

92. Bouis D, Hospers GA, Meijer C, Molema G, Mulder NH. Endothelium in vitro: A review of human vascular endothelial cell lines for blood vessel-related research. *Angiogenesis*. 2001:4:91-102.

93.   Asaishi K, Endrich B, Gotz A, Messmer K. Quantitative analysis of microvascular structure and function in the amelanotic melanoma a-mel-3. *Cancer Res.* 1981:41:1898-1904.

94.   Endrich B, Asaishi K, Gotz A, Messmer K. Technical report--a new chamber technique for microvascular studies in unanesthetized hamsters. *Res Exp Med (Berl).* 1980:177:125-134.

95.   Wosko TJ, Ferrara DT, Sartori LS. Histological comparison of the b16 melanoma and its f1 variant. *Cancer Lett.* 1984:24:57-63.

96.   Yu J, May L, Milsom C, Anderson GM, Weitz JI, Luyendyk JP, Broze G, Mackman N, Rak J. Contribution of host-derived tissue factor to tumor neovascularization. *Arterioscler Thromb Vasc Biol.* 2008:28:1975-1981.

97.   Zeng H, Qin L, Zhao D, Tan X, Manseau EJ, Van Hoang M, Senger DR, Brown LF, Nagy JA, Dvorak HF. Orphan nuclear receptor tr3/nur77 regulates vegf-a-induced angiogenesis through its transcriptional activity. *J Exp Med.* 2006:203:719-729.

98.   Bradford MM. A rapid and sensitive method for the quantitation of microgram quantities of protein utilizing the principle of protein-dye binding. *Anal Biochem.* 1976:72:248-254.

99.   Smith PK, Krohn RI, Hermanson GT, Mallia AK, Gartner FH, Provenzano MD, Fujimoto EK, Goeke NM, Olson BJ, Klenk DC. Measurement of protein using bicinchoninic acid. *Anal Biochem.* 1985:150:76-85.

100.   Laemmli UK. Cleavage of structural proteins during the assembly of the head of bacteriophage t4. *Nature.* 1970:227:680-685.

101.   Kurien BT, Scofield RH. Protein blotting: A review. *J Immunol Methods.* 2003:274:1-15.

102.   Nicoletti I, Migliorati G, Pagliacci MC, Grignani F, Riccardi C. A rapid and simple method for measuring thymocyte apoptosis by propidium iodide staining and flow cytometry. *J Immunol Methods.* 1991:139:271-279.

103.   Grynkiewicz G, Poenie M, Tsien RY. A new generation of ca2+ indicators with greatly improved fluorescence properties. *J Biol Chem.* 1985:260:3440-3450.

104.   Endrich B, Hammersen F, Gotz A, Messmer K. Microcirculatory blood flow, capillary morphology and local oxygen pressure of the hamster amelanotic melanoma a-mel-3. *J Natl Cancer Inst.* 1982:68:475-485.

105.   Zeintl H, Tompkins W, Messmer K, Intaglietta M. Static and dynamic microcirculatory video image analysis applied to clinical investigations. *Prog Appl Microcirc.* 1986:11:1-10.

106. Klyscz T, Junger M, Jung F, Zeintl H. [cap image--a new kind of computer-assisted video image analysis system for dynamic capillary microscopy]. *Biomed Tech (Berl)*. 1997:42:168-175.

107. Grosios K, Holwell SE, McGown AT, Pettit GR, Bibby MC. In vivo and in vitro evaluation of combretastatin a-4 and its sodium phosphate prodrug. *Br J Cancer*. 1999:81:1318-1327.

108. Eirich J, Burkhart JL, Ullrich A, Rudolf GC, Vollmar A, Zahler S, Kazmaier U, Sieber SA. Pretubulysin derived probes as novel tools for monitoring the microtubule network via activity-based protein profiling and fluorescence microscopy. *Mol Biosyst*. 2012:8:2067-2075.

109. Bogatcheva NV, Verin AD. The role of cytoskeleton in the regulation of vascular endothelial barrier function. *Microvasc Res*. 2008:76:202-207.

110. Dejana E, Orsenigo F, Lampugnani MG. The role of adherens junctions and ve-cadherin in the control of vascular permeability. *J Cell Sci*. 2008:121:2115-2122.

111. Wu Q, Quan H, Xu Y, Li Y, Hu Y, Lou L. P38 mitogen-activated protein kinase is required for the antitumor activity of the vascular disrupting agent 5,6-dimethylxanthenone-4-acetic acid. *J Pharmacol Exp Ther*. 2012:341:709-717.

112. Mehta D, Malik AB. Signaling mechanisms regulating endothelial permeability. *Physiol Rev*. 2006:86:279-367.

113. Yuan SY, Rigor RR. Regulation of endothelial barrier function. *Colloquium Series on Integrated Systems Physiology: From Molecule to Function*. 2011:3:1-146.

114. Birukova AA, Birukov KG, Gorshkov B, Liu F, Garcia JG, Verin AD. Map kinases in lung endothelial permeability induced by microtubule disassembly. *Am J Physiol Lung Cell Mol Physiol*. 2005:289:L75-84.

115. Bogatcheva NV, Adyshev D, Mambetsariev B, Moldobaeva N, Verin AD. Involvement of microtubules, p38, and rho kinases pathway in 2-methoxyestradiol-induced lung vascular barrier dysfunction. *Am J Physiol Lung Cell Mol Physiol*. 2007:292:L487-499.

116. Shtil AA, Mandlekar S, Yu R, Walter RJ, Hagen K, Tan TH, Roninson IB, Kong AN. Differential regulation of mitogen-activated protein kinases by microtubule-binding agents in human breast cancer cells. *Oncogene*. 1999:18:377-384.

117. Wang TH, Wang HS, Ichijo H, Giannakakou P, Foster JS, Fojo T, Wimalasena J. Microtubule-interfering agents activate c-jun n-terminal kinase/stress-activated protein kinase through both ras and apoptosis signal-regulating kinase pathways. *J Biol Chem*. 1998:273:4928-4936.

118. Waterman-Storer CM, Salmon E. Positive feedback interactions between microtubule and actin dynamics during cell motility. *Curr Opin Cell Biol.* 1999:11:61-67.

119. Niggli V. Microtubule-disruption-induced and chemotactic-peptide-induced migration of human neutrophils: Implications for differential sets of signalling pathways. *J Cell Sci.* 2003:116:813-822.

120. Verin AD, Birukova A, Wang P, Liu F, Becker P, Birukov K, Garcia JG. Microtubule disassembly increases endothelial cell barrier dysfunction: Role of mlc phosphorylation. *Am J Physiol Lung Cell Mol Physiol.* 2001:281:L565-574.

121. van Horck FP, Ahmadian MR, Haeusler LC, Moolenaar WH, Kranenburg O. Characterization of p190rhogef, a rhoa-specific guanine nucleotide exchange factor that interacts with microtubules. *J Biol Chem.* 2001:276:4948-4956.

122. Ren Y, Li R, Zheng Y, Busch H. Cloning and characterization of gef-h1, a microtubule-associated guanine nucleotide exchange factor for rac and rho gtpases. *J Biol Chem.* 1998:273:34954-34960.

123. Amano M, Ito M, Kimura K, Fukata Y, Chihara K, Nakano T, Matsuura Y, Kaibuchi K. Phosphorylation and activation of myosin by rho-associated kinase (rho-kinase). *J Biol Chem.* 1996:271:20246-20249.

124. Leung T, Chen XQ, Manser E, Lim L. The p160 rhoa-binding kinase rok alpha is a member of a kinase family and is involved in the reorganization of the cytoskeleton. *Mol Cell Biol.* 1996:16:5313-5327.

125. Stone AA, Chambers TC. Microtubule inhibitors elicit differential effects on map kinase (jnk, erk, and p38) signaling pathways in human kb-3 carcinoma cells. *Exp Cell Res.* 2000:254:110-119.

126. Guay J, Lambert H, Gingras-Breton G, Lavoie JN, Huot J, Landry J. Regulation of actin filament dynamics by p38 map kinase-mediated phosphorylation of heat shock protein 27. *J Cell Sci.* 1997:110 357-368.

127. Huot J, Houle F, Marceau F, Landry J. Oxidative stress-induced actin reorganization mediated by the p38 mitogen-activated protein kinase/heat shock protein 27 pathway in vascular endothelial cells. *Circ Res.* 1997:80:383-392.

128. Kanthou C, Tozer GM. Tumour targeting by microtubule-depolymerizing vascular disrupting agents. *Expert Opin Ther Targets.* 2007:11:1443-1457.

129. van Nieuw Amerongen GP, van Hinsbergh VW. Cytoskeletal effects of rho-like small guanine nucleotide-binding proteins in the vascular system. *Arterioscler Thromb Vasc Biol.* 2001:21:300-311.

130. Reynolds CH, Nebreda AR, Gibb GM, Utton MA, Anderton BH. Reactivating kinase/p38 phosphorylates tau protein in vitro. *J Neurochem*. 1997:69:191-198.

131. Taddei A, Giampietro C, Conti A, Orsenigo F, Breviario F, Pirazzoli V, Potente M, Daly C, Dimmeler S, Dejana E. Endothelial adherens junctions control tight junctions by ve-cadherin-mediated upregulation of claudin-5. *Nat Cell Biol*. 2008:10:923-934.

132. Vincent L, Kermani P, Young LM, Cheng J, Zhang F, Shido K, Lam G, Bompais-Vincent H, Zhu Z, Hicklin DJ, Bohlen P, Chaplin DJ, May C, Rafii S. Combretastatin a4 phosphate induces rapid regression of tumor neovessels and growth through interference with vascular endothelial-cadherin signaling. *J Clin Invest*. 2005:115:2992-3006.

133. Kanthou C, Greco O, Stratford A, Cook I, Knight R, Benzakour O, Tozer G. The tubulin-binding agent combretastatin a-4-phosphate arrests endothelial cells in mitosis and induces mitotic cell death. *Am J Pathol*. 2004:165:1401-1411.

134. Lominadze D, McHedlishvili G. Red blood cell behavior at low flow rate in microvessels. *Microvasc Res*. 1999:58:187-189.

135. Dachs GU, Steele AJ, Coralli C, Kanthou C, Brooks AC, Gunningham SP, Currie MJ, Watson AI, Robinson BA, Tozer GM. Anti-vascular agent combretastatin a-4-p modulates hypoxia inducible factor-1 and gene expression. *BMC Cancer*. 2006:6:280.

136. Shaked Y, Ciarrocchi A, Franco M, Lee CR, Man S, Cheung AM, Hicklin DJ, Chaplin D, Foster FS, Benezra R, Kerbel RS. Therapy-induced acute recruitment of circulating endothelial progenitor cells to tumors. *Science*. 2006:313:1785-1787.

7 APPENDIX

7.1 Publications

7.1.1 Original publications

<u>Kretzschmann VK</u>, Gellrich D, Ullrich A, Zahler S, Vollmar AM, Kazmaier U, Fürst R. The novel tubulin antagonist pretubulysin exhibits profound tumor vessel disrupting properties *in vitro* and *in vivo*.
Submitted

<u>Kretzschmann VK</u> and Fürst R. Plant-derived vascular disrupting agents: Compounds, actions, and clinical trials. Phytochemistry Reviews. 2013:1-16, DOI:10.1007/s11101-013-9304-6

Mamasuew K, Hofmann N, <u>Kretzschmann V</u>, Biel M, Yang RB, Breer H, Fleischer J. Chemo- and thermosensory responsiveness of Grueneberg ganglion neurons relies on cyclic guanosine monophosphate signaling elements. Neurosignals. 2011:19(4):198-209

7.1.2 Oral presentations

<u>Kretzschmann VK</u>, Gellrich D, Ullrich A, Zahler S, Vollmar AM, Kazmaier U, Fürst R. Project 1: Pretubulysin a new microtubule depolymerizing vascular disrupting agent, Project 2: Evaluation of pretubulysin as anti-inflammatory and anti-metastatic agent. 4th FOR 1406 Meeting, July 16-18, 2013, Saarbrücken, Germany

<u>Kretzschmann VK</u>, Gellrich D, Ullrich A, Zahler S, Vollmar AM, Kazmaier U, Fürst R. The novel tubulin antagonist pretubulysin exhibits vascular disrupting properties *in vitro* and *in vivo*. Natural Anticancer Drugs, June 30 – July 4, 2012, Olomouc, Czech Republic

<u>Kretzschmann VK</u>, Gellrich D, Ullrich A, Zahler S, Vollmar AM, Kazmaier U, Fürst R. The novel tubulin antagonist pretubulysin exhibits vascular disrupting properties *in vitro* and *in vivo*. 3rd FOR 1406 Meeting, September 16-18, 2012, Starnberg, Germany

<u>Kretzschmann VK</u>, Ullrich A, Zahler S, Vollmar AM, Kazmaier U, Fürst R. Pretubulysin – a new vascular disrupting agent. 2nd FOR 1406 Meeting, October 26, 2011, Munich, Germany

7.1.3 Poster presentations

Kretzschmann VK, Gellrich D, Ullrich A, Zahler S, Vollmar AM, Kazmaier U, Fürst R. Targeting the tumor vasculature with pretubulysin – a new vascular disrupting agent. 1st European Conference on Natural Products: Research and Applications, September 22-25, 2013, Frankfurt, Germany

Kretzschmann VK, Gellrich D, Ullrich A, Zahler S, Vollmar AM, Kazmaier U, Fürst R. The novel tubulin antagonist pretubulysin disrupts tumor vasculature *in vitro* and *in vivo*. 79th Spring Meeting of the Deutsche Gesellschaft für experimentelle und klinische Pharmakologie und Toxikologie, March 5-7, 2013, Halle/Saale, Germany **Naunyn-Schmiedebergs Archives of Pharmacology. 2013: 386: 1 Suppl: 44-44.**

Kretzschmann VK, Gellrich D, Ullrich A, Zahler S, Vollmar AM, Kazmaier U, Fürst R. The novel microtubule-binding agent pretubulysin shows profound tumor vascular-disrupting properties *in vitro* and *in vivo*. Annual Meeting of the Deutsche Pharmazeutische Gesellschaft e.V. Doktorandentagung, November 14-17, 2012, Weimar, Germany

Kretzschmann VK, Ullrich A, Zahler S, Vollmar AM, Kazmaier U, Fürst R. The tubulin antagonist pretubulysin shows strong vascular-disrupting properties *in vitro*. Interact 2012 PhD symposium, March, 29-30, 2012, Munich, Germany

Kretzschmann VK, Ullrich A, Zahler S, Vollmar AM, Kazmaier U, Fürst R. The tubulin antagonist pretubulysin shows strong vascular-disrupting properties *in vitro*. 78th Spring Meeting of the Deutsche Gesellschaft für experimentelle und klinische Pharmakologie und Toxikologie, March 20-22, 2012, Dresden, Germany **Naunyn-Schmiedebergs Archives of Pharmacology. 2012: 385: 1 Suppl: 49-49.**

Kretzschmann VK, Ullrich A, Zahler S, Vollmar AM, Kazmaier U, Fürst R. The microtubule-binding agent pretubulysin exhibits profound vascular-disrupting properties *in vitro*. Joint Meeting Society of Microcirculation (ESM) and German Society of Microcirculation and Vascular Biology (GfMVB), October 13-16, 2011, Munich, Germany, **Journal of Vascular Research. 2011:48: 1 Suppl: 113-113**

7.2 Curriculum vitae

Personal data

Name	Verena Karoline Kretzschmann
Date of birth	January 8th, 1986
Place of birth	Stuttgart

Academic Education

January 2011-December 2013	PhD thesis at the Department of Pharmacy, Pharmaceutical Biology, LMU Munich, Prof. Dr. A.M. Vollmar and Prof. Dr. R. Fürst
January 2010-October 2010	Diploma thesis at the Institute of Physiology, University of Hohenheim, Prof. Dr. H. Breer and PD Dr. J. Fleischer
October 2005-December 2010	Study of Biology, University of Hohenheim

7.3 Acknowledgements

former group members Bettina and Elisabeth, for their good advices all the time, and for our great but also quite hard running times.

Lena, Tini, Flo, Sandra, Siwei, Simone and Michi, thanks for the wonderful time inside and outside the lab. I really enjoyed our trips within the FOR 1406 group and especially our free-time activities at the roof garden. I am glad to be part of such a great group. Thanks for unforgettable three PhD years and for supporting and motivating me during the last weeks.

I also want to give special thanks to my former lab mate Simone for the great time. You listened and discussed with me science and private life and gave me good advices whenever needed. I wish you all the best for the future and especially for the PhD thesis.

Michi, you are the best lab partner ever, and I really enjoyed our time together. Thanks for your great advices, for listening, for answering all my questions, and for bringing so much fun in the lab. In the last months you became a really good friend and I wish you all the best for your shared future with Anja.

Mille grazie Marco, for being there, whenever I need you. Thanks for your endless encouragement, for your motivation, help and patience during the final run. I am so glad to have you in my life.

Last but not least I want to deeply thank my family for offering me the opportunity to make my way. Thanks, Mum, Dad, Roman and Ruben for your never ending support and belief and for being there whenever needed.